MAGNETIC, SUPERCONDUCTING AND TOPOLOGICAL ORDERS IN IRON-BASED t_{2g} SYSTEM

A Dissertation Presented to

the Faculty of the Department of Physics

University of Houston

In Partial Fulfillment

of the Requirements for the Degree

Doctor of Philosophy

By

Yuan-Yen Tai

May 2014

MAGNETIC, SUPERCONDUCTING AND TOPOLOGICAL ORDERS IN IRON-BASED t_{2g} SYSTEM

Yuan-Yen Tai

APPROVED:

Dr. Chin-Sen Ting , Chairman

Dr. Kevin E. Bassler

Dr. Haibing Peng

Dr. Bernd Lorenz

Dr. Jian-Xin Zhu

Dean, College of Natural Sciences and Mathematics

For my loving parents

Acknowledgements

First of all I would like to thank my supervisor Prof. C. S. Ting for providing me a great opportunity to investigate many challenge and critical problems in theoretical condensed matter physics. His continuous support, constructive suggestions and encouragements greatly helped me to overcome many difficulties.

I'm thankful to all of my graduate committees for their great help and support. I have special thank to Prof. Kevin Bassler, I learned lots of critical thinking and physical concepts in his class. His consistent advice and response to most of my problems made me a better and realistic thinker. I am grateful to Prof. Wu-Pei Su. He is always kind and suggestful to me. On several occasion, he helped and suggested me through my difficulities. I have special thank to Dr. Jian-Xin Zhu and Dr. Matthias J. Graf that they provided me a great chance to have a first hand experience to collaborate in Los Alamos National Labortory where they provided their great help and advices through out my projects.

I have many thanks to Dr. C.-C Joseph Wang, Dr. Tanmoy Das, Dr. Xiaodong Wen, Dr. Yuanyuan Zhao, Dr. Hua Chen and Prof. Lihua Pan. I have great time discuss and collaborate with them in several projects. Throughout these projectes, they provide lots of critical thinkings and helped my project become a better and complete one. I am feeling lucky and grateful to one of my friends Jinnefer Chin-Davis who was always warm hearted and gave me great advice. I am especially grateful to my parents, my sister and many of my friends who care about me and have patience with my Ph.D progress.

MAGNETIC, SUPERCONDUCTING AND TOPOLOGICAL ORDERS IN IRON-BASED t_{2g} SYSTEM

An Abstract of a Dissertation

Presented to

the Faculty of the Department of Physics

University of Houston

In Partial Fulfillment

of the Requirements for the Degree

Doctor of Philosophy

By

Yuan-Yen Tai

May 2014

Abstract

Iron-based superconductors (FeSCs) are a class set of high-temperature superconductor (HTS) based on different crystal structure and pairing symmetry from the Cu-based HTS. The world's physicists, chemists and scientists initiated a substantial research in studying the mechanisms and details of this new class of HTS. The first goal of studying the FeSCs was to hope that more experimental and theoretical explanation to the origin of superconductivity of similar scenario as in Cu-based HTS. Up to recent years, the underlying mechanism for both the magnetism and superconductivity came to reliable models. However, through out my literature studies, there are still debates in several aspects.

I constructed phenomenological model with tight-binding approach for the itinerant picture of electrons, and mean-field self-consistent calculation to study the interacting picture of this model. Point-group-symmetries analysis was also applied to investigate the structure of the model. A proper set of model parameters with correct minimal symmetry analysis well describes the Fermi surface evolution, phase diagram and local density of state (LDOS).

To conclude, from **chapter 2.** to **chapter 5.**, all of my calculated results were nicely compared to experiments and DFT calculations and give deeper understanding to this field. I gave predictions in **chapter 6.** that new topological phases could exist in the tetragonal crystal structure.

Contents

Chapter 1

Introduction

1.1 Experiments and LDA calculations

In 2006 [1], LaOFeAs was the first described iron-pnictide (FeAs) structure that is superconducting, $T_c = 3.5$ K. It was not much attractive until the breakthrough as Kamihara and co-authors reported a hight temperature superconductor (HTS) with $T_c = 26$ K [2] in 2008 and the highest T_c was found to be 55 K in $SmO_{1-x}F_xFeAs$; Table. (D.1) listed these Fe-based HTS compounds with their T_c. Lots of experiments and theoretical research have been initiated since these discoveries.

The iron-based SC (FeSC) is a 2D-layered crystal structure with component of FeX (X=As, Se, P, Te, etc...) structure and other layers with different chemical compounds. It has five different types: (i) 11-FeSe, (ii) 111-LiFeAs, (iii) 122-$SrFe_2As_2$, (iv) 1111-LaFeAsO and (v) 32522-$Sr_3Sc_2O_5Fe_2As_2$ [3], as shown in Fig. 1.1(a). Many Fe-based HTS accompanied with co-linear antiferromagnetic (C-AFM) order as shown in Fig. 1.1(b). The C-AFM is also called spin-density-wave (SDW). All of these five structures share the same layered structure based on a planar layer of iron atoms with anion-atoms (As, Se, P, Te, etc...) tetrahedrally joined, these anion-atoms are above(upper) / below(lower) the Fe plane which is different from the Cu-O based HTS (cuprates) that the Cu-O atoms are in the same plane. Now, we can realize that these upper / lower anion-atoms play important roles that affect the orbital orientation, kinetic energy and pairing symmetries.

TABLE 1.1: Fe-based SCs.

Year	Compound	T_c	Reference
2006	LaOFeAs	3.5 K	[1]
2008	$LaO_{1-x}F_xFeAs$	26 K	[4]
2008	$CeO_{1-x}F_xFeAs$	41 K	[2]
2008	$SmO_{1-x}F_xFeAs$	55 K	[5]
...	...	...	...

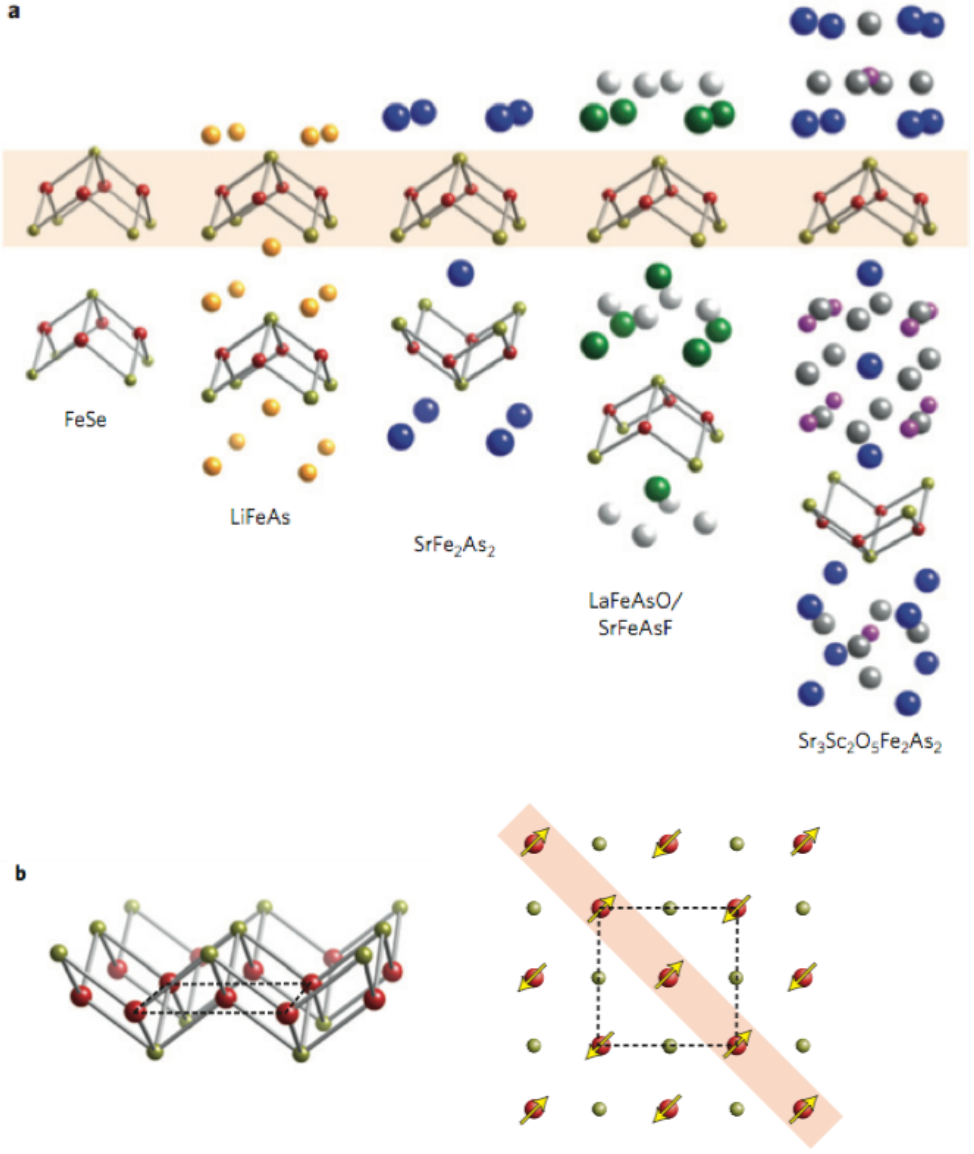

FIGURE 1.1: Crystal and magnetic structure of layered FeSCs, from Ref. [3].

Among these (i-v) structures, doped 122-$BaFe_2As_2$ is one ideal material for both experimental and theoretical studies for the basic understanding of electronic structure, magnetic structure and pairing symmetries. Because it appeared to have almost all of the features of the generic phase diagram: **1**. by electron doping, $BaFe_{2-x}Co_xAs_2$, **2**. by hole doping, $Ba_{1-x}K_xFe_2As_2$, **3**. by iso-valence doping, $BaFe_2As_{2-x}P_x$ and **4**. by applied pressure, as shown in Fig. 1.2. The phase diagram of the FeSCs is very similar to several other unconventional superconductors such as cuprates. Observed from the phase diagram, the undoped (parent) $BaFe_2As_2$ is non-superconducting and having C-AFM under Neel temperature.

Body-centered-tetragonal (BCT) structure with 2-Fe per unit cell each layer is used for describing / coordinating the crystal structure $BaFe_2As_2$ to enclose the above and

below anion atoms. The LDA calculated electronic structure shows cylindrical shaped Fermi-surface around Γ and M points. In which, the Γ point possess hole-pocket and the M point possess electron-pocket [6]. When one considers the SDW magnetic phase, the 2-Fe per unit cell is no longer enough to describe the entire system and one must consider 4-Fe per unit cell with a shrinked Brillouin zone and the Fermi surface of the undoped $BaFe_2As_2$ with SDW order will be folded into tiny pockets for $k_z = 0$ which became a bad metal. If we dive into more physical detail, we learn some orbital physics of the Fe-atom with its five outer shell d-orbitals. The d-orbitals are generally divided into two groups: **1**. $\mathbf{e}_g$ group for $d_{x^2-y^2}$, $d_{z^2-r^2}$ orbitals and **2**. $\mathbf{t}_{2g}$ group for d_{xy}, d_{xz}, d_{yz} orbitals. In particular, the energies of the t_{2g} group are closer to the Fermi-surface and if we extract the partial density of state (PDOS) from Ref. [6] we can learn that t_{2g} orbitals are dominate, most importantly that d_{xz} and d_{yz} orbitals are highly degenerated in energy.

Lee and co-workers published one research article incorporated with orbital order and strong magnetic anisotropy for $CaFe_2As_2$ in LDA calculation [7]. They also concluded that the most important orbitals for FeSCs are d_{xz} and d_{yz} and the SDW order can be generated with Hubbard interaction, U, and Hund's coupling, J_h, terms. More specifically, the Hund's coupling is for describing the inter-orbital and inter-spin interactions between d_{xz} and d_{yz} orbitals. Therefore, this became a simple minimal picture to describe the low energy physics of the emerging SDW magnetism. It was generally known that it is very hard to deal with superconductivity with ab-initio calculations, such as LDA or GGA, due to large matrix of Hamiltonian to be solved with Bogoliubov de Gennes equation and the computer efficiencies go down when the size of the matrix equations goes up. Therefore, there are many issues left to phenomenological model such as SC pairing symmetry, random impurity and magnetic vortices state.

1.2 Microscopic Models

In the literature of past few years, many phenomenological models have been proposed to investigate the band structure, Fermi surface, the SDW order and SC pairing symmetry for FeSCs, ranging from eight orbitals model (five Fe-3d with three As-4p orbitals) [8], five orbitals model (five Fe-3d orbitals) [9], three orbitals model (d_{xy}, d_{xz} and d_{yz}) [10, 11] and down to minimal two orbital model (d_{xz}, d_{yz}) [12–15] or simple two bands model [16–18]. These phenomenological models were invented for different reasons and was used for different calculations. They have several features in common but few of them may have discrepancies. Nevertheless, $S_\pm$ symmetry was generally acknowledged as an essential pairing mechanism among others [18]. We will focus on two-orbital models (with $S_\pm$

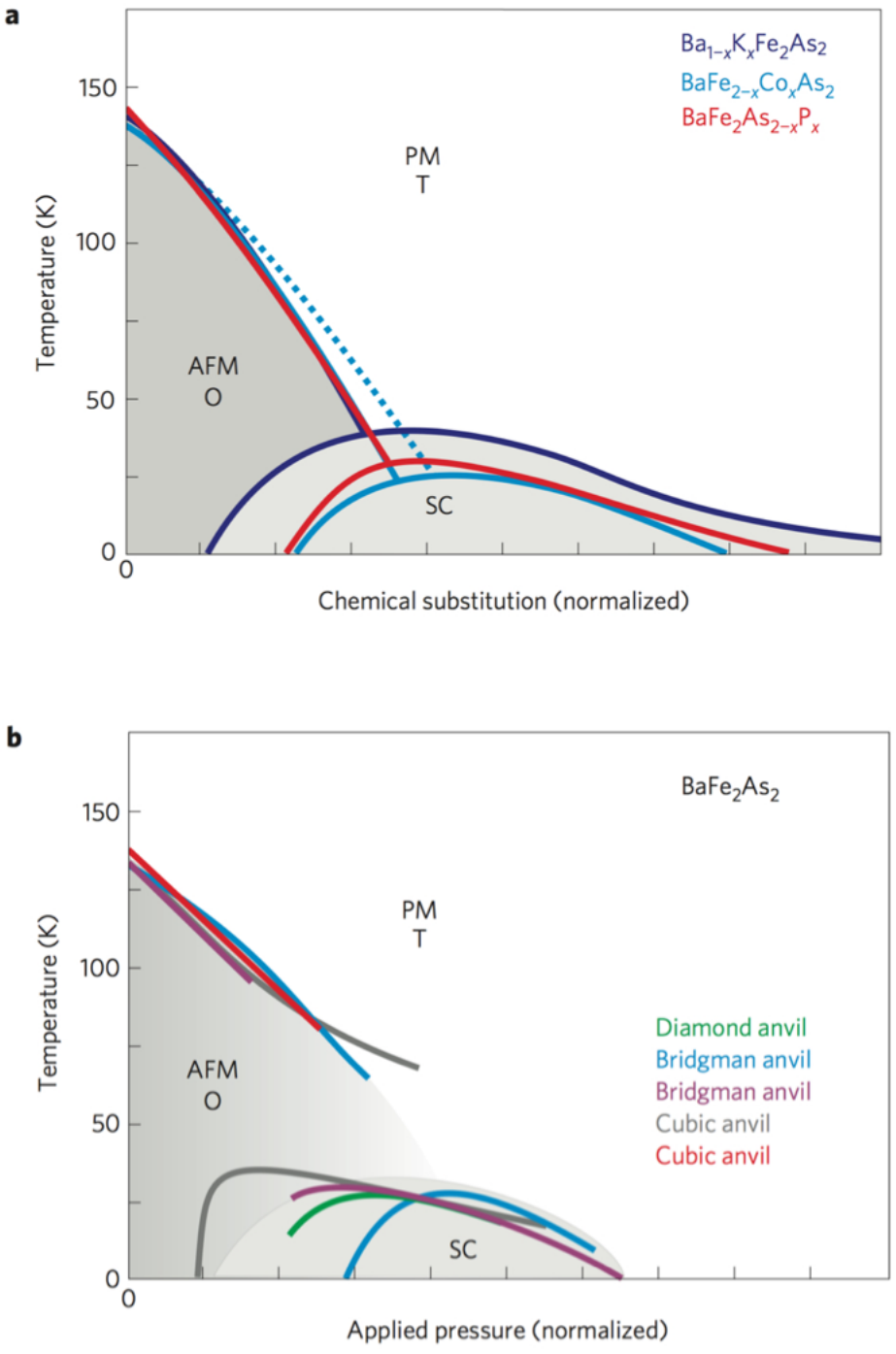

FIGURE 1.2: Doping (a) and pressure (b) dependence of $BaFe_2As_2$, from Ref. [3].

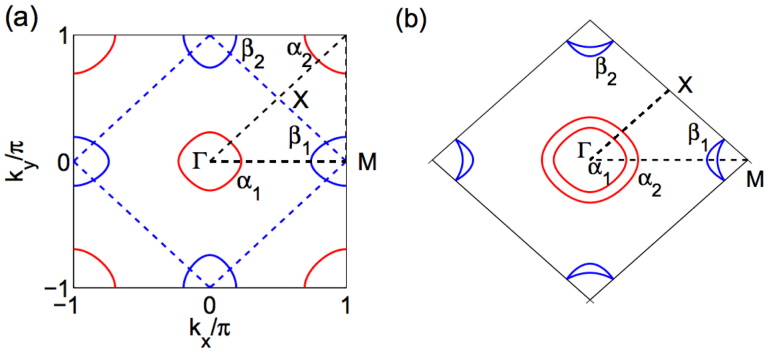

FIGURE 1.3: (a) Fermi surface of 1-Fe unitcell BZ and (b) folded Fermi surface of 2-Fe unitcell BZ given in S. Raghu's model, from Ref. [12].

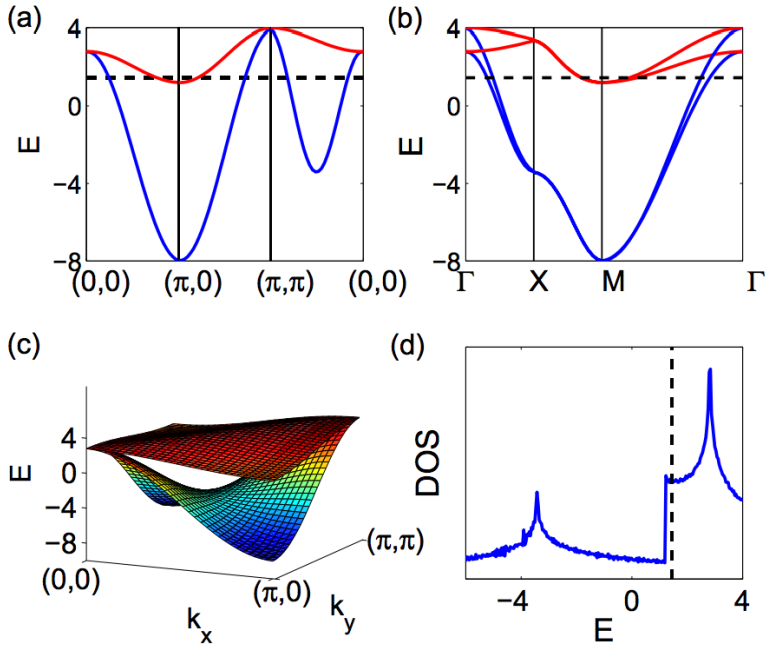

FIGURE 1.4: (a) band structure of 1-Fe unitcell BZ, (b) folded band structure of 2-Fe unitcell BZ, (c) the 3D $E(k)$ plot and (d) DOS calculation of S. Raghu's model, from Ref. [12].

pairing symmetry) for their simplicity and usefulness for phase diagram calculation and large real-space lattice constructions.

The first effective two-orbital model was given by S. Raghu and co-authors [12]. For LDA calculations and experiments, Raghu's model gave nice 2D Fermi surface for half-filling Fermi energy, Fig. 1.3. It can well describe the SDW order and $S_{\pm}$ pairing symmetry with additional interaction terms. However, if one compares the entire band structure and density of state calculation of Raghu's model as shown in Fig. 1.4, one can find that it is different from LDA calculations for d_{xz} and d_{yz} orbitals [3]. One can easily find that the DOS, Fig. 1.4, will immediately encounter with a cliff in lower Fermi level.

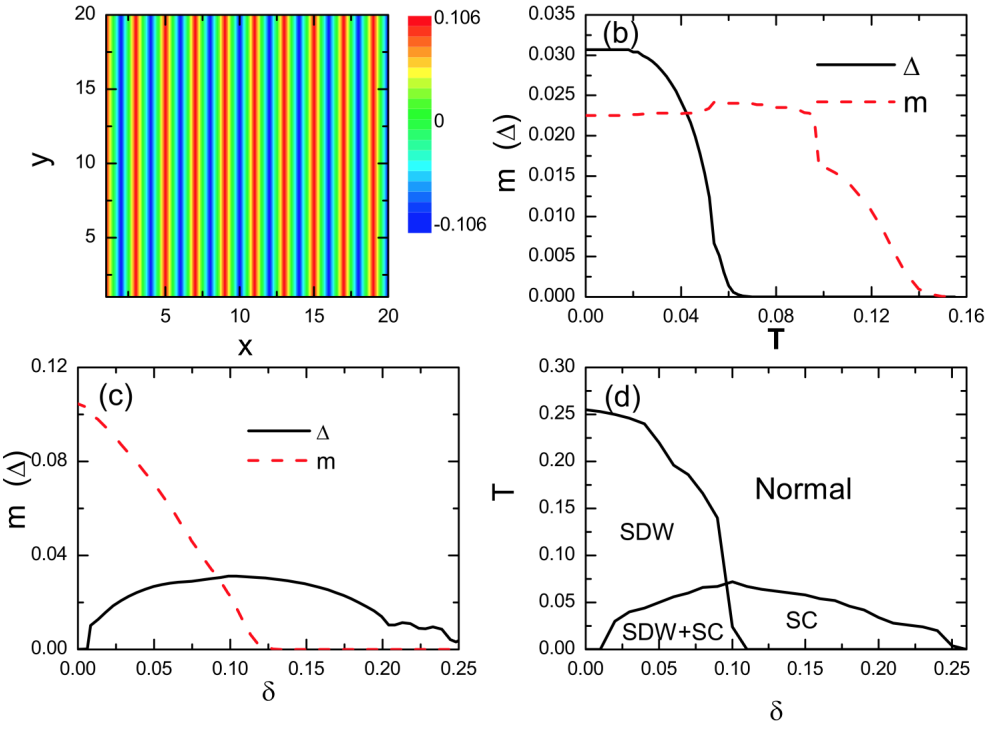

FIGURE 1.5: (a) 2D real space map of SDW order, (b) temperature dependence of SC and SDW order with the doping density $\delta = 0.09$, (c) magnitude of SC and magnetic order as a function of the doping at zero temperature and (d) the calculated phase diagram, from Ref. [19].

Further more, in higher Fermi level the system will go across a Van Hove singularity. These features not seen in LDA calculations and in a physical understanding that the cliff means the hole doped phase diagram of superconductivity should not exist due to insufficient density of state in the hole doped side for effective electron pairing. One important feature was missed in Raghu's model that these upper / lower anion atoms was not taken into consideration which might give a different symmetry in this D_{2d} / C_{4v} crystal structure. More detailed discussions of the D_{2d} / C_{4v} symmetries are placed in the Appendix.

In 2009, D. Zhang provided a new model which considered the effect of upper / lower anion atoms [13]. He considered that the upper / lower anion atoms may mediate different values for the next near neighbor hopping terms. Zhang's model has nice Fermi surface evolution in the electron doped side and it was successfully applied to calculate the electron doped phase diagram in rigid band approximation by Zhou and co-authors [19]. Similar to Lee's LDA calculation [7], T. Zhou applied the on-site Hubbard interaction, U, the Hund's coupling, J_h, and an effective pairing interaction, V, to Zhang's model. The effective Hamiltonian reads,

$$H = H_t + H_{\text{int}} + H_\Delta \tag{1.1}$$

Here H_t is the hopping terms from Zhang's model, H_{int} includes the Hubbard and Hund's interactions and H_Δ is the effective pairing interaction. This effective Hamiltonian can well describe the electron doped phase diagram for $BaFe_2As_2$ as shown in Fig. 1.5. It was a great improvement from Raghu's model, however, the hole-doped part was missing and was not able to be discussed in Zhang's effective two orbital model. In this regard, I will present a new model [15] in chapter 3 to show how we modify and construct a reliable model based on crystal and orbital symmetry. So far, our new model greatly improved the phase diagram calculation and was nicely compared to many experiments and LDA calculations. It was the first microscopic model that achieved so many succesfull calculations among many others.

1.3 Overview of Chapters

Before I close this chapter, let me brifely introduce the following chapters. In **chapter 2.**, I will introduce a generalized calculation method based on Zhang's model [13] to deal with Fermi surface evolutions when disorder effects break translational symmetry [20]. However, Zhang's model [13] used in **chapter 2.** is only applicable to the electron-doped phase diagram of the 122-$BaFe_2As_2$ compounds, the hole-doped part was not able to be applied by Zhang's model. Therefore, in **chapter 3.**, a new model [15] based on symmetry analysis of the FeAs layer was developed. This new model is capable to study the phase diagram of the hole-doped part of $BaFe_2As_2$. In **chapter 4.**, the Fermi surface evolution was investigated of doped $BaFe_2As_2$ when spin-density-wave (SDW) was incorporated. In **chapter 5.**, the new model is extended to investigate the Zn-doping effect of $BaFe_2As_2$. In the last chapter, **chapter 6.**, I extend my study to topological insulators based on the new model [15]. Based on symmetry analysis, we will discuss the possibility of new type of Chern and mirror-Z_2 topological insulator which we predict that the new kind of topological insulator could be realized in some FeSCs or other compounds which has similar crystal structure and orbital order.

Chapter 2

Fermi surface evolution and BAFM in $A_xFe_{2-y}Se_2$

2.1 Introduction

In this chapter, I will investigate a newly found iron-selenide superconductor $A_xFe_{2-y}Se_2$ (A =K, Rb, Cs, Tl, Tl/K, Tl/Rb) [21–24]. This new class of compounds provides a chance to understand the underlying physics when randomness comes to play an important role in condensed matter theory. It has several special features: (i) Superconductivity (for $x \sim 1$ and $y \sim 0.12-0.3$) emerges in proximity to an insulating phase [23, 25] (for $x \sim 0.8$ and $y \geq 0.4$), instead of a poor metal as in other iron-based parent compounds. For the iron deficient compounds with $y \geq 0.4$, there is mounting evidence for the existence of iron vacancy ordered superstructures stabilized with a stripe-like antiferromagetic (AFM) state [26–29]. This raises the interest in the possibility of the insulating phase being driven by the Mott localization [30, 31] due to the reduction in kinetic energy [29] and lack of translational symmetry. More over, the compounds with $x \sim 0.8$ and $y \sim 0.4$ are of special interest for the formation of a peculiar vacancy order (so called $\sqrt{5}\times\sqrt{5}$ superstructure) and it reveals a block-spin antiferromagnetic (BAFM) state [32–35]. (ii) The end member of the series AFe_2Se_2 ($x = 1$ and $y = 0$) is highly electron doped (0.5 electron/Fe) in compare to other Fe-based SCs (such as LaOFeAs, $BaFe_2Se_2$, FeSe etc.). Band structure calculations [36–40] for these end compounds show only electron pockets that are primarily located around the M point of the Brillouin zone (BZ) as defined for a simple tetragonal structure. With the band structure calculations, a series of angle-resolved photoemission spectroscopy (ARPES) experiments has been performed on $A_xFe_{2-y}Se_2$ [41–45]. A common feature is the presence of electron pockets around the M point in the Brillouin zone and a marked absence or near absence of a hole pocket at the Γ point. With regard to electron pockets, the FeSe-122 family is similar to the isostructural FeAs-122 family, while they differ with respect to

the hole pocket, which is considered to be essential for certain interband pairing models of superconductivity.

These unique features raise the hope to gain new insights into the mechanism of iron-based superconductivity by studying the FeSe-122 family. However, special care must be taken in the interpretation of these results due to the complicated real-space structure of highly iron deficient compounds. The real-space structure for different Fe compositions ($0 \leq y \leq 0.4$) is quite intricate and resembles more that of an alloy than of a lightly doped crystal. For example, although both $A\mathrm{Fe}_2\mathrm{Se}_2$ ($y = 0$) and $A_{0.8}\mathrm{Fe}_{1.6}\mathrm{Se}_2$ ($y = 0.4$) compounds have perfect lattice periodicity in the iron layer, the lattice structure for compounds with $0 \leq y \leq 0.4$ can be thought of as a superposition of both lattices, which forms either a random-vacancy lattice or phase-separated lattice with vacancy stripe order. More generally, a serious problem of iron vacancy is introducing random-disorder scattering centers in the iron layer and destroy the translational periodicity, thus rendering the wave vectors of the Bloch wave functions as 'bad' quantum numbers to describe electron motion. Therefore, when interpreting the electronic structure as measured by ARPES, which probes the momentum space, a real-space electronic structure approach must be developed to account for the strong disorder.

In this chapter, we present a systematic study of (i) the evolution of the normal-state electronic structure with random vacancy doping based on a new technique of real-space construction and (ii) the magnetic structure of the FeSe-245 ("$\sqrt{5} \times \sqrt{5}$") structure for fixed hopping term in the t-J model. In (i), the ARPES measurement of the Fermi surface topology was adequately extracted from the spectral function with a tight-binding lattice model with random vacancy order at the Fe sites. We find that the electronic band structure and Fermi surface topology has been dramatically affected by the Fe vacancies which break the lattice periodicity. The evolution in the band dispersion results in a noticeable reconstruction of the Fermi surface (the technical detail is provided in the Appendix A). Therefore, as a consequence, for intermediate iron vacancy concentrations, the realized stable electronic structure is a compromise between the solutions for $y = 0$ (perfect lattice) and $y = 0.4$ (stripe ordered lattice), resulting in a competition between vacancy random disorder and vacancy stripe order. Based on the parameterized hopping model with modified parameters, the constructed mean-field t-J lattice model gives rise to a checker-board block-spin structure for $\mathrm{K}_{0.8}\mathrm{Fe}_{1.6}\mathrm{Se}_2$, which is in good agreement with neutron scattering experiments and *ab-initio* calculations. However, a detailed feature of this calculated magnetism reveals a defeciency in the original Zhang's model [46].

The outline of this chapter is as follows. In Sec. 2.2 we formulate a tight-binding t-J model Hamiltonian and introduce within the mean-field approach the Bogoliubov-de Gennes (BdG) equations. In Sec. 2.3 we discuss the Bloch wave function formulation of multiorbital electron hopping to obtain a single set of model parameters for the

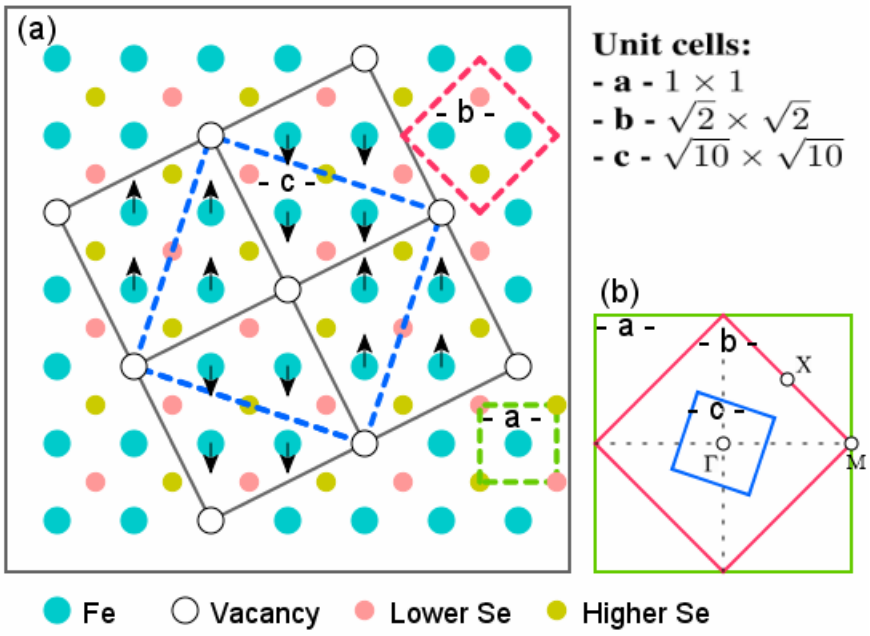

FIGURE 2.1: (Color online) Different cuts (unit cells) of the real-space lattice of FeSe-122 (a) and corresponding unit cells (same color map) in the Brillouin zone (b). The arrows indicate the block-spin AFM structure. For unit cells with cuts "-b-" and "-c-" the Se atoms in the layers above and below are shown. In the vacancy-ordered state ($y = 0.4$) vacancies phase-separate to form stripes.

kinetic energy part of the Hamiltonian by comparing the electronic structure and Fermi surfaces of $K_xFe_2Se_2$ with a perfect lattice structure. In Sec. 2.4 we discuss the electronic structure of a random vacancy lattice by introducing an auxiliary impurity scattering approach in the unitarity limit. In the case of the supercell calculations, the results are in good agreement with the Bloch wave function method. In Sec. 2.5 we present our calculations of the magnetic structure, which agree well with the neutron scattering measurements. The summary is given in Sec. 2.6.

2.2 Model and Formalism

In this chapter, we adopt Zhang's model [46] for the tight-binding Hamiltonian which successfully describes the electronic structure and phase diagram calculations of the FeAs-122 superconductors. Zhang [46] suggested that the upper and lower As atoms mediate different hopping terms between iron atoms in the iron layer. Since this tight-binding model was introduced, several successful studies have been performed [19] to describe ARPES [47, 48], magnetic structures [49, 50], phase diagrams [51], and vortex core and spin susceptibility in RPA calculations [52, 53].

Figure 2.1 shows the schematics of various lattice configurations with real-space unit cells used in this chapter for $A_xFe_{2-y}Se_2$. Recognizing the crystallographic similarities between the isostructural FeSe-122 and FeAs-122 compounds and that the electron

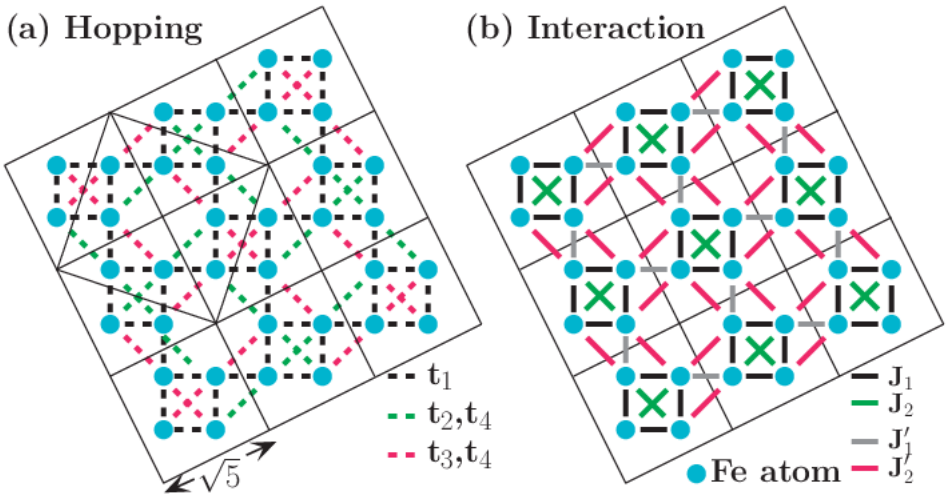

FIGURE 2.2: (Color online) Schematic pictures of the effective t-J Hamiltonian. (a) The effective tight-binding model, where t_1 is the nearest-neighbor (nn) hopping, t_2 (t_3) are the next-nearest-neighbor (nnn) intra-orbital hopping terms due to up (down) Se atoms and t_4 is the nnn interorbital hopping. (b) The effective exchange interactions, where J_1 and J_2 are the nn and nnn interactions inside each block, while J_1' and J_2' are the nn and nnn interactions between blocks.

pocket at the M point is not only a common but also main feature in the heavily electron-doped region, $0 \leq y \leq 0.4$, we use the same tight-binding model for the electron hopping as in Refs. [13, 19]. We account for the reported electronic band structure of the perfect lattice of $K_xFe_2Se_2$,[41] shown in Fig. 2.2(a), by proposing a modified set of hopping parameters $(t_1, t_2, t_3, t_4) = (1, 1, -2, 0.08)$. This modification of parameters is due to lattice distortions caused by vacancies surrounding Fe atoms. In principle, the hopping parameters for the 122 and 245 structure should differ. However, we simplify our approach by keeping the same parameters for all vacancy dopings, because it catches the essential physical picture and describes well the Fermi surface topology of both 122 and 245 structures.

In our approach, we use for simplicity the same hopping parameters for $K_{0.8}Fe_{1.6}Se_2$ as for all other $K_xFe_{2-y}Se_2$ compounds. The unit cell of $K_{0.8}Fe_{1.6}Se_2$ is modified to a $\sqrt{10} \times \sqrt{10}$ area, see Fig. 2.1(a) with cut "-c-" for the unit cell, due to the periodic vacancy order along stripes at the doping concentration $y = 0.4$. In this real-space unit cell there are a total of 10 sites, namely, 8 iron atoms and 2 vacancies. We start with an effective lattice model for $K_{0.8}Fe_{1.6}Se_2$ by including the hopping H^t and exchange interaction H^J terms [54].

$$H = H^t + H^J, \tag{2.1}$$

where

$$H^t = -\sum_{ij\mu\nu\sigma} t_{i\mu j\nu} c^\dagger_{i\mu,\sigma} c_{j\nu,\sigma} - t_0 \sum_{i\mu\sigma} c^\dagger_{i\mu,\sigma} c_{i\mu,\sigma}, \tag{2.2}$$

and

$$H^J = J_1 \sum_{<ij>\mu\nu} \vec{S}_{i\mu} \cdot \vec{S}_{j\nu} + J_2 \sum_{\ll ij \gg \mu\nu} \vec{S}_{i\mu} \cdot \vec{S}_{j\nu} + J_1' \sum_{<ij>'\mu\nu} \vec{S}_{i\mu} \cdot \vec{S}_{j\nu} + J_2' \sum_{\ll ij \gg' \mu\nu} \vec{S}_{i\mu} \cdot \vec{S}_{j\nu}. \tag{2.3}$$

The hopping parameters on the lattice are defined as

$t_{<ij>,\mu=\nu}$	$t^{upper}_{\ll ij \gg,\mu=\nu}$	$t^{lower}_{\ll ij \gg,\mu=\nu}$	$t_{\ll ij \gg,\mu\neq\nu}$
$t_1 = 1$	$t_2 = 1$	$t_3 = -2$	$t_4 = 0.08$

(2.4)

where $i\,(j)$ are site indices, and $\mu\,(\nu)$ are orbital indices corresponding to d_{xz} or d_{yz} wave function orbitals and t_0 is the chemical potential. The expressions $< ij >$ ($\ll ij \gg$) and $< ij >'$ ($\ll ij \gg'$) denote intra- (inter)-block nearest-neighbor (nn) and next-nearest-neighbor (nnn) hopping processes, whereas t^{upper} (t^{lower}) indicates the hopping term crossing over the upper (lower) Se atom as shown in Fig. 2.2(a). In the FeSe-122 compound neutron diffraction studies are consistent with moments pointing along the c axis.[32] Hence, we approximate the Heisenberg interaction to be of the Ising type, where only the S^z component is involved

$$S^z_{i\mu} = \frac{1}{2} \sum_{\alpha\alpha'} c^\dagger_\alpha \sigma^z_{\alpha\alpha'} c_{\alpha'}, \tag{2.5}$$

and the interaction term can be expressed in mean-field approximation by

$$\begin{aligned} S^z_{i\mu} S^z_{j\nu} = & \frac{1}{4}(\langle n_{i\mu\uparrow}\rangle - \langle n_{i\mu\downarrow}\rangle)(n_{j\nu\uparrow} - n_{j\nu\downarrow}) \\ & + \frac{1}{4}(\langle n_{j\nu\uparrow}\rangle - \langle n_{j\nu\downarrow}\rangle)(n_{i\nu\uparrow} - n_{i\nu\downarrow}) \\ & - \frac{1}{4}(\langle n_{i\nu\uparrow}\rangle - \langle n_{i\nu\downarrow}\rangle)(\langle n_{j\nu\uparrow}\rangle - \langle n_{j\nu\downarrow}\rangle). \end{aligned} \tag{2.6}$$

In Fig. 2.2(b) the nn intra- (inter)-block exchange term J_1 (J_1') and nnn intra- (inter)-block exchange term J_2 (J_2') are illustrated. The same type of effective model has also been used to study the electronic properties in other iron-based compounds. [55–59] As mentioned in Ref. [60], the double-occupancy constraint for fermions is implicitly incorporated by the renormalization of the dispersion.

We can now construct the corresponding mean-field Bogoliubov-de Gennes (BdG) matrix equation on a lattice:

$$\sum_{j\nu} \begin{pmatrix} H_{i\mu j\nu\uparrow} & \Delta_{i\mu j\nu} \\ \Delta^*_{i\mu j\nu} & -H_{i\mu j\nu\downarrow} \end{pmatrix} \begin{pmatrix} u^n_{j\nu\uparrow} \\ v^n_{j\nu\downarrow} \end{pmatrix} = E_n \begin{pmatrix} u^n_{i\mu\uparrow} \\ v^n_{i\mu\downarrow} \end{pmatrix}. \tag{2.7}$$

Here the single-particle Hamiltonian $H_{i\mu j\nu,\sigma}$ is expressed by

$$H_{i\mu j\nu\sigma} = -t_{i\mu j\nu} + \frac{\sigma}{4}\sum_{\delta\mu}[(J_\delta + J'_\delta)\langle m_{i+\delta,\mu}\rangle]\delta_{ij}\delta_{\mu\nu} - t_0\delta_{ij}\delta_{\mu\nu}, \tag{2.8}$$

where σ correspond to ± 1 for spin-up(down) index, δ is taken with $\pm\hat{x}$ ($\pm\hat{y}$) and $\pm\hat{x}\pm\hat{y}$, which correspond to the nn and nnn real space shift; J (J') is for the intra (inter) block interaction and the mean-field magnetization per site and per orbital is $\langle m_{i\mu}\rangle = \mu_B(\langle n_{i\mu\uparrow}\rangle - \langle n_{i\mu\downarrow}\rangle)$. The quasiparticle energies E_n are measured with respect to the chemical potential. We note that the single-particle Hamiltonian depends on spin- and orbital-dependent electron density and pairings, which are given by

$$\langle n_{i\mu\uparrow}\rangle = \sum_n |u^n_{i\mu\uparrow}|^2 f(E_n)\ , \tag{2.9}$$

$$\langle n_{i\mu\downarrow}\rangle = \sum_n |v^n_{i\mu\downarrow}|^2 [1 - f(E_n)]\ , \tag{2.10}$$

$$\Delta_{i\mu j\nu} = \frac{V_{i\mu j\nu}}{4}\sum_n (u^n_{i\mu\uparrow} v^{*n}_{j\nu\downarrow} + u^n_{j\nu\uparrow} v^{*n}_{i\mu\downarrow}) \tanh\frac{E_n}{2T}. \tag{2.11}$$

Here we set the Boltzmann constant $k_B = 1$. Finally, the BdG equation (2.7) must be solved self-consistently with Eqns. (2.9)-(2.11). Since we consider only normal-state properties in this chapter, we ignore the superconducting pairing term, $V_{i\mu j\nu} = 0$, in the BdG matrix equation. Note that we study only the hopping term H^t in Secs. III and IV. Whereas in Sec. V we invoke both H^t and H^J terms for the 245 structure.

2.3 Electronic structure in the paramagnetic state

The most common way to construct the electronic band structure of ordered systems is to use the Bloch wave function formulation in the enlarged $\sqrt{10} \times \sqrt{10}$ unit cell with 8 Fe atoms and 2 vacancies, the corresponding **k**-space Hamiltonian is a 16×16 matrix, $H^t_{16\times 16}$, which is straightforward but tedious to derive. Instead, we propose another method based on the impurity problem solution that produces exactly the same results and, moreover, provides physical insight into the breaking of the translational symmetry. In this approach the vacancy is mapped onto an impurity with an adjustable onsite scattering potential V_0 that varies from 0 (no vacancy) to ∞ (strong scattering center). Also the continuous tunability of the impurity potential provides an easy handle on the evolution of the electronic structure with scattering strength. Please refer to the Appendix A for more details on the implementation of the impurity problem calculation employed in this chapter.

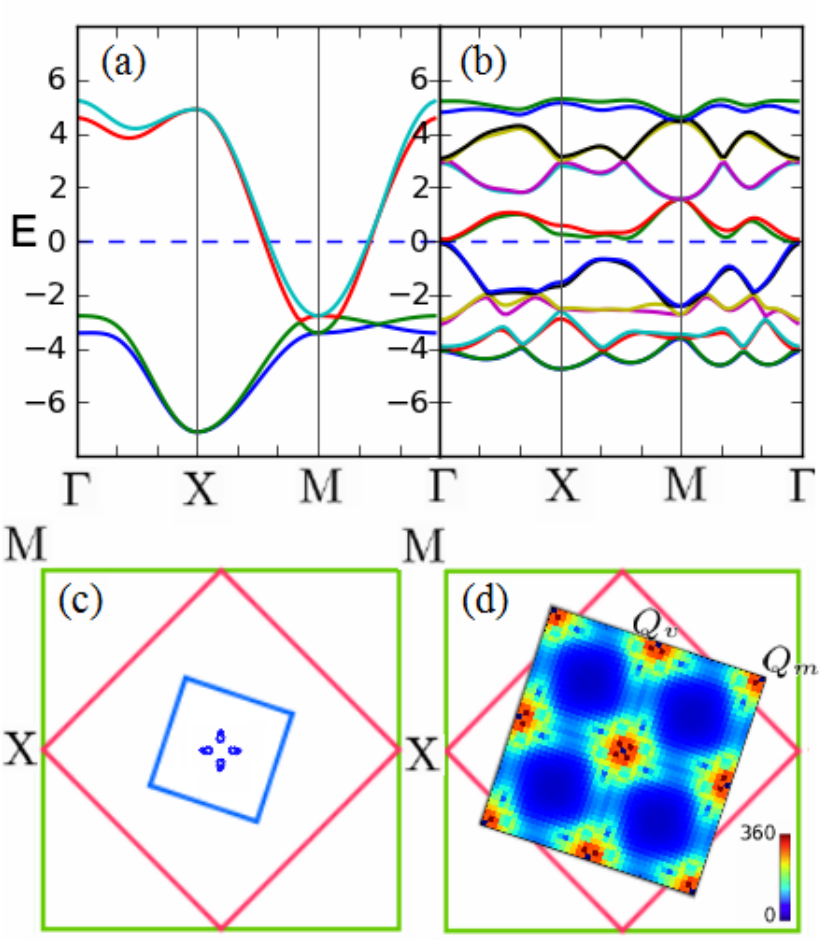

FIGURE 2.3: (Color online) The electronic band structure for compounds (a) $K_{0.8}Fe_2Se_2$ (fill factor $n = 2.4$, $t_0 = 1.09$ for high electron doping) and (b) $K_{0.8}Fe_{1.6}Se_2$ (half-filling $n = 2.0$, $t_0 = 0.005$) with $(t_1, t_2, t_3, t_4) = (1, 1, -2, 0.08)$. The dashed blue line is the location of the chemical potential. (c) Fermi surface of electron pockets of $K_{0.8}Fe_{1.6}Se_2$ located near the Γ point in k-space corresponding to the $\sqrt{10} \times \sqrt{10}$ unit cell (blue square).a (d) Static spin susceptibility for the bare band structure of $K_{0.8}Fe_{1.6}Se_2$. The high intensity spots at scattering wave vectors $Q_v = \pi(\frac{1}{5}, \frac{3}{5})$ and $Q_m = \pi(\frac{4}{5}, \frac{2}{5})$ are in agreement with neutron scattering experiments.

In Fig. 2.3(a) we show the electronic band structure of $K_{0.8}Fe_2Se_2$ for our tight-binding model parameterization using the $\sqrt{2} \times \sqrt{2}$ unit cell (cut "-b-" in Fig. 2.1(a)). The corresponding band structure of the vacancy ordered compound $K_{0.8}Fe_{1.6}Se_2$ is shown for comparison in Fig. 2.3(b). The evolution of the dispersion from the $\sqrt{2} \times \sqrt{2}$ unit cell with four bands to the enlarged $\sqrt{10} \times \sqrt{10}$ unit cell with 16 bands is nontrivial and cannot be obtained by a simple rigid-band shift of the chemical potential. Indeed, the Fermi surface topology for $K_{0.8}Fe_{1.6}Se_2$ shows very tiny electron pockets located near the Γ point, see Fig. 2.3(c), in contrast to $K_{0.8}Fe_2Se_2$.

In addition to the electronic dispersion, we calculate the static spin susceptibility $\chi(\mathbf{q})$ for the bare band structure of itinerant electrons,

$$\chi(\mathbf{q}) = \sum_{IJ} \chi_{IJ}(\mathbf{q}, i\Omega_m \to 0) \ , \tag{2.12}$$

$$\chi_{IJ} = \frac{1}{N}\langle T_\tau[S_I^z(\mathbf{q},\tau)S_J^z(-\mathbf{q},0)]\rangle, \tag{2.13}$$

where N is the total number of unit cells and $S_I^z(\mathbf{q},\tau)$ is the Fourier component corresponding to the site and orbital index I in the unit cell. In this compact notation, the orbital wave functions have the running super-indices $I = (i,\mu)$ and $J = (j,\nu)$. The dynamic susceptibility is given by

$$\begin{aligned}\chi_{IJ}(\mathbf{q}, i\Omega_m) &= -\frac{T}{4N}\sum_{\mathbf{K}\alpha}\sum_{n} G_{J\alpha,I\alpha}(\mathbf{K}, i\omega_n) \\ &\quad \times G_{I\alpha,J\alpha}(\mathbf{K}+\mathbf{q}, i\omega_n + i\Omega_m) \ ,\end{aligned} \tag{2.14}$$

where the wave vector $\mathbf{K}$ is defined in the Brillouin zone corresponding to the $\sqrt{10}\times\sqrt{10}$ unit cell, $\omega_n = (2n+1)\pi T$ and $\Omega_m = 2m\pi T$ are the Matsubara frequencies of the fermions and bosons. In standard notation the multiorbital lattice Green's functions are given by

$$G_{I\uparrow,J\uparrow}(\mathbf{K}, i\omega_n) = \sum_n \frac{u^n_{I\uparrow}(\mathbf{K})\ u^{n*}_{J\uparrow}(\mathbf{K})}{i\omega_n - E_n(\mathbf{K})} \ , \tag{2.15a}$$

$$G_{I\downarrow,J\downarrow}(\mathbf{K}, i\omega_n) = \sum_n \frac{v^{*n}_{I\downarrow}(\mathbf{K})\ v^{n}_{J\downarrow}(\mathbf{K})}{i\omega_n + E_n(\mathbf{K})} \ . \tag{2.15b}$$

In the calculation of the itinerant spin susceptibility the red spots in Fig. 2.3(d) show high intensity around $\mathbf{q} = Q_v$ and Q_m in agreement with neutron scattering experiments.[32] It follows from the Stoner criterion that the observed AFM state is possibly formed from itinerant electrons of the paramagnetic state due to the bare band structure, rather than the exchange interaction of localized spins. Hence, it is natural to expect that close to the magnetic instability a small driving force can break the symmetry of the paramagnetic state and induce the long-range AFM state.

2.4 Electronic structure of random vacancy lattice

The distribution of Fe vacancy in doped FeSe-122 compounds is an open question. Except for the perfect 245-structure, where a Fe-vacancy order can be formed, recent experiments[61–63] indicate that the doped FeSe-122 compounds with Fe chemical concentration deviating from 1.6 or 1.5 are in favor of a nanoscale phase separation. Any of these scenarios suggests that the periodic Bloch wave function formulation is no longer valid for lattices with vacancy disorder in the intermediate doping region $0 < y < 0.4$.

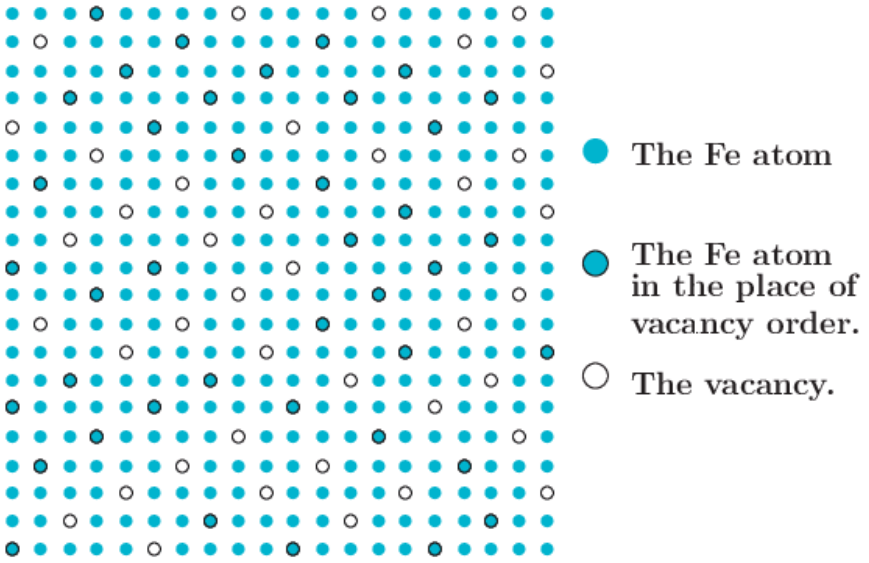

FIGURE 2.4: (Color online) Schematic picture of a 20×20 lattice with random vacancies. For this configuration the minimum size of a supercell is a 10×10 square lattice. This supercell contains the translational symmetries of both the $\sqrt{2} \times \sqrt{2}$ and $\sqrt{5} \times \sqrt{5}$ unit cells. The random lattice is constructed by randomly removing vacancies from the ordered diagonal stripes of phase-separated vacancies. The phase separation pattern along the direction (2,1,0) becomes clearer for larger superlattices.

Here, we describe the construction of a random vacancy lattice calculation (RLC). First, we construct a 40×40 or larger real-space lattice for $A_xFe_2Se_2$ with vacancies phase-separated in stripes along the (2,1,0) direction as shown in Fig. 2.4. Second, we randomly add iron atoms, i.e., remove vacancies, on the vacancy ordered stripes up to the point that we match the vacancy occupation for compounds measured by ARPES. Third, we construct the corresponding real-space Hamiltonian H^t with hopping terms $(t_1, t_2, t_3, t_4) = (1, 1, -2, 0.08)$. Finally, we exactly diagonalize the Hamiltonian and compute its pairs of eigenvalues E_n and eigenvectors $(u^n_{i\mu\uparrow}, v^n_{i\mu\downarrow})$ from which we calculate the lattice Green's functions.

When going beyond the dilute limit of random disorder, as for example in a heavily doped alloy, the randomness of vacancies plays a crucial role for the electronic dispersion, because the rigid-band shift appropriate in the dilute limit breaks down. Hence the conventional approach of periodicity and the calculation of the electronic band structure and Fermi surface fail. In order to solve this complicated problem, we calculate the multiorbital real-space spectral function $A_{IJ}(\omega) = -\frac{1}{\pi}\mathrm{Im}\, G_{IJ}(i\omega_n \rightarrow \omega + i\Gamma)$, which depends on the multiorbital real-space Green's function summed over all bands n,

$$G_{IJ}(i\omega_n) = G_{I\uparrow,J\uparrow}(\mathbf{K} = 0, i\omega_n) + G_{I\downarrow,J\downarrow}(\mathbf{K} = 0, i\omega_n) \; , \tag{2.16}$$

where the general form of the spin-dependent Green's functions on the right-hand side of the above equation has been given in Eq. (2.15). Finally, the Fourier transform of

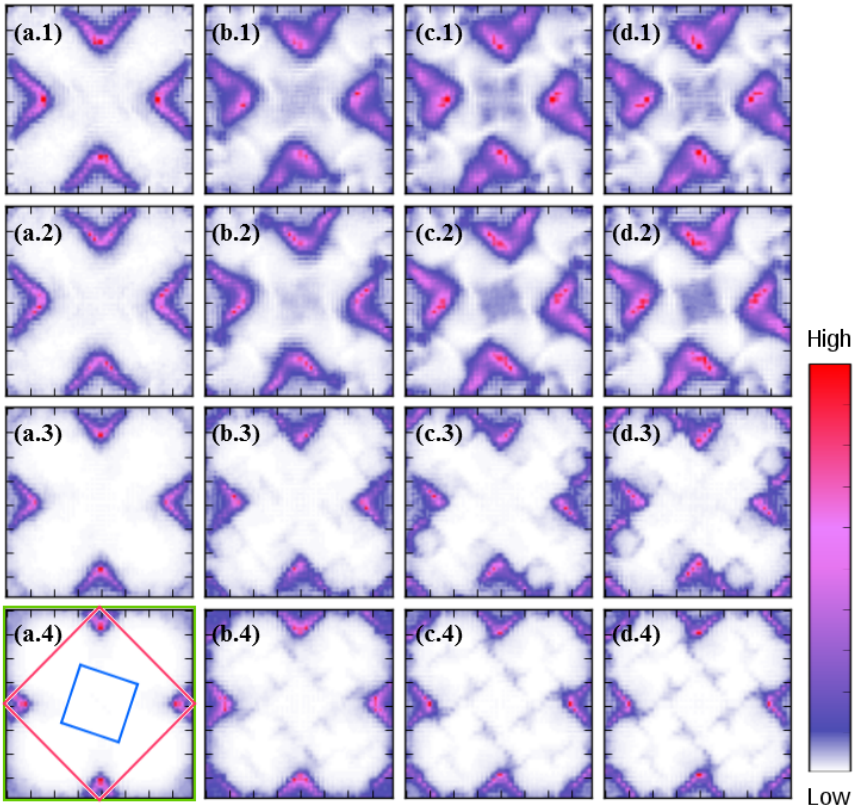

FIGURE 2.5: (Color online) The calculated Fermi surface evolution from the Fourier transformed real-space spectral function in the 1-Fe BZ. The alphabetical order in each picture represents different vacancy concentrations: (a.n) $Fe_{1.9}$, (b.n) $Fe_{1.78}$, (c.n) $Fe_{1.72}$, (d.n) $Fe_{1.7}$, while the numerical index $n = 1 - 4$ represents different values of the chemical potential. The chemical potential varies from high to low as n increases: $(t_0^{(1)}, t_0^{(2)}, t_0^{(3)}, t_0^{(4)}) = (0.5, 0.33, -0.7, -1.5)$. The calculations in panels (b.1), (c.2) and (d.3) correspond to the compounds (Tl,K)$Fe_{1.78}Se_2$, $Tl_{0.58}Rb_{0.42}Fe_{1.72}Se_2$ and $K_{0.8}Fe_{1.7}Se_2$, respectively. In panel (a.4) we redraw the different unit cells of Fig. 2.1(b) with 1×1 (green), $\sqrt{2} \times \sqrt{2}$ (red), and $\sqrt{10} \times \sqrt{10}$ (blue).

$A_{IJ}(\omega)$ to **k**-space for the one-iron per unit cell (1-Fe) gives the desired spectral function, which is the one measured in ARPES experiments,

$$A(\mathbf{k}, \omega) = \sum_{IJ} A_{IJ}(\omega) \exp\{-i\mathbf{k} \cdot (\mathbf{R}_i - \mathbf{R}_j)\}. \tag{2.17}$$

Here, i (j) are lattice indices for the location of each Fe atom in the 40×40 supercell with orbital indices μ (ν) and super-indices $I = (i, \mu)$ and $J = (j, \nu)$. The double-sum is a short-hand notation for $\sum_{IJ} \equiv \sum_{ij} \sum_{\mu\nu} \delta_{\mu\nu}$. Since we considered only the bare band structure, we dropped for convenience the spin indices in this calculation.

Next we apply the RLC method to calculate for both doping variables x and y the evolution of the spectral function and Fermi surface topology for compounds $A_xFe_{2-y}Se_2$. For the hopping term, H^t, the variables x and y can be mapped onto electron filling factor in the two-orbital model: $\langle n \rangle = [x + 8(2 - y) - 4]/[2 - y] - 4$, which is used in turn for

TABLE 2.1: The FeSe-122 compounds for vacancy doping y. The Fermi surface topologies are compared to local density approximation (LDA) calculations[33, 65] or ARPES measurements.[42–44] For the 122 structure (y=0), we focus only on the electron pocket at the M point. For the 245 structure (y=0.4), we focus on the four tiny pockets surrounding the Γ point according to the LDA calculation.

y	compound	referenced	lattice	electron pockets
0.00	$K_{0.8}Fe_2Se_2$	LDA	PLC	M
0.22	$(Tl,K)Fe_{1.78}Se_2$	ARPES	RLC	M
0.28	$Tl_{0.58}Rb_{0.42}Fe_{1.72}Se_2$	ARPES	RLC	M & Γ
0.30	$K_{0.8}Fe_{1.7}Se_2$	ARPES	RLC	M
0.40	$K_{0.8}Fe_{1.6}Se_2$	LDA	PLC	Γ

the determination of the chemical potential, t_0. Figure 2.5 shows the calculated Fermi surface evolution for changing t_0 and y values on random vacancy disorder lattices. The panels 2.5(b.1), 2.5(c.2) and 2.5(d.3) correspond to electron densities reported in experiments.[42–44] The lattices solved were large enough to self-average the vacancy disorder, thus no further ensemble average of different random vacancy configurations was required. The visualization of the evolution of the spectral function helps us to understand when an electron pocket "appears" at the Γ point, namely for $y \geq 0.22$, see panels (b)-(d), as well as when it disappears for shifted chemical potentials $t_0^{(3)} = -0.7$ and $t_0^{(4)} = -1.5$ (rows 3 and 4). Our finding differs from that discussed in Ref. [64], where it was claimed that the electron pocket at the Γ point of the FeSe-122 compound originates from the BAFM structure. However, our results clearly demonstrate the presence of an electron pocket at Γ in the absence of BAFM order and over a large range of vacancy concentrations $0.22 \leq y \leq 0.4$. Indeed Fig. 2.5 shows that the small electron pocket at the Γ point originates from the same regions in the Brillouin zone as for the vacancy stripe-ordered compound with $Fe_{1.6}$ shown in Fig. 2.3. These calculations demonstrate the power of the RLC method, when randomness (doping) strongly affects the Fermi surface. This computational method is adequate to understand the evolution of the electronic structure for intermediate doping levels in the range $0 \leq y \leq 0.4$, where the stable electronic structure is a compromise between the solution for the perfect lattice with $y = 0$ and the stripe-ordered lattice with $y = 0.4$. Alternatively one can obtain these results by diagonalizing large supercells with random lattice Hamiltonians. Of course such a brute force approach is time consuming, especially when many calculations for different random configurations are required as illustrated in the cartoon of Fig. 2.4. We confirmed numerically our results by sampling many random vacancy configurations of large supercells and found that the spectral functions are no different from the RLC method presented here for fixed iron concentrations. In Table 2.1 we list results for both periodic lattice calculations (PLC) and random vacancy lattice calculations (RLC) performed for various vacancy concentrations y.

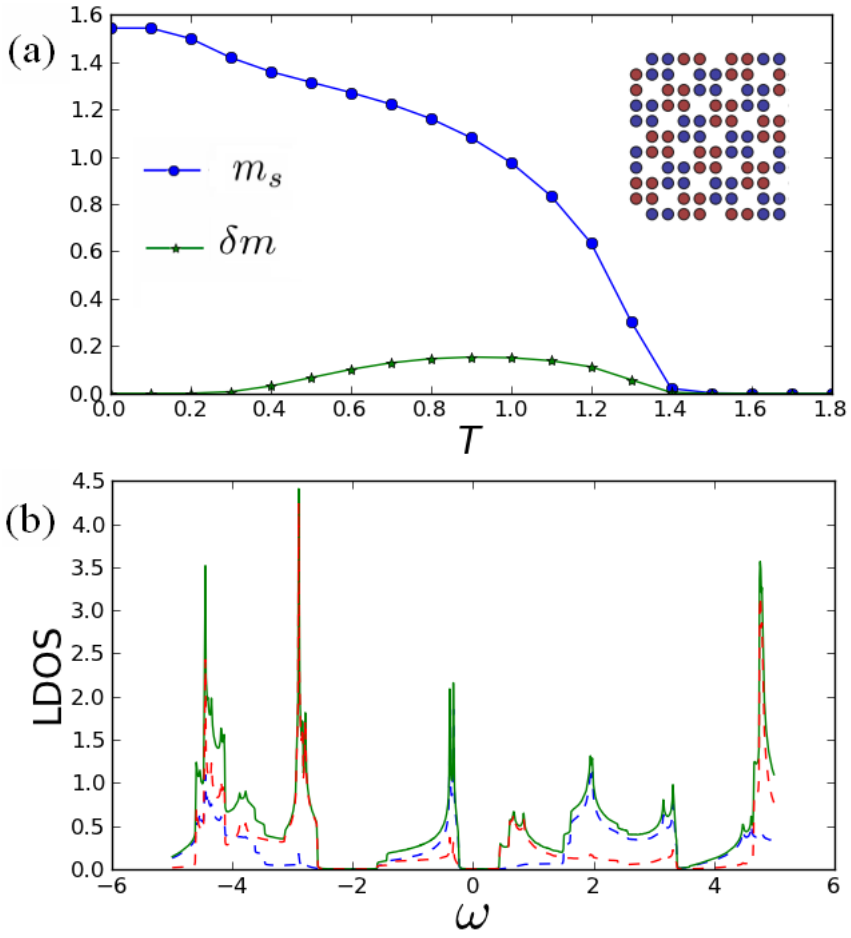

FIGURE 2.6: (Color online) (a) Temperature dependence of the magnetization (as defined in the main text) in the BAFM state. The temperature T is in units of t_1. The inset shows a small part of the lattice used in our mean-field calculation (20×20 sites with 20% vacancies for the stripe-ordered 245 structure of $K_{0.8}Fe_{1.6}Se_2$). (b) The zero-temperature LDOS as a function of energy ω in units of t_1. Shown are the two block sublattices with net spin up (dashed red) and down (dashed blue) lines as well as their sum (solid green). A gap of $\sim 0.4\,t_1$ opens at the Fermi level $\omega = 0$.

Very recently, Berljin *et al.* [66] used the approach of configuration-averaged spectral functions, based on density functional theory calculations to describe the effect of disordered vacancies in $K_{0.8}Fe_{1.6}Se_2$, which is not considered here.

2.5 Magnetic structure in the AFM state

Now that we have fully developed the parameterization for the kinetic part H^t of the t-J lattice model for random vacancy order with a single set of hopping parameters, we can focus on the exchange interaction term H^J. We start with a mean-field calculation for the magnetic state, using a set of rescaled exchange parameters extracted from the band structure calculations. [33] We rescale the *ab-initio* exchange parameters by a global factor to obtain $(J_1, J_2, J_1', J_2') = (-3.44, -0.36, -1.16, 1.52)t_1$, which results in better

agreement of the calculated Néel temperature with experiment. Within our low-energy effective t-J model, this set of exchange parameters leads to a Néel temperature for the block-spin AFM state, $T_N \approx 1.4\, t_1 \approx -0.407\, J_1$, see Fig. 2.6(a). The stability of the BAFM structure is also consistent with a recent study of the J_1-J_2-J_3 Heisenberg model where a stable plaquette order was found.[67] If we assume a hopping integral $t_1 = 35$ meV, we obtain $T_N = 569$ K. Indeed this value is very close to the one observed experimentally ($T_N = 559$ K).[32] We argue that this quantitative result provides further evidence for the dominance of the kinetic term over the exchange term in the t-J Hamiltonian with incipient AFM order due to Fermi surface nesting. Furthermore, we calculate the staggered magnetization as defined by

$$m_s \;=\; \frac{1}{N_L}\sum_i |m_i| \;, \tag{2.18}$$

and its deviation from the standard AFM state may be defined as

$$\delta m \;=\; \frac{2}{N_L}|\sum_i m_i| \;. \tag{2.19}$$

Here N_L is the total number of Fe sites and $m_i = \sum_\mu \langle m_{i\mu}\rangle$ is the spin density on each site i, where the summation index i runs over all lattice sites. In the BAFM state, the system breaks the translational symmetry in the $\sqrt{5}\times\sqrt{5}$ unit cell and gives rise to a larger periodicity with a $\sqrt{10}\times\sqrt{10}$ unit cell. The result for the magnetization as a function of temperature is shown in Fig. 2.6(a), which is in qualitative agreement with the neutron scattering experiments, except for a smaller magnetic moment as observed experimentally per iron site ($3.3\,\mu_B$). [32] The reason for this discrepancy follows from our phenomenological two-orbital model, which has only 2 electrons per Fe site. Therefore, the maximum total moment on each site is $2\mu_B$. Whereas all 5 electrons of the Fe atom seem to participate in the moment formation. Notably our result shows an antiferrimagnetic state at finite temperatures for $T > 0.3t_1$, where $\delta m \neq 0$, that is, the magnetization for the up and down spin blocks are slightly different leading to a net ferri magnetization. This difference is related to the fact that in the present model an asymmetry for the intra-orbital next-nearest-neighbor hopping integrals t_2 vs. t_3 has been introduced due to the selenium atoms below and above the iron layer. We confirmed numerically that for $|t_2| = |t_3|$ a purely antiferromagnetic state exists. It is interesting to note that this type of difference in kinetic hopping terms also manifests itself in the magnetization between the two spin blocks of the bipartite sublattices. The existence of antiferrimagnetism could be identified by weak satellite peaks at the ferromagnetic propagating wave vector $\mathbf{Q} = 0$ in elastic neutron scattering of $K_{0.8}Fe_{1.6}Se_2$ for temperatures $0.3t_1 < T < T_N$. Therefore using the same arguments one should also expect an asymmetry in the AFM split satellite peaks of the nuclear magnetic resonance (NMR)

spectrum. The observation of antiferrimagnetism could serve as an important evidence for different Fe $3d$-electron hopping integrals mediated by Se atoms buckling on both sides of the Fe layer in the bulk system.

Finally, we calculate the local density of states (LDOS) given by

$$\rho_i(\omega) = \sum_{n\mu}[|u^n_{i\mu\uparrow}|^2\delta(E_n - \omega) + |v^n_{i\mu\downarrow}|^2\delta(E_n + \omega)], \tag{2.20}$$

where the delta-function $\delta(x)$ is approximated as $\delta(x) \approx \Gamma/\pi(x^2 + \Gamma^2)$ with the intrinsic quasiparticle broadening parameter Γ. In our calculation, we choose $\Gamma = 0.002$ but note that the result does not change qualitatively for small changes of Γ. For the LDOS calculations we use an 80×80 sites supercell. Figure 2.6(b) shows the zero-temperature LDOS in the BAFM phase on two block sublattices. We note that the LDOS on each site of a chosen block is the same. As a consequence of the exchange interaction a clear gap of size $\sim 0.4t_1$ opens at the Fermi energy $\omega = 0$, which is in qualitative agreement with *ab-initio* band structure calculations for the BAFM state. [33]

2.6 Conclusion

In summary, we systematically addressed within an effective two-orbital model the effects of the iron vacancy on the normal-state electronic structure and magnetic properties in the $A_xFe_{2-y}Se_2$ compounds. We determined a suitable choice of hopping parameters for Fe $3d$-electrons by comparing the Fermi surface topology of ARPES data. From the determined hopping parameters we calculated the evolution of the electronic structure and mapped out the Fermi surface topology for arbitrary Fe vacancy concentration based on a random vacancy disorder model. After the kinetic part of the t-J Hamiltonian was parameterized we focused on the special case of $A_{0.8}Fe_{1.6}Se_2$, where the Fe atoms form the $\sqrt{5} \times \sqrt{5}$ vacancy order. Here we studied the magnetic properties by including the exchange interactions with relative strengths extracted from *ab-initio* calculations. Our mean-field solution of the t-J Hamiltonian reproduced the block-spin antiferromagnetic (BAFM) state, in good agreement with neutron scattering experiments and *ab-initio* calculations. Finally, we found that the magnitude of the magnetization on the two-block bipartite sublattices is at a small variance for temperatures $0.3t_1 < T < T_N$, which made the magnetic structure become more or less an antiferrimagnetic one in finite temperature. This feature is unique to our model with different Se-mediated hopping strengths (below and above the Fe layer) on the two block spin sublattices, which can be tested by future refined neutron scattering and nuclear magnetic resonance experiments in the corresponding temperature range. The signature of the ferrimagnetic can be easily understand by the symmetry analysis under the $\sqrt{5} \times \sqrt{5}$ structure where can easily found that one sub-block contains up-Se atom and the other sub-block contains

down-Se atom. The breaking of up / down Se atom symmetry can easily bring us the understanding of the antiferrimagnetic state. The next chapter will have more complete symmetry and orbital analysis in regard the iron-based SCs for microscopic models.

Chapter 3

Calculated Phase diagram of doped $BaFe_2As_2$ superconductor in a C_4-symmetry breaking model

3.1 Introduction

In **chapter 2.**, I introduced a new method to study the Fermi surface evolution in $A_xFe_{2-y}Se_2$ compound with Zhang's model. Specifically, Zhang's model [13] was the first one which could reproduce the phase diagram of the electron doped $BaFe_2As_2$ among many other microscopic models [9, 14, 19, 64, 65, 68–71]. However, the model failed to give account of the hole-doped (h-doped) part of the phase diagram when doping on the Ba site. A deeper insight could be found in the last part of **chapter 2.** that the calculated antiferrimaghetic order is due to the hopping terms setting in Zhang's model. In this chapter, I aim to gain insights from Zhang's model and construct a new model which could escape these potential issues (missing h-doped part and antiferrimagnetism) from Zhang's model. Very recently, Hu and co-workers [14] proposed a Hamiltonian with S_4 symmetry to clarify the local symmetry breaking of the underlying electronic structure through orbital ordering in the Fe-122 family. Both models by Zhang [13] and Hu [14] share a very important ingredient, that is, the breaking of the C_4 symmetry. So far both models have been applied only to the e-doped region of the phase diagram [19, 70]. Although both models give a qualitative picture of competing order in the system, caution must be taken when the evolution of the low-energy quasiparticle states and Fermi surface topology are considered. These can impose even stricter constraints on a given model: (i) e-doping: The disappearance of the hole pockets at the Γ point of the Brillouin zone (BZ) is the key feature of e-doped compounds $BaFe_{2-x}Co_xAs_2$ [48, 51, 72–74]. (ii) h-doping: The nested large electron pockets around the M point of the BZ evolve into a set of four small clover-like hole pockets for the end member

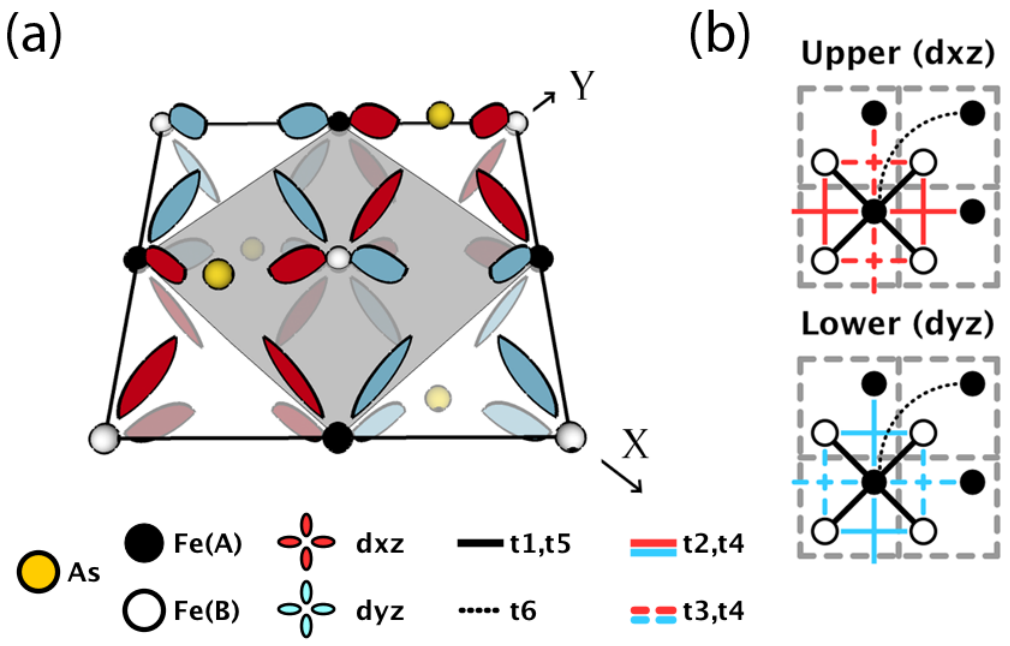

FIGURE 3.1: (color online) (a)3D schematic picture of the Fe d_{xz} and d_{yz} orbital overlap through the As atoms. In panel (a), the red (blue) lobes represent the d_{xz} (d_{yz}) orbitals. The black (white) spheres represent the Fe atoms on the A (B) sublattice and the yellow spheres represent the upper (lower) As atoms located above (below) the Fe plane. This configuration shows a 2×2 (4-Fe) unit cell within the solid thick lines. The shaded region is the 2-Fe unit cell. The 2-Fe unit cell is used in panel (b) to construct the tight-binding model, where the As atoms are not shown. In panel (b), the solid black line stands for nearest-neighbor (1NN) intra- (t_1) and inter-orbital (t_5) hopping. The solid (dashed) red and blue lines stand for second-nearest-neighbor (2NN) intra-orbital hopping t_2 (t_3). The difference between red and blue lines stands for d_{xz} and d_{yz}, while t_4 is isotropic 2NN intra-orbital hopping. The dotted black line stands for the third-nearest-neighbor (3NN) hopping t_6.

KFe_2As_2, which is identified as a Dirac cone [75–77]. A very similar feature is also found in several density functional theory (DFT) calculations [65, 68, 71, 78, 79]. Note that this is an intrinsic feature of the bare band structure and is not related to emergent spin-density wave order [80, 81].

Aided by experiments and DFT calculations, we develop a minimal tight-binding model with improved normal-state band structure parametrization to account for conditions (i) and (ii). The crystal structure of $BaFe_2As_2$ ($ThCr_2Si_2$ type structure) and its electronic structure are now well understood and the relevant orbitals for atomic bonding have been identified [82]. Within a quantum-chemical framework of bonding one realizes that the upper (lower) anion atom mediates the overlap between the Fe $3d_{xz}$ ($3d_{yz}$) orbital with the $4p$ orbitals of the As atom. A schematic picture of the overlap between these orbitals is shown in Fig. 3.1(a). The challenge in the study of superconductivity in the Fe-based 122 family is how to simultaneously satisfy the observations (i) and (ii).

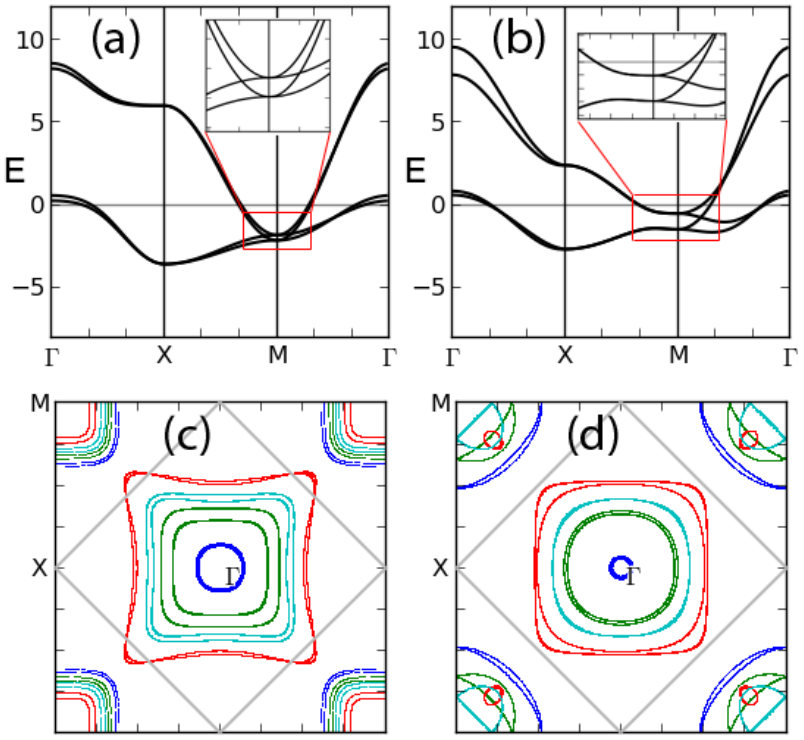

FIGURE 3.2: (color online) The electronic band structure of model Hamiltonians H_1^t (a) and H_2^t (b) along high-symmetry directions in the BZ. The insets show the significant difference between H_1^t and H_2^t near the M point. The horizontal line in (a) and (b) indicates the Fermi level E_f for half filling ($n = 2.0$). Panel (c) shows the Fermi surfaces for model H_1^t for $n = 2.23$ (blue, μ=-0.76), $n = 2.0$ (green, μ=-1.244), $n = 1.8$ (cyan, μ=-1.65), $n = 1.5$ (red, μ=-2.25). Panel (d) shows the FSs of model H_2^t for different doping levels $n = 2.38$ (blue, μ=-0.055), $n = 2.0$ (green, μ=-0.89), $n = 1.8$ (cyan, μ=-1.25), $n = 1.5$ (red, μ=-1.745).

In this chapter, we show that in order to model the low energy bands, we need to consider one more key condition beyond those already proposed by Zhang, which is critical for the second-nearest neighbor (2NN) hopping terms. **I:** A 90° relative orbital rotation is introduced between the A and B sublattices of the Fe atoms ($t_2 \neq t_3$), see Fig. 3.1(b). **II:** On the same sublattice, we propose an additional 90° rotation between the d_{xz} and d_{yz} intra-orbital hopping, which is in agreement with the LDA calculations of Refs. [9, 83]. **III:** An isotropic inter-orbital hopping term t_4 is introduced. The combined effects of conditions **I** and **II** reduce the symmetry to D_{2d}.

3.2 Theory

The original set of four hopping parameters, t_{1-4}, in Zhang's model accounted only for conditions **I** and **III**. In our new model, we include the symmetry condition **II** and thus extend the set to six hopping parameters t_{1-6} [84, 85]. For the calculations we choose the 2-Fe unit cell, as described in Fig. 3.1(a), to construct the basis function $\psi =$

$(c_{A1}, c_{A2}, c_{B1}, c_{B2})^T$ and its Fourier transform $c_{iM\alpha} = \frac{1}{\sqrt{N}} \sum_{\mathbf{k}} c_{M\alpha}(\mathbf{k}) \times \exp\left(i\mathbf{R}_{iM} \cdot \mathbf{k}\right)$ for the normal state k-space. The kinetic energy is then given by the minimal hopping Hamiltonian $H^t = \sum_{\mathbf{k}} \psi^\dagger(\mathbf{k})\, W_{\mathbf{k}}\, \psi(\mathbf{k})$ in the 2-Fe unit cell of the 1^{st} BZ, $-\pi < k_x(k_y) < \pi$, where M=(A,B) and $\mathbf{R}_{iM}$ is the position of the Fe atoms in the A (B) sublattice, α=(1,2) stands for d_{xz} / d_{yz} orbitals, and

$$W_{\mathbf{k}} = \begin{pmatrix} \xi_{A1} - \mu & \xi_{12} & \xi_t & \xi_c \\ \xi_{12} & \xi_{A2} - \mu & \xi_c & \xi_t \\ \xi_t & \xi_c & \xi_{B1} - \mu & \xi_{12} \\ \xi_c & \xi_t & \xi_{12} & \xi_{B2} - \mu \end{pmatrix}. \tag{3.1}$$

First, we compare Zhang's minimal model H_1^t, which satisfies only conditions **I** and **III**, with our extended model H_2^t, which satisfies conditions **I** through **III** [86]:

$$\begin{aligned} \mathbf{H_1^t}: \;& \xi_{A1} = \xi_{A2} = \xi^H, \quad \xi_{B1} = \xi_{B2} = \xi^V, \\ & \text{with } t_{1-6} = (-1, -0.4, 2, -0.04, 0, 0). \\ \mathbf{H_2^t}: \;& \xi_{A1} = \xi_{B2} = \xi^H, \quad \xi_{A2} = \xi_{B1} = \xi^V, \\ & \text{with } t_{1-6} = (-1, 0.08, 1.35, -0.12, 0.09, 0.25). \end{aligned} \tag{3.2}$$

Here, we defined the dispersion functions: $\xi^H = 2t_2\cos(k_x) + 2t_3\cos(k_y) + 4t_6\cos(k_x)\cos(k_y)$, $\xi^V = 2t_3\cos(k_x) + 2t_2\cos(k_y) + 4t_6\cos(k_x)\cos(k_y)$, $\xi_{12} = 2t_4\cos(k_x) + 2t_4\cos(k_y)$, $\xi_t = 4t_1\cos(k_x/2)\cos(k_y/2)$, $\xi_c = 4t_5\cos(k_x/2)\cos(k_y/2)$. Fig. 3.1(b) shows the schematic picture of H_2^t. The key difference between both models is the orientation of orbitals, which is identical for the A and B sublattices in Zhang's model, while here the combination of conditions **I** and **II** results in a 90° relative orbital rotation (*twist*) between both sublattices (see Appendix B. for more details of the symmetry and Appendix C. for the twist argument). The parameters for H_1^t are taken from Ref. [19]. In the case of H_2^t, we determine the hopping parameters by comparing the calculated FS topologies to the angle-resolved photoemission (ARPES) experiments [75] for electron fill factors $n = 2.0$ (half filling), $n = 1.8$ (optimal h-doping) and $n = 1.5$ (KFe_2As_2). The dispersions also agree qualitatively with many LDA calculations for both e- and h-doped compounds [65, 68, 71, 78, 79], thus the model is not restricted to $BaFe_2As_2$. In Fig. 3.2(a) and (b) we plot the band dispersion for H_1^t and H_2^t, respectively. Note the significant difference between the electronic dispersions of these Hamiltonians, which is seen in the insets of Fig. 3.2(a) and (b), where we enlarge the relevant area around the M point in the BZ. In the case of (b) a linear dispersion (Dirac cone) can be found for model H_2^t, while none exists for model H_1^t in (a). As will become clearer, this key difference between Zhang's H_1^t model and the new H_2^t model is a direct consequence of condition **II**.

3.3 Multi-orbital mean-field Hamiltonian

In the next step, we construct the minimal mean-field Hamiltonian in the weak-coupling regime. Since the C-AFM will enlarge the real-space unit cell, we need to choose the 4-Fe unit cell configuration as shown in Fig. 3.1(a), with the real-space Hamiltonian, $H = H^t + H^\Delta + H^{int}$. Here H^t is the hopping term, H^Δ is the 2NN intra-orbital pairing interaction and H^{int} is the interaction term, which includes the Coulomb interaction U and Hund's coupling J_H. We note that the effect of Coulomb interaction dominant on these two low-energy orbitals has been discussed for antiferromagnetism [7, 19]. Here, the hopping Hamiltonian H^t is expressed by

$$H^t = \sum_{i\alpha j\alpha'\sigma} (t_{i\alpha j\alpha'} c^\dagger_{i\alpha\sigma} c_{j\alpha'\sigma} + h.c) - \mu \sum_{i\alpha\sigma} c^\dagger_{i\alpha\sigma} c_{i\alpha\sigma}, \tag{3.3}$$

where i and j are site indices of each Fe site, α=(1,2) is the orbital index, $\sigma = (\uparrow, \downarrow)$ is the spin index and μ is the chemical potential. The detail of these hopping terms is giving in Fig. 3.1(b). The second term in H is the mean-field superconducting (SC) pairing Hamiltonian,

$$H^\Delta = \sum_{ij\alpha\sigma} (\Delta_{ij\alpha} c^\dagger_{i\alpha\sigma} c_{i\alpha\bar{\sigma}} + h.c). \tag{3.4}$$

The third term in H is the on-site Coulomb interaction Hamiltonian including Hund's coupling. Following Ref. [87] we write,

$$\begin{aligned} H^{int} =& U \sum_{i\alpha\sigma\neq\bar{\sigma}} \langle n_{i\alpha\bar{\sigma}} \rangle n_{i\alpha\sigma} \\ &+ U' \sum_{i,\alpha\neq\alpha',\sigma\neq\bar{\sigma}} \langle n_{i\alpha\bar{\sigma}} \rangle n_{i\alpha'\sigma} \\ &+ (U' - J_H) \sum_{i,\alpha\neq\alpha',\sigma} \langle n_{i\alpha\sigma} \rangle n_{i\alpha'\sigma}, \end{aligned} \tag{3.5}$$

where $n_{i\alpha\sigma} = c^\dagger_{i\alpha\sigma} c_{i\alpha\sigma}$ and U'=$U - 2J_H$. After performing the Bogoliubov transformation of the electrons onto particle-hole excitations with $c_{i\alpha\sigma} = u^n_{i\alpha\sigma}\gamma_n + \sigma\, v^{n*}_{i\alpha\sigma}\gamma^\dagger_n$, the corresponding Bogoliubov-de Gennes (BdG) Hamiltonian can be written in matrix form and solved self-consistently,

$$\sum_{j\alpha'} \begin{bmatrix} H_{i\alpha j\alpha'\uparrow} & \Delta_{ij\alpha'} \\ \Delta^*_{ij\alpha'} & -H_{i\alpha j\alpha'\downarrow} \end{bmatrix} \begin{bmatrix} u^n_{j\alpha'\uparrow} \\ v^n_{j\alpha'\downarrow} \end{bmatrix} = E^n \begin{bmatrix} u^n_{i\alpha\uparrow} \\ v^n_{i\alpha\downarrow} \end{bmatrix}, \tag{3.6}$$

with particle-like ($u^n_{i\alpha\uparrow}$) and hole-like ($v^n_{i\alpha\downarrow}$) wave functions.

The self-consistent mean-field equations for the SC order parameter and spin-up and spin-down occupations are given by

$$\Delta_{ij\alpha} = \frac{V_{ij}}{4} \sum_n (u^n_{i\alpha\uparrow} v^{n*}_{j\alpha\downarrow} + u^n_{j\alpha\uparrow} v^{n*}_{i\alpha\downarrow}) \tanh\left(\frac{E_n}{2k_B T}\right), \tag{3.7}$$

where

$$\langle n_{i\alpha\uparrow}\rangle = \sum_n |u^n_{i\alpha\uparrow}|^2 f(E_n), \tag{3.8}$$

and

$$\langle n_{i\alpha\downarrow}\rangle = \sum_n |v^n_{i\alpha\downarrow}|^2 [1 - f(E_n)]. \tag{3.9}$$

For simplicity, we consider second-nearest-neighbor (2NN) intra-orbital pairing only with pairing potential V_{ij}=V. To facilitate the discussion of physical observables and generating of the phase diagram, we define the staggered lattice magnetization and the s-wave and d-wave projections of the order parameter on the lattice:

$$m_i = \frac{1}{4} \sum_\alpha (\langle n_{i\alpha\uparrow}\rangle - \langle n_{i\alpha\downarrow}\rangle), \tag{3.10}$$

$$\Delta_s = \frac{1}{8N} \sum_{i,\delta,\alpha} \Delta_{i,i+\delta,\alpha}, \tag{3.11}$$

$$\Delta_d = \frac{1}{8N} \Big| \sum_{i,\delta,\alpha} \epsilon_x \, \epsilon_y \, \Delta_{i,i+\delta,\alpha} \Big|. \tag{3.12}$$

The neighbors of site i are reached by $\delta = (\hat{x} + \hat{y}, \hat{x} - \hat{y}, -\hat{x} + \hat{y}, -\hat{x} - \hat{y})$, with $\epsilon_x = \delta \cdot \hat{x}, \epsilon_y = \delta \cdot \hat{y}$; N is the number of Fe sites in the real-space lattice. We note that the x (y) axis is aligned with the short Fe-Fe bond direction.

3.4 Model results

We calculate the phase diagram for both Hamiltonians H_i=$H^t_i + H^{int} + H^{\Delta}$ with $i = 1, 2$ to investigate the stability of the reported C-AFM, SC, and coexisting C-AFM/SC phases as a function of doping parameter. The evolution with doping is described by the same set of hopping, interaction, and pairing parameters for each model across the entire doping range. For model H_1 we use $(U, J_H, V) = (3.4, 1.3, 1.2)$ from Zhou and co-workers [19], while for H_2 a new set of parameters $(U, J_H, V) = (3.2, 0.6, 1.05)$ is used [86] (see Appendix B. for a detail comparison of the phase diagrams under the same parameter set).

Figure 3.3(a) shows the C-AFM and SC order parameters at nearly zero temperature ($T = 10^{-4}$) for models H_1 (top) and H_2 (bottom). We confirm that the phase diagram of e-doped compounds is equally well described by both Hamiltonians in agreement with

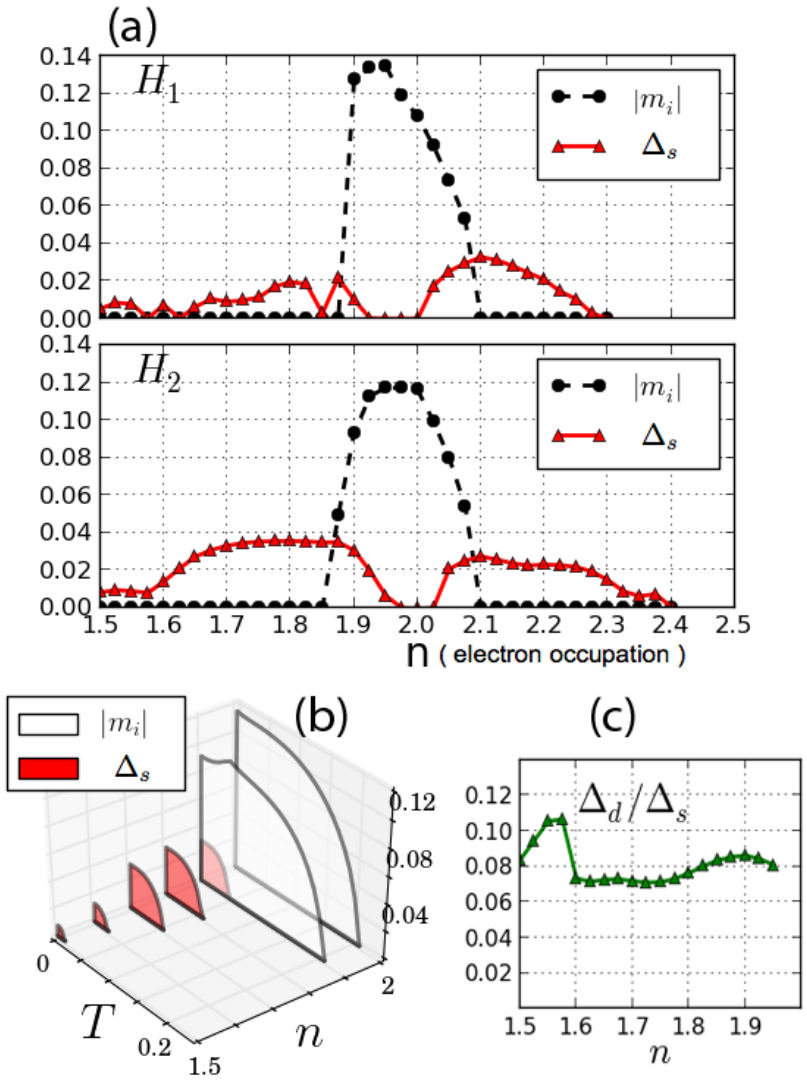

FIGURE 3.3: (color online) The phase diagrams of the C-AFM (m_i) and SC (Δ_s) order parameters of models H_1 (top) and H_2 (bottom) at zero temperature ($T = 10^{-4}$) are shown in panel (a). Panel (b): Temperature (in units of $|t_1|$) dependence of the calculated order parameters of model H_2. The suppression of m_i is visible in the coexistence region with Δ_s at filling $n = 1.9$. Panel (c): The ratio of the SC order parameters Δ_d/Δ_s for 2NN pairing is shown for H_2. The d-wave admixture is of order 8% over the entire h-doping regime ($n = 1.5 - 2.0$).

experiments [51, 72–74, 88]. However, the situation is markedly different on the h-doped side. Here only H_2 is capable of describing experiments [76, 77] by correctly accounting for the e-h asymmetry and the existence of a strong SC phase at low electron filling ($1.6 < n < 1.85$). In Fig. 3.3(b) the finite temperature self-consistent calculations of the C-AFM and SC order parameters are shown for H_2 at h-doping values $n = 1.5, 1.6, 1.7, 1.8, 1.9$ and 2.0 (half filling). We also find that in the coexistence C-AFM/SC phase both orders compete for phase space. The competition leads to a marked suppression of m_i, when Δ_s nucleates at a lower temperature, see Fig. 3.3(b) for fill factor $n = 1.9$. From the self-consistent calculations of the phase diagram, we extract the maximum

gaps: C-AFM gap $m_i/T_N \approx 0.116/0.211 = 0.549$ at $n = 2.0$, and the SC gaps for e-doping $\Delta_s^{exp}/T_c \approx 0.11/0.049 = 2.23$ at $n = 2.1$, and h-doping $\Delta_s^{exp}/T_c \approx 0.14/0.066 = 2.16$ at $n = 1.8$ and $\Delta_s^{exp}/T_c \approx 0.033/0.015 = 2.21$ at $n = 1.5$. Here we introduced $\Delta_s^{exp} \equiv 4\,\Delta_s$ as the experimentally determined tunneling gap. The SC gap ratios are in reasonable agreement with experimental reports for various doping values, ranging from values associated with weak- to strong-coupling pairing, $1.5 \leq \Delta^{exp}/T_c \leq 3.8$ [89–92]. Figure 3.3(c) shows the ratio between Δ_d and Δ_s, which is roughly 8% over the entire h-doping region. Although the $s^{\pm}$ gap symmetry is the most widely accepted pairing symmetry for Fe-122 based SCs [93, 94], we always find a small admixture of d-wave symmetry in our self-consistent mean-field calculations. This was also observed in recent heat conduction experiments [95]. For a lattice model with D_{2d} symmetry both s- and d-wave belong to the same representation and are allowed to mix. This admixture is also found in Zhang's model, H_1, however, there the C_4 symmetry breaking is only due to condition **I**, while for model H_2 it is related to condition **I** and the 2NN hopping terms of condition **II**.

The pairing symmetry can be discussed more systematically by how it affects the spectral function observed in ARPES experiments. Since we are interested in the entire doping range of the phase diagram, we focus only on the H_2 model. The discussion can be further simplified by neglecting the coexistence region of C-AFM/SC. In that case, we can downfold the BdG Hamiltonian from the 4-Fe unit cell onto the 2-Fe unit cell configuration, see Fig. 3.1(a). The order parameters Δ_s and Δ_d were previously defined on the lattice. Their Fourier transforms in the BZ of the 2-Fe unit cell are $\Delta_s(\mathbf{k}) = 2\,\Delta_s\,[\cos(k_x) + \cos(k_y)]$ and $\Delta_d(\mathbf{k}) = 2\,\Delta_d\,[\cos(k_x) - \cos(k_y)]$. We can further decompose them into sublattice (A,B) and orbital (1,2) contributions:

$$\begin{aligned} \Delta_{A1}(\mathbf{k}) = \Delta_{B2}(\mathbf{k}) = \Delta_s(\mathbf{k}) + \Delta_d(\mathbf{k}), \\ \Delta_{A2}(\mathbf{k}) = \Delta_{B1}(\mathbf{k}) = \Delta_s(\mathbf{k}) - \Delta_d(\mathbf{k}). \end{aligned} \tag{3.13}$$

Note these expressions are a consequence of the twofold D_{2d} symmetry, thus giving rise to the $s_{x^2+y^2} \pm d_{x^2-y^2}$-wave gap. The corresponding downfolded k-space BdG Hamiltonian attains the eigenvalues and eigenvectors for the spectral function of each orbital and sublattice,

$$A_{i\alpha}(\mathbf{k},\omega) = \sum_{n=1}^{8} |u^n_{i\alpha\uparrow}(k)|^2 \delta(\omega - E^n_k) + |v^n_{i\alpha\downarrow}(k)|^2 \delta(\omega + E^n_k), \tag{3.14}$$

where the total spectral function, measured in ARPES, is given by the sum $A(\mathbf{k},\omega) = \sum_{i,\alpha} A_{i\alpha}(\mathbf{k},\omega)$. An obvious question is what is the evolution of the spectral function with doping and how is it affected by the order parameters Δ_s and Δ_d for filling factors $n = 2.1, 1.8$ and 1.5. In Fig. 3.4 the total spectral function and its partial

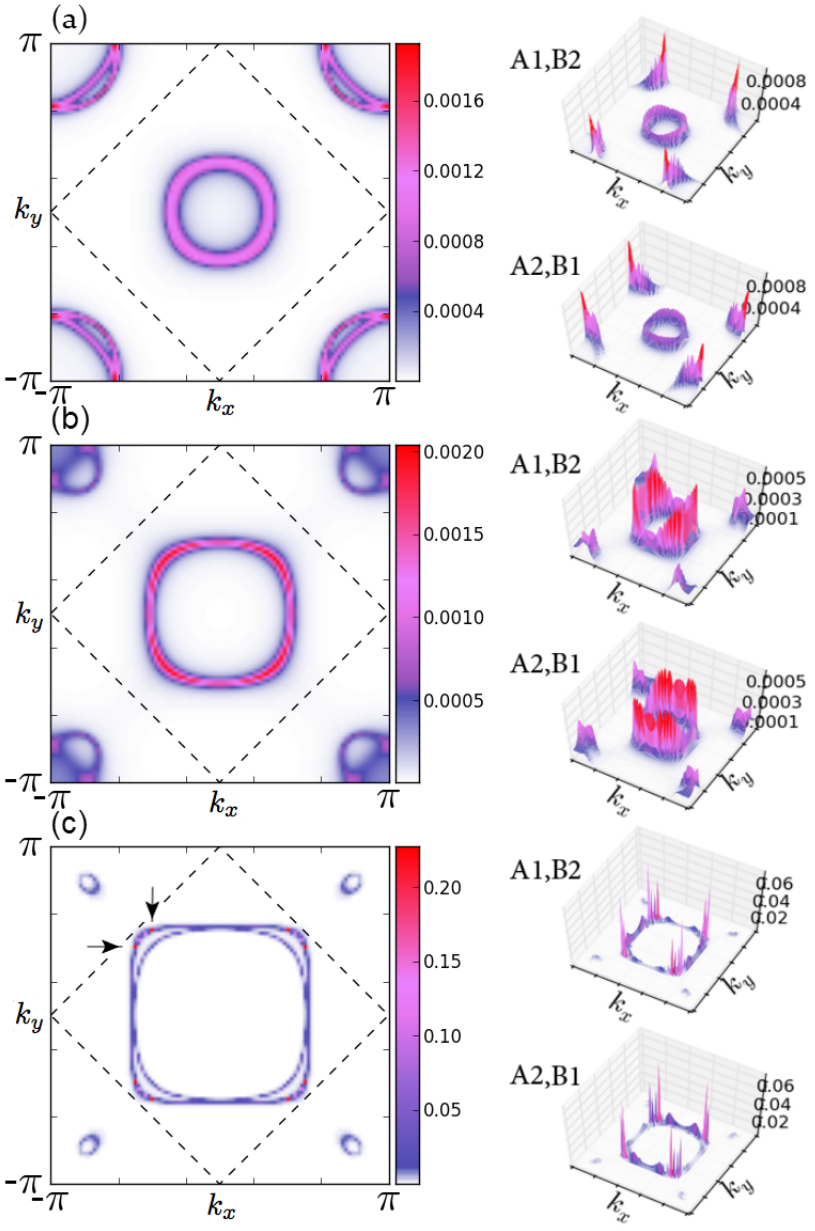

FIGURE 3.4: (color online) Spectral functions at zero temperature at the Fermi level for fill factors $n = 2.1$ (a), $n = 1.8$ (b), and $n = 1.5$ (c). In each panel the total weight of the spectral function is shown in the left column, while the right column shows the corresponding partial spectral functions for each orbital and sublattice. The total spectrum is the sum of all four partial spectra. Panel (c): The two arrows mark the peaks of the electronic hot spots responsible for the octet gap structure. The dashed line shows the nodes of $\Delta_s(\mathbf{k}) = 0$.

weights are shown. The reduced D_{2d} symmetry is obvious from plots of spectral weights A_{A1}, A_{A2}, A_{B1} and A_{B2}. By construction of the model, the 90° rotational symmetry breaking (*twist*) is revealed by the distinction between $A_{A1(B2)}$ and $A_{A2(B1)}$ (right panels in Fig. 3.4). Unfortunately, ARPES experiments cannot differentiate between them. However, one can compare the total spectral functions (left panels of Fig. 3.4) with ARPES experiments. The spectral weights are very small for $n = 2.1$ and $n = 1.8$, indicating that quasiparticles are gapped. The hole pockets around the Γ point exhibit an isotropic gap for $n = 2.1$, while an anisotropic gap with fourfold modulation is found for $n = 1.8$. On the other hand, for $n = 1.5$ (corresponding to KFe_2As_2), we observe eight quasiparticle hot spots at the corners of the large hole Fermi surface centered at Γ, as well as four small pockets near the M point. We believe that the hot spots indicate either the existence of nodal octet structure or highly anisotropic gap.

The pairing symmetry in KFe_2As_2 has been a recent topic of hot debate. The existence of only hole pockets has motivated earlier theoretical proposals of d-wave pairing symmetries with gap nodes [96, 97]. This would imply a change in the superconducting symmetry from s- to d-wave pairing as hole doping is increased. So far there is some experimental evidence for gap nodes [95, 98–100]. However, more recent angle-resolved photoemission spectroscopy unveiled that KFe_2As_2 is a nodal s-wave superconductor with octet-line node structure on the large hole pockets at $k_z = \pi$ [101]. Our model calculations are consistent with an octet nodal structure on the zone-centered hole pocket at $k_z = 0$. However, the eight electronic hot spots at the corners of the large hole Fermi surface in the spectral function do not rule out a highly anisotropic gap. Future ARPES measurements at $k_z = 0$ may resolve the current disagreement about the location of hot spots vs. nodal points between our results and experiments.

3.5 Summary

We have shown how the C_4 symmetry breaking, involving the As atoms below and above the Fe layer, leads to a natural extension of Zhang's minimal model for the Fe-122 superconductors. The new tight-binding model is in better agreement with experiments and density functional theory calculations over the entire doping range. Within the weak-coupling theory of superconductivity, the calculated phase diagram reproduces qualitatively the e-h doping asymmetry reported in many experiments and the gap-over-T_c ratios. In addition, we always find a small d-wave admixture of roughly 8% to a dominant s-wave SC order parameter. This admixture can give rise to quasiparticles in the spectral function resembling nodal excitations at electronic hot spots in the spectral function of KFe_2As_2. Finally, the new minimal model is computationally more efficient than similar five-band models for studying disorder effects in real space around impurities or magnetic vortices.

Chapter 4

Evolution of the Fermi surface topology in doped 122 iron pnictides

4.1 Introduction

So far, we've investigated the entire phase diagram in **chapter 3.**, however, these Fermi surface evolution was only able compare to LDA calculations and experiments in *normal* state. One can observe that, by doping either electrons or holes into the parent compound, the SDW order becomes weakened and the superconductivity (SC) emerges. Both phases appear to coexist with each other in some doping regimes [51, 72–74, 76, 77, 88, 102], even though controversy still remains about their coexistence [103]. Due to the nature of SDW order which enlarge the real space translational symmetry, the k-space BZ should be folded under the SDW phase. Therefore, it would be interesting to monitor the Fermi surface evolution under the SDW order and compare these calculated Fermi surfaces with experiments. This study could help gain insights that how the Fermi surfaces evolution give a stable $s_{\pm}$ pairing symmetry in theories [78, 104, 105] as well as in many experiments [106–108].

In **chapter 3.**, I improved the original model in Ref. [13] to give a unified description of the entire phase diagram covering both the electron- and hole-doped regimes. This is so far the only phenomenological 2-by-2-orbital model (2 Fe sites with 2 orbitals each), in which the resultant low-energy electronic dispersion agrees qualitatively well with density functional theory calculations of the electronic structure in the local density approximation (LDA) of the entire Brillouin zone (BZ) of the 122 compounds [9, 65, 78, 83, 109]. Notably, the obtained phase diagram also agrees with the experimentally observed electron- and hole-doped phase diagrams [51, 72–74, 76, 77, 88]. In this chapter, I keep using this new model to test further its validity by studying the FS topology of

the hole-doped and electron-doped compounds. At the same time I also compare the model results with experiments and with previous theoretical studies [17, 19, 81, 110].

4.2 Model and formalism

We write the model Hamiltonian as [15]

$$H = H_t + H_{int} + H_\Delta, \tag{4.1}$$

where H_t and H_{int} are the single electron hopping and on-site electron-electron interaction terms, respectively. The kinetic energy term can be written as $H_t = \sum_{\mathbf{i}\mu\mathbf{j}\nu\sigma}(t_{\mathbf{i}\mu\mathbf{j}\nu} c^\dagger_{\mathbf{i}\mu\sigma} c_{\mathbf{j}\nu\sigma} + h.c.) - t_0 \sum_{\mathbf{i}\mu\sigma} c^\dagger_{\mathbf{i}\mu\sigma} c_{\mathbf{i}\mu\sigma}$, and the electron-electron interaction term can be expressed in the mean-field approximation by $H_{int} = U \sum_{\mathbf{i},\mu,\sigma\neq\bar{\sigma}} \langle n_{\mathbf{i}\mu\bar{\sigma}}\rangle n_{\mathbf{i}\mu\sigma} + U' \sum_{\mathbf{i},\mu\neq\nu,\sigma\neq\bar{\sigma}} \langle n_{\mathbf{i}\mu\bar{\sigma}}\rangle n_{\mathbf{i}\nu\sigma} + (U' - J_H) \sum_{\mathbf{i},\mu\neq\nu,\sigma} \langle n_{\mathbf{i}\mu\sigma}\rangle n_{\mathbf{i}\nu\sigma}$, where $\mathbf{i}$, $\mathbf{j}$ are lattice site indices; $\mu, \nu = 1, 2$ are the orbital indices for d_{xz} and d_{yz} orbitals; t_0 is the chemical potential, which is determined by the electron filling per site n with $n_{\mathbf{i}\mu\sigma} = c^\dagger_{\mathbf{i}\mu\sigma} c_{\mathbf{i}\nu\sigma}$ and $U' = U - 2J_H$. At the mean field level, the pairing term is given by $H_\Delta = \sum_{\mathbf{i}\mu\mathbf{j}\nu\sigma}(\Delta_{\mathbf{i}\mu\mathbf{j}\nu} c^\dagger_{\mathbf{i}\mu\sigma} c_{\mathbf{j}\nu\bar{\sigma}} + h.c.)$. Since this is a phenomenological Hamiltonian and dispersions are fit to low-energy LDA calculations or ARPES measurements, our classification in terms of d_{xz} and d_{yz} orbitals should not be taken literal, but rather as a convenient way to differentiate between the symmetries of the effective low-energy orbitals.

The Hamiltonian in Eq. (4.1) is solved self-consistently through the multiorbital Bogoliubov-de Gennes equations in matrix notation,

$$\sum_{\mathbf{j}\nu} \begin{pmatrix} H_{\mathbf{i}\mu\mathbf{j}\nu\uparrow} & \Delta_{\mathbf{i}\mu\mathbf{j}\nu} \\ \Delta^*_{\mathbf{i}\mu\mathbf{j}\nu} & -H^*_{\mathbf{i}\mu\mathbf{j}\nu\downarrow} \end{pmatrix} \begin{pmatrix} u^n_{\mathbf{j}\nu\uparrow} \\ v^n_{\mathbf{j}\nu\downarrow} \end{pmatrix} = E_n \begin{pmatrix} u^n_{\mathbf{i}\mu\uparrow} \\ v^n_{\mathbf{i}\mu\downarrow} \end{pmatrix}, \tag{4.2}$$

in combination with the self-consistency equations for the electron density,

$$n_{\mathbf{i}\mu} = \sum_n |u_{\mathbf{i}\mu\uparrow}|^2 f(E_n) + \sum_n |v_{\mathbf{i}\mu\downarrow}|^2 [1 - f(E_n)], \tag{4.3}$$

and the SC order parameter,

$$\Delta_{\mathbf{i}\mu\mathbf{j}\nu} = \frac{V_{\mathbf{i}\mu\mathbf{j}\nu}}{4} \sum_n (u^n_{\mathbf{i}\mu\uparrow} v^{n*}_{\mathbf{j}\nu\downarrow} + u^n_{\mathbf{j}\nu\uparrow} v^{n*}_{\mathbf{i}\mu\uparrow}) \tanh(\frac{E_n}{2k_B T}). \tag{4.4}$$

Here $f(E)$ is the Fermi-Dirac distribution function with Boltzmann constant k_B, $V_{\mathbf{i}\mu\mathbf{j}\nu}$ is the NNN pairing strength, with $V_{\mathbf{i}\mu\mathbf{j}\mu} = V$, when $\mathbf{j} = \mathbf{i} \pm \hat{x}' \pm \hat{y}'$ and zero otherwise.

Throughout this work, we will use the six hopping parameters

$$t_{1-6} = (-1, 0.08, 1.35, -0.12, 0.09, 0.25) \tag{4.5}$$

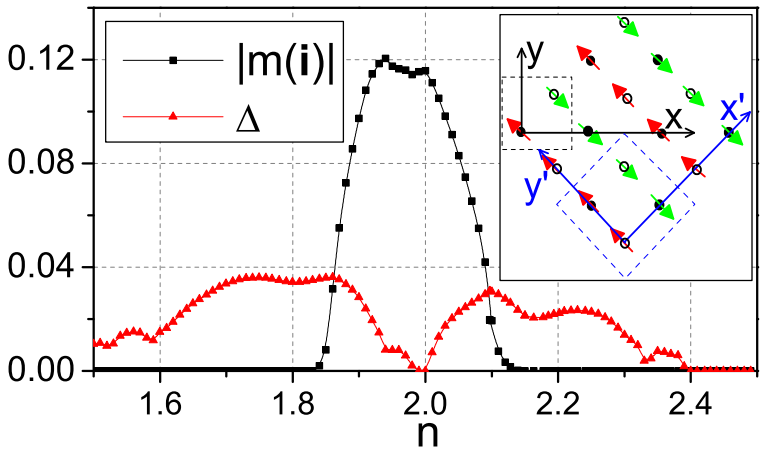

FIGURE 4.1: (Color online) The phase diagram at zero temperature. The collinear SDW order parameter (black line with squares) and the SC order parameter (red line with triangles) are shown. Inset: The schematic lattice structure of the Fe layer in the SDW state is plotted. Solid dots and circles denote nonequivalent Fe ions in different sublattices. Black and blue dashed squares denote the 2-Fe unit cell in the paramagnetic state and 4-Fe unit cell in the SDW state, respectively.

and the three many-body interaction parameters $(U, J_H, V) = (3.2, 0.6, 1.05)$ from Ref. [15]. All energies are measured in units of $|t_1|$. Before we give a detailed discussion about the effects of doping, we present the phase diagram of Tai's model in Fig. 4.1. In these calculations, the collinear SDW order parameter is defined as $m(\mathbf{i}) = (-1)^{\mathbf{i}_{x'}} \frac{1}{4} \sum_{\mu} (n_{\mathbf{i}\mu\uparrow} - n_{\mathbf{i}\mu\downarrow})$, and the bulk SC order parameter is defined as the average over the lattice, $\Delta = \frac{1}{8N} \sum_{\mathbf{i},\hat{\delta},\mu} \Delta_{\mathbf{i},\mathbf{i}+\hat{\delta},\mu}$.

4.3 FS topology and Dirac cones for the undoped case

For the undoped case, the FS in the normal state contains two hole pockets around the $\Gamma = (0, 0)$ point and two electron pockets around the $M = (\pi, \pi)$ point (Fig. 4.2(a)). Since the SDW order will enlarge the real-space unit cell, we choose the 4-Fe unit cell configuration as denoted by the blue dashed squares in the inset of Fig. 4.1, from which we can see that the antiferromagnetic order is along the x′ axis and the ferromagnetic order is along the y′ axis. We plot the zero-temperature magnetic FS of the undoped parent compound, obtained from our self-consistent calculation, in Fig. 4.2(b). Four small FS pockets appear in the magnetic Brillouin zone (MBZ) along the high-symmetry $\Gamma - M$ line, consistent with experiments [111, 112]. We note that the pockets outside the MBZ are just replicas of those inside due to band folding in the SDW state. To reveal the nature of these FS pockets, we make a one-dimensional (1D) cut in Fig. 4.2(c) for the band structures along $X'_{\mathrm{x}} - \Gamma' - X'_{\mathrm{y}}$. We can see that two of the colored FS pockets (red) are electron-type and located around $(k_x, k_y) = \pm(0.287\pi, 0.287\pi)$, while the other two (green) are hole-type and located around $(k_x, k_y) = \pm(0.244\pi, 0.244\pi)$. Along the

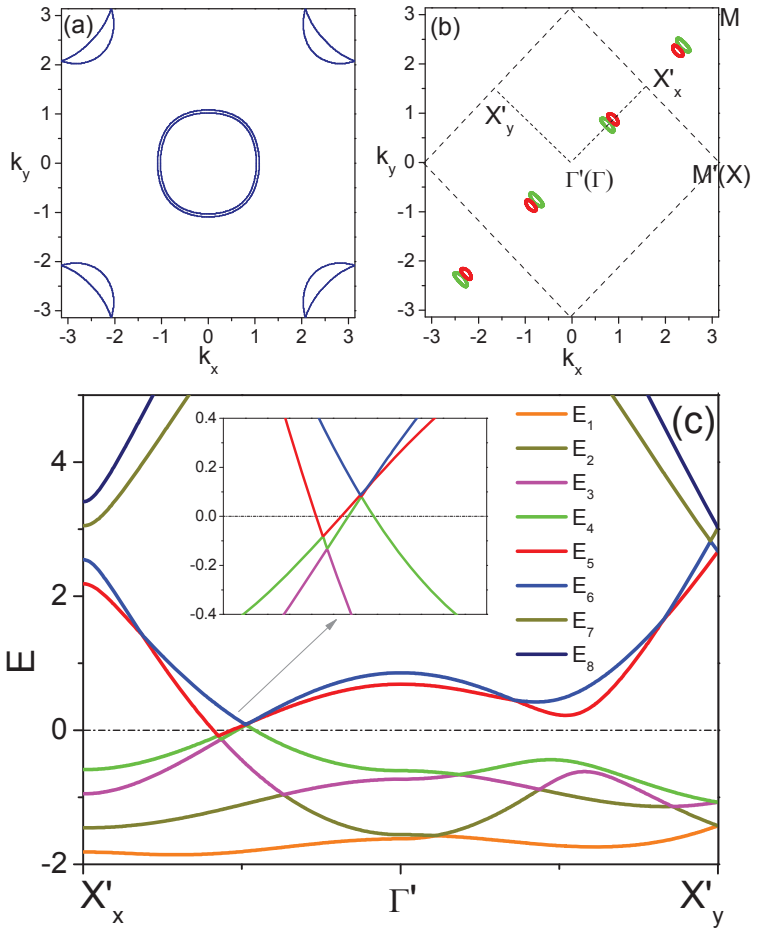

FIGURE 4.2: (Color online) (a) The normal state FS at half filling. (b) The ungapped magnetic FS at half-filling. The dash lines indicate the MBZ boundary in the SDW state. (c) The band structure along two directions $X_{\mathrm{x}}^{'}-\Gamma^{'}$ and $\Gamma^{'}-X_{\mathrm{y}}^{'}$. Inset: Enlarged view of the Dirac cones.

line $X_{\mathrm{x}}^{\prime}-\Gamma^{\prime}$, we predict the existence of two Dirac cones (one electron doped and the other hole doped). Indeed this is captured by recent ARPES experiments [80] and is in good agreement with magneto-resistance measurements [113]. In retrospect, these calculations allow us to justify why the present two-orbital model agrees so well with experiments. This is because the density of states due to the d_{xy} orbital is practically zero at the Fermi energy in the presence of the SDW order [6] and thus may be neglected. Similar features for the parent compound have also been obtained by a different two-orbital model [81].

4.4 Evolution of FS and spectral function with hole/electron doping

The doping effect is expected to have an intimate impact on the FS with SDW order. In underdoped samples, where the SC and SDW orders coexist, earlier work [17] investigated the effect of the SDW strength on the FS topology by keeping the chemical potential (or doping level) fixed. The FS with the SDW in the undoped case has also been shown to sensitively depend on the strength of the onsite Coulomb interaction [110]. Therefore, it is necessary to choose a set of interaction parameters able to fit the phase diagram of the compounds for both electron- and hole-doped cases (see Fig. 1), and then to examine how the FS is changed as the doping level varies. It appears that this issue has only been studied for the electron-doped case[19] based on the model of Ref. [12]. In the following, we first study the FS topology of the hole-doped case by setting the SC order parameter $\Delta = 0$ to better illustrate the impact of the SDW. The effect of the SC is mainly to open a gap on parts of the FS pockets, where the SDW gap closes. Concretely, in the optimally doped state, it can be predicted that $\Delta(\mathbf{k}) = 2\Delta(cos(k_x) + cos(k_y))$ in the BZ of the 2-Fe unit cell. In the coexistence region of SDW and SC, the reconstructed FSs are formed by mixing electron and hole bands but the SDW wave retains the gapped nature of the $s_{\pm}$-wave SC although the gap equation appears in a mathematically different way [17, 18]. According to our numerical calculation, the SDW gap is mainly affected by the doping that destroying the nesting between the Fermi surfaces, not by the presence of the SC. Further, the FS measured in the ARPES experiments for doped SC samples [47, 48, 114] usually did not exhibit the SC gaps.

When the iron pnictides are lightly hole-doped, i.e., away from half filling, the size of the hole pockets is enlarged, while that of the electron pockets is reduced. The electron pockets will then vanish completely at a small doping value as shown in Fig. 4.3(a). By further increasing doping, two new hole pockets appear in the same location where the electron pockets vanished (Fig. 4.3(b)-(c)). This can be easily seen from the inset of Fig. 4.2(c) by shifting the chemical potential downward. It is also worthwhile to point out that the band structure with the SDW depends strongly on the magnitude of the SDW order. When the doping level $\delta n \equiv$2-n$>$ 0.1, an additional pair of ungapped FS pockets appears in the diagonal $k_x = -k_y$ direction (Fig. 4.3(d)). The size of all these hole pockets is enlarged proportional to doping and then the FSs become closed around the Γ point (two blue squares in Fig. 4.3(g)). Meanwhile, the magenta FS pockets are still located along the $k_x = k_y$ direction and stay gapped along the orthogonal direction, $k_x = -k_y$. When the system is even further doped, all the FSs become closed around the Γ point and symmetric along $k_x = k_y$ and $k_x = -k_y$ directions as the SDW order becomes increasingly small (Fig. 4.3(f)). So far we are not aware of any ARPES experiments in the hole-doped region with SDW. Hence, our results will guide

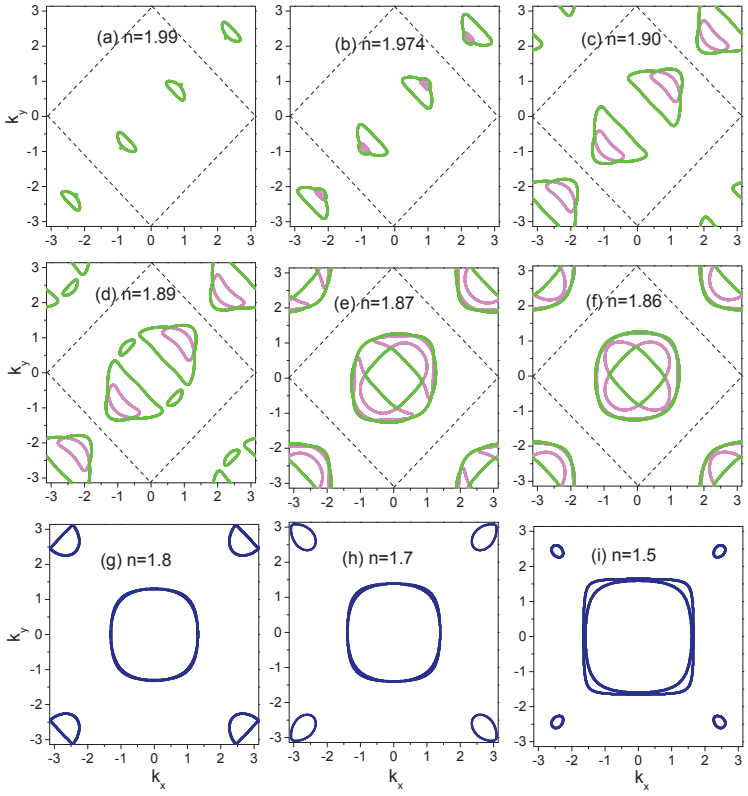

FIGURE 4.3: (Color online) The doping evolution of the FS at the zero temperature on the hole-doped side of the phase diagram. The SC order is artificially set to zero in order to illustrate the effect of the SDW. In panels (a)-(f), the green and magenta lines indicate the ungapped hole-type FS and the black dash lines indicate the MBZ boundary. The royal curves in (g)-(i) show the paramagnetic state FSs due to the totally depression of the SDW order.

the search and interpretation of future experiments of the FS topology with SDW phase in the very underdoped regime. In this regime, the SDW gap is large while the SC gap is comparatively small. If the ARPES experiment observes small gaps in certain k space-region while large gaps are detected in other part of the k space then the FS where the SC resides on could be easily determined. If one neglects the smaller SC gap, the FS with SDW as a function of doping should be experimentally obtained, and the results should be used to compare with our theoretical predictions. However near the optimal doped sample where the gaps of the SDW and SC are of the same magnitude, it would be hard for our theory to fit the experiments except in the regime where the SC gap is much larger than the SDW gap.

For samples with $n \leq 1.86$, or $\delta n \geq 0.14$, the SDW order disappears and thus no more band folding. We show the corresponding FSs in the 2-Fe BZ at $n = 1.8$, $n = 1.7$ and $n = 1.5$ in Figs. 4.3(g)-(i), respectively. The four electronic pockets at the zone corner M shrink, while the hole pockets at Γ expand a little with increasing doping. It should be noticed that for extremely hole-doped samples, the small electron pockets

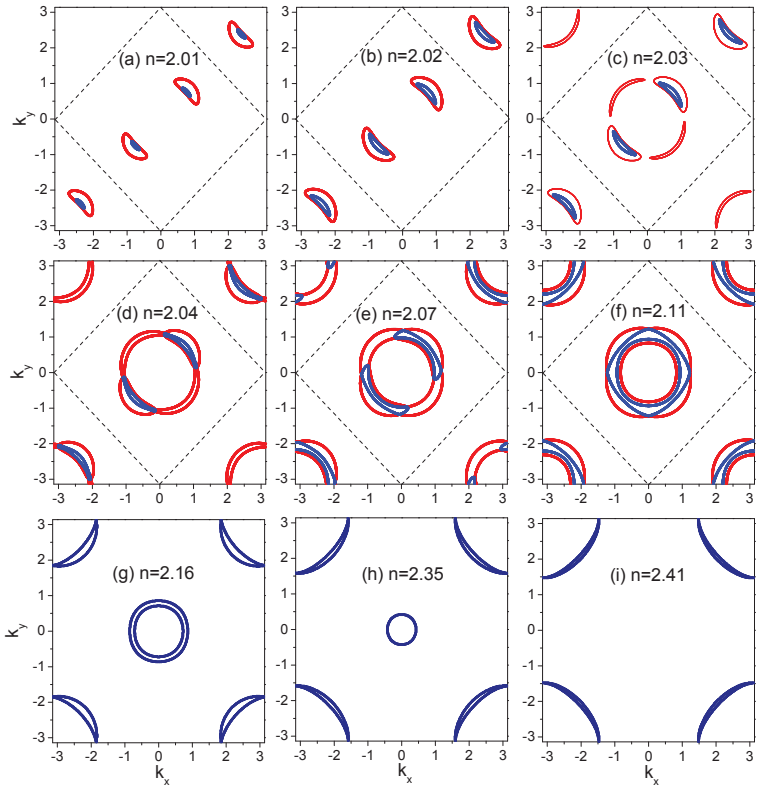

FIGURE 4.4: (Color online) Similar to Fig. 3, but for the electron-doped side. The red and blue lines in panels (a)-(f) indicate the ungapped electronic FS.

near the M points no longer touch the BZ boundary, which is consistent with available ARPES experiments [75, 115], and so far has not yet been explained by other two-orbital models. In addition, Fig. 4.3(g) shows nearly degenerate hole-like FSs at the Γ point, while experiments indicate two well separated hole like FSs [75, 80, 115–118]. This is an intrinsic shortcoming of the two-orbital model, because the outer hole pocket (β FS sheet), which is missing in the present calculation, has a major d_{xy} orbital component according to orbital-sensitive ARPES results [119]. On the other side, the LDA calculations [7, 120, 121] have shown that, although heavily hybridized, the main character of the bands that determine the FS are d_{xz} and d_{yz} orbitals, with small contributions of d_{xy} at the hole pockets and at most the elongated portions of the electron pockets. This fact may qualitatively justify the proposal of the two-orbital model as the phenomenological, minimum orbital model for the 122 pnictides to capture the SDW and SC order.

In order to check the validity of the two-orbital model employed in the present work, we also examine the FS evolution with electron doping. The results are shown in Fig. 4.4. In the lightly doped regime, the hole pockets are gradually getting smaller and finally disappear. With further increased doping, two electron pockets appear (see Figs. 4.4(a) and (b)). This behavior is mirrored for hole doping and can be seen from the inset of Fig. 4.2(c) by moving the chemical potential upward. However, in the

intermediate doping regime around $n = 2.03$, two new electron FS arcs also appear along the diagonal $k_x = -k_y$ direction, see Fig. 4.4(c). This is quite different from the two-band result in Fig. 2 of Ref. [16], there the magnetic FS pockets are always along the $k_x = k_y$ direction. Recently, ARPES experiments [114] were performed on strongly underdoped $BaFe_{2-x}Co_xAs_2$ samples in which the electronic structure of the detwinned crystal was observed. It can be seen that the anisotropic features in Fig. 4.4(c) and 4.4(d) are qualitatively comparable to the experimental observations as shown in Fig. 1 of Ref. [114], if the crystal orientation across the twin boundaries is considered. When the doping increases, the size of the electron FS pockets and arcs are enlarged, and eventually become large closed FSs around Γ, while the other pair of ungapped FS pockets remains along the Γ-M line (Figs. 4.4(e)). When the system is further doped, the inner blue electron pockets are also closed around the Γ point (Fig. 4.4(f)).

For $n > 2.11$, the SDW order is totally suppressed, and the FS is then presented in the 2-Fe BZ, as shown in Fig. 4.4(g)-(i). It can be seen that in the heavily electron-doped sample, the hole-like FSs around the Γ point become very small. First the inner one disappears, and finally both hole FSs disappear while the electron FS pockets at the zone corner become enlarged. A key finding of this work is that all these model results are consistent with ARPES experiments [47, 48]. In addition, the shape of the FS pockets around the M point are round, while those obtained in previous work were more square [19].

For a direct comparison to future experimental studies with varying doping levels, we calculate the spectral function $A(\mathbf{k},\omega) = \sum_{\mathbf{i},\mu} A_{\mathbf{i},\mu}(\mathbf{k},\omega)$, and integrate from $\omega = -0.1$ to 0.1, which is proportional to the photoemission intensity measured in ARPES experiments. The local and orbital-resolved spectral function is defined as

$$A_{\mathbf{i},\mu}(\mathbf{k},\omega) = \sum_n [|u_{\mathbf{i}\mu\uparrow}(\mathbf{k})|^2 \delta(E_n(\mathbf{k}) - \omega) + |v_{\mathbf{i}\mu\downarrow}(\mathbf{k})|^2 \delta(E_n(\mathbf{k}) + \omega)]. \tag{4.6}$$

Our calculated spectral functions are shown in Fig. 4.5. It is known that when the sample is undoped or in the lightly hole- or electron-doped regimes, the spectral intensity is strong along the diagonal direction $k_x = k_y$ direction, but very weak along the other diagonal direction, $k_x = -k_y$ [111, 112]. When the electron or hole doping is increased, the intensity along $k_x = -k_y$ becomes enhanced (Figs. 4.5(b), 4.5(d), and 4.5(e)), with obvious anisotropic characteristics induced by the existence of the SDW order. In the paramagnetic phase, as seen from Figs. 4.5(a) and 4.5(f), the FSs become symmetric along the $k_x = k_y$ and $k_x = -k_y$ directions.

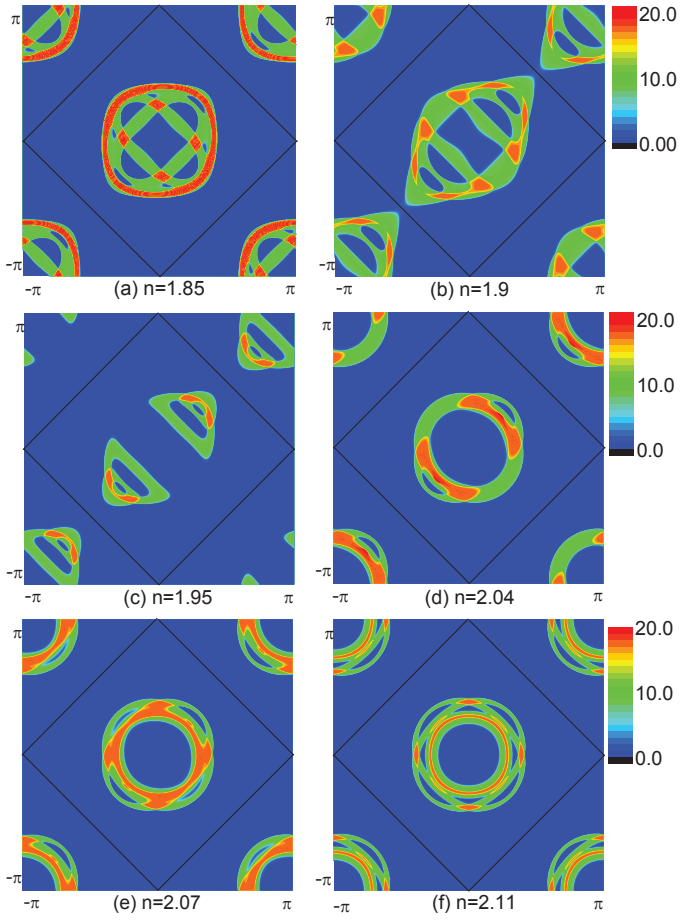

FIGURE 4.5: (Color online) The spectra function $A(\mathbf{k}, \omega)$ integrated from $\omega = -0.1$ to 0.1 at different doping levels: (a) $n = 1.85$, (b) $n = 1.9$, (c) $n = 1.95$, (d) $n = 2.04$, (e) $n = 2.07$, and (f) $n = 2.11$.

4.5 Summary

In summary, we have studied for the first time systematically the FS evolution of the 122 parent compound as functions of hole- and electron-doping. At zero doping, there exist equal-sized electron-doped and hole-doped Dirac cones along the Γ-M direction ($k_x = k_y$) in the BZ, i.e., the direction of the antiferromagnetic order. This is in good agreement with experiments. When the 122 parent compound is lightly doped, the effect of hole-doping is mainly to reduce the size of the Dirac cone-like pockets, while the SDW gap closes up along the antiferromagnetic nesting direction. With further doping, additional parts of FSs becomes ungapped along the orthogonal direction, $k_x = -k_y$. Then the SDW order is completely suppressed and the complete two-dimensional FSs appear in the heavily hole-doped sample. We noticed that the FSs obtained for the heavily hole-doped regime seem not to agree well with ARPES experiments, this is because the contribution from the d_{xy} orbital is not adequately captured in the present study. However, our results with the SDW order can be used to guide future experiments on

the evolution of the Fermi surface topology in very underdoped samples of Fe-pnictides, where the d_{xy} orbital is greatly suppressed. On the other hand, we have also investigated the FS evolution as a function of electron doping. All of our theoretical findings in this case are in qualitative agreement with experiments from under-doped to over-doped regime. This conclusion implies that the present model suits better for the electron-doped case than for the hole-doped case. Finally we believe that the low energy physics of the 122 pnictides is originating mainly from the d_{xz} and d_{yz} orbitals, and further works are needed to support the validity of the present model.

Chapter 5

Disorder effects in multiorbital $s_{\pm}$-wave superconductors: Implications for Zn-doped $BaFe_2As_2$ compounds

5.1 Introduction

Our calculations in **chapter 4.** partly indicated that the generic phase diagram of the iron-based superconductors (Fe-SCs) suggests the close proximity [49] of the superconductivity (SC) to the SDW order. This should be contrasted with high-temperature cuprates, of which the SC originates from an AFM Mott insulator phase and can be quickly suppressed by substitution with other $3d$-transition-metal atoms into the CuO_2 plane. Instead, the SC in the Fe-SCs can be induced when Fe atoms are partially replaced by $3d$-transition-metal atoms like Ni and Co [122–129]. Moreover, in the case of the electron- and hole-doped 122 family like $Ba(Fe_{1-x}Co_x)_2As_2$ or $Ba_{1-x}K_xFe_2As_2$, the coexistence of the SDW and SC in a narrow doping region is reported by both experiments [122, 130] and theoretical calculations [81, 131]. It has been argued that owing to their multiorbital nature and variable correlation effects, the superconducting pairing symmetry may not be universal in the Fe-SCs [93, 132, 133]. This certainly poses a great challenge to relating the symmetry of the order parameter and the canonical doping phase diagram across different crystallographic iron-pnictide families. Therefore, detailed measurements of the bulk transport and superconducting properties will remain useful for determining the superconducting pairing symmetry in the Fe-SCs.

While superconductivity can be induced in the 122 family by substitution of Fe with Co or Ni (and many other $3d$ transition metals [134–137]) in the FeAs layer, the role of these electron dopants is still controversial [138–142]. It is hotly debated whether

such substitution is dominated by the doping effect of extra charge carriers or impurity scattering or a combination thereof [143]. In general, the study of disorder effects in superconductors is promising in addressing the pairing symmetry, as it has been applied successfully to the understanding of high-T_c cuprate superconductivity [144]. Therefore, it is natural that the study of impurity scattering effects in Fe-SCs attracted much attention immediately after their discovery. Of particular interest is the case of Zn doping, [145–147] because it does not induce SC, while it is expected to give rise to non-magnetic, strong potential scattering in the unitary limit. For the Zn-doped 122-type iron pnictides, the early results showed that Zn impurities hardly affect the superconductivity of hole-doped $Ba_{0.5}K_{0.5}Fe_2As_2$ [148]. However, more recent measurements of the magnetic susceptibility and resistivity [149, 150] on high-quality single-crystalline $Ba(Fe_{1-x-y}Zn_xCo_y)_2As_2$ compounds, suggested that the electron doped superconductivity is almost fully suppressed above a concentration of roughly 8% Zn, regardless of whether the sample is under, optimally or over doped. This discrepancy with earlier experiments is possibly due to the technical difficulty in substituting Zn for Fe atoms. Further measurements [151] on the hole doped $Ba_{0.5}K_{0.5}(Fe_{1-x}Zn_x)_2As_2$ compound also showed that the superconductivity is suppressed by Zn impurities. These interesting results have presented a challenge to theoretically identify the pairing symmetry in Fe-SCs. So far, the sign-reversal $s_{\pm}$-wave pairing symmetry has been supported by many experiments including neutron scattering [106], angle-resolved photoemission spectroscopy [117], and scanning tunneling spectroscopy [108], and is also consistent with the competition picture between magnetism and superconductivity [103]. However, it has also been shown earlier [138] that because of the sign reversal of superconducting gap function across electron and hole bands, the $s_{\pm}$-wave pairing state is very fragile against impurities while the non-sign-reversal s_{++}-wave pairing symmetry should be a competitive candidate for Fe-SCs. The recent experiment [150] showed that the suppression in the superconducting transition temperature is much slower than that predicated by the theory for the $s_{\pm}$-wave pairing state [138]. More recently, the effect of Zn-doping induced disorder in Fe-SCs with both $s_{\pm}$- and s_{++}-wave pairing symmetries [147] has been investigated by solving the BdG equation for a two-orbital model [12] including both on-site (favoring s_{++}-wave pairing symmetry) and next nearest neighbor (NNN) inter-site (favoring $s_{\pm}$-wave pairing symmetry) pairing interaction. The zero-temperature real-space BdG calculations [147] indicated that the disorder could suppress the NNN pairing order parameter with negligible effect on the on-site pairing order parameter, suggesting a possibility of disorder induced pairing symmetry change from $s_{\pm}$- to s_{++}-wave. As such, depending on the strength of the on-site pairing interaction, this interesting proposal may provide a flexibility to explain various experimental data [145–147].

We note that, in Ref. [147], because the tuning of impurity concentration in the

truly disordered system was actually mimicked by a tuning of the NNN pairing interaction in an impurity-free system, a direct comparison of superconducting transition temperature change with impurity concentration between theory and experiment is impossible. Due to this interpretation gap, there are still several open questions. In this chapter, we will study the disorder effects of the Zn impurity on the superconducting properties of 122-type iron-based superconductors. In particular, we aim to address the question of how the superconducting transition temperature is completely suppressed at 8% of Zn doping in 122-type compounds [149–151]. To fulfill this goal, we start with an improved minimal two-orbital model for Fe-SCs [15]. As in Ref. [147], we solve the BdG equations self-consistently in real space to study the impurity-induced disorder effect, from which the superconducting order parameter, superconducting transition temperature, superfluid stiffness are calculated. We point out that with the sole $s_{\pm}$-wave pairing symmetry, the superconducting transition temperature can be suppressed at an impurity concentration as high as about 10%, which agrees well with the experiments on the $Ba(Fe_{1-x-y}Zn_xCo_y)_2As_2$ compounds [150]. This result is in striking contrast with an earlier prediction that the superconductivity is suppressed already at only 1% of impurity concentration [138]. The root cause for this difference is given as follows: Firstly, first-principles electronic structure calculations suggest that substitution of the nonmagnetic Zn atom in the iron-based 122 superconductors, pushes the Zn-3d impurity level considerably far below the Fe-3d level, namely by about $\sim 8-10$ eV. [143, 152, 153] Hence, Zn substitution should be regarded as a strongly localized defect in the strong scattering (unitary) limit. Such strong potential scattering is supported by more recent angle-resolved photoemission spectroscopy measurements on $Ba(Fe_{1-x}Zn_x)_2As_2$ [154, 155]. Secondly, as shown later by our calculations, the superconducting coherence length can be very short, which is consistent with the experimental observation that Fe-SCs are extremely type-II superconductors with Ginzburg-Landau parameter as large as 250 [127, 156]. In such a case, the applicability of the conventional approach based on the Abrikosov-Gorkov (AG) pair-breaking theory in dilute alloys [157], which assumes a spatially uniform suppression of the impurity-averaged order parameter and Green's functions, is in question. The failure of the AG theory to address consistently the superconducting and transport properties in high-temperature cuprate and some heavy-fermion superconductors with short coherence length is well documented [158, 159]. Therefore, in order to go beyond the applicability of the early theoretical studies and to reveal the interesting physics of highly disordered or *dirty* high-temperature iron-based superconductors, we shall study the nonmagnetic impurity-induced disorder effects in the unitary limit of multiorbital superconductors by solving the lattice BdG equation. This approach has proven to be quite successful in providing a consistent picture for the suppression of superconducting transition temperature and superfluid density in the inhomogeneous high-temperature cuprate and plutonium-based

heavy-fermion superconductors [158–160]. In this chapter, we emphasize the key role of strong electronic inhomogeneity induced by Zn substitution and how it could be probed in the 122 iron pnictides.

The remainder of this chapter is organized as follows: In Sec. 5.2 we introduce the model Hamiltonian and the formalism. To set the stage for the highly disordered materials, the single impurity problem is briefly revisited in Sec. 5.3. The disorder effects of the strong scattering limit on the superconducting order parameter are discussed in Sec. 5.4. In Sec. 5.5, disorder effects on the local density of states and the superfluid density or magnetic penetration depth are discussed. Finally, a brief summary is given in Sec. 5.6.

5.2 Model and formalism

The multiorbital nature of iron-based superconductivity requires the construction of physically-reliable and computationally-efficient, effective-low-energy, multiorbital models. In particular, a simple two-orbital model was first constructed by Raghu and coworkers [12]. The Fermi surface topology resulting from this model captured well the shape reported by angle-resolved photoemission spectroscopy [117]. However, it has some weaknesses in other aspects of the electronic band dispersion. For example, too much imbalance of Fermi velocities on the electron and hole bands has been revealed in the study of the local electronic structure around a single impurity of an $s_{\pm}$-wave superconductor [161]. Several groups [9, 10, 162] have pointed out that one needs at least three orbitals to accurately reproduce the electronic band structure calculated in the density functional theory within the local density approximation (LDA). However, it has also been shown [12, 110] that the other Fe-3d_{xz} and Fe-3d_{yz} orbitals play an important role in the low-energy physics of these materials. On the other hand, it has been argued that the canonical minimal model of the 122-type iron pnictides requires only two irons (2-Fe) with two orbitals, d_{xz} and d_{yz}, per unit cell to account for the effects of the upper and lower As atoms with respect to the two-dimensional plane of the Fe square lattice [13, 14]. It is worthy to mention that these 2-by-2-orbital models have successfully described the behavior of the collinear AFM and its competition with the superconducting order in the electron-doped part of the phase diagram. In **chapter 3.**, I improved the model original proposed in Ref. [13] to give a unified description of the entire phase diagram covering both the electron- and hole-doped regimes[15]. To our knowledge, this is the only 2-by-2-orbital model so far, in which the resultant low-energy electronic energy dispersion agrees well with LDA electronic structure calculations in the entire Brillouin zone of 122-type iron compounds.

Here, we start with the improved 2-by-2-orbital model of Ref. [15]. Interestingly, we wish to point out that this model of 2-by-2 orbitals per unit cell can be mapped exactly

onto two decoupled one-site two-orbital models by recognizing a unitary rotation of orbitals between both Fe sublattices. The technical details of this mapping are given in the Appendix C. We write the complete Hamiltonian for the two-dimensional Fe-square lattice as

$$\mathcal{H} = \mathcal{H}_0 + \mathcal{H}_{\rm I} + \mathcal{H}_{\rm pair} + \mathcal{H}_{\rm imp} \; . \tag{5.1}$$

Here $\mathcal{H}_0$ is the tight-binding Hamiltonian of the normal-state band structure describing hopping between Fe-3d_{xz} and Fe-3d_{yz} orbitals. The lattice Hamiltonian in the real space (see also Appendix C.) is given by

$$\mathcal{H}_0 = \sum_{\mathbf{ij}\alpha\beta\sigma} t_{\mathbf{ij}}^{\alpha\beta} d_{\mathbf{i}\alpha\sigma}^{\dagger} d_{\mathbf{j}\beta\sigma} - \sum_{\mathbf{i}\alpha\sigma} \mu d_{\mathbf{i}\alpha\sigma}^{\dagger} d_{\mathbf{i}\alpha\sigma} \; , \tag{5.2}$$

where $d_{\mathbf{i}\alpha\sigma}^{\dagger}$ creates an electron with spin σ in the effective orbitals $\alpha = 1$ and 2 on the $\mathbf{i}$-th lattice site. We choose the nonvanishing hopping matrix elements as $t_{\pm\hat{x}}^{\alpha\alpha} = t_{\pm\hat{y}}^{\alpha\alpha} = 0.09$, $t_{\pm\hat{x}}^{\alpha\bar{\alpha}} = t_{\pm\hat{y}}^{\alpha\bar{\alpha}} = -1$, $t_{\pm(\hat{x}+\hat{y})}^{11} = t_{\pm(\hat{x}-\hat{y})}^{22} = 1.35$, $t_{\pm(\hat{x}-\hat{y})}^{11} = t_{\pm(\hat{x}+\hat{y})}^{22} = 0.08$, $t_{\pm(\hat{x}\pm\hat{y})}^{\alpha\bar{\alpha}} = -0.12$, $t_{\pm 2\hat{x}}^{\alpha\alpha} = t_{\pm 2\hat{y}}^{\alpha\alpha} = 0.25$. The chemical potential μ is adjusted to give a fixed filling factor.

The local electronic correlations include the on-site Hubbard repulsion of electrons and Hund's rule coupling of spins. They are described by the term $\mathcal{H}_{\rm I}$, which at the mean-field level takes the form

$$\begin{aligned} \mathcal{H}_{\rm I}^{\rm MF} = \quad & U \sum_{\mathbf{i}\alpha\sigma} \langle \hat{n}_{\mathbf{i}\alpha\bar{\sigma}} \rangle \hat{n}_{\mathbf{i}\alpha\sigma} + U' \sum_{\mathbf{i}\alpha\neq\beta\sigma} \langle \hat{n}_{\mathbf{i}\alpha\bar{\sigma}} \rangle \hat{n}_{\mathbf{i}\beta\sigma} \\ & + (U' - J_H) \sum_{\mathbf{i}\alpha\neq\beta\sigma} \langle \hat{n}_{\mathbf{i}\alpha\sigma} \rangle \hat{n}_{\mathbf{i}\beta\sigma} \; . \end{aligned} \tag{5.3}$$

with the on-site Hubbard potential U, the inter-orbital Coulomb repulsion U', and the Hund's rule coupling J_H. The orbital rotation symmetry imposes the constraint $U = U' + 2J_H$. In Eq. (5.1), the term $\mathcal{H}_{\rm pair}$ contains the effective pairing interaction between two electrons on the NNN site. In mean-field theory this can be written as

$$\mathcal{H}_{\rm pair} = \sum_{\mathbf{ij}\alpha} (\Delta_{\mathbf{ij}}^{\alpha} d_{\mathbf{i}\alpha\uparrow}^{\dagger} d_{\mathbf{j}\alpha\downarrow}^{\dagger} + \text{H.c.}) \delta_{\mathbf{i}\pm\hat{x}\pm\hat{y},\mathbf{j}} \; . \tag{5.4}$$

As has been widely discussed in the literature, this NNN-pairing interaction ultimately leads to the proposed $s_{\pm}$-wave symmetry of iron pnictides [9, 78, 105, 163, 164]. Finally, the last term $\mathcal{H}_{\rm imp}$ in Eq. (5.1) describes the scattering potential due to the randomly distributed impurities. We model the disorder term by a local intra-orbital scattering potential

$$\begin{aligned} \mathcal{H}_{\rm imp} \quad = \quad & \sum_{\mathbf{I}\alpha\sigma} \{ W d_{\mathbf{I}\alpha\sigma}^{\dagger} d_{\mathbf{I}\alpha\sigma} + \delta t [d_{\mathbf{I}+(-)\hat{x}\alpha\sigma}^{\dagger} d_{\mathbf{I}+(-)\hat{x}\pm\hat{y}\bar{\alpha}\sigma} \\ & + d_{\mathbf{I}+(-)\hat{y}\alpha\sigma}^{\dagger} d_{\mathbf{I}+(-)\hat{y}\pm\hat{x}\bar{\alpha}\sigma} + \text{H.c.}] \} \; . \end{aligned} \tag{5.5}$$

Here, the impurity means that an Fe atom at lattice site **I** is substituted by Zn atom. Therefore, the on-site energy of the impurity atom is changed and acts as a nonmagnetic potential scattering center which scrambles the crystal momentum. As represented by the first term on the rhs of Eq.. (5.5), we consider only intra-orbital scattering. This simplification is justified by our numerical calculations, which show that inter-orbital scattering processes are irrelevant in the unitary limit. In Eq. (5.5) we explicitly consider the difference in covalent radii of the Zn atom compared to the Fe atom, which is captured by the second term proportional to δt. Therefore, the substitution introduces an additional change in the hopping parameters among the nearest-neighbor Fe sites of the impurity site. In the case of the Zn substitution, in addition to electron doping which can be tuned by the chemical potential, the induced local impurity potential is expected to be much stronger than for other transition metals like Co and Ni. Note that when the impurity potential on the Zn site is very large, the effect caused by a small change in the Fe-Zn hopping integrals is negligible. Hence, the surrounding Fe-Fe bond disorder is the second most important term next to the strength of the impurity potential.

We then diagonalize the mean-field Hamiltonian $\mathcal{H}$ of Eq. (5.1) by solving the BdG equation self-consistently:

$$\sum_{\mathbf{j}\beta} \begin{pmatrix} \mathcal{H}^{\alpha\beta}_{\mathbf{ij}\uparrow} & \Delta^{\alpha}_{\mathbf{ij}}\delta_{\alpha,\beta} \\ \Delta^{\alpha*}_{\mathbf{ji}}\delta_{\alpha,\beta} & -\mathcal{H}^{\beta\alpha}_{\mathbf{ji}\downarrow} \end{pmatrix} \begin{pmatrix} u^n_{\mathbf{j}\beta} \\ v^n_{\mathbf{j}\beta} \end{pmatrix} = E_n \begin{pmatrix} u^n_{\mathbf{i}\alpha} \\ v^n_{\mathbf{i}\alpha} \end{pmatrix} , \tag{5.6}$$

where $\mathcal{H}^{\alpha\beta}_{\mathbf{ij}\sigma} = \tilde{t}^{\alpha\beta}_{\mathbf{ij}} + (U\langle\hat{n}_{\mathbf{i}\alpha\bar{\sigma}}\rangle + U'\sum_{\gamma\neq\alpha\sigma'}\langle\hat{n}_{\mathbf{i}\gamma\sigma'}\rangle - J_H\sum_{\gamma\neq\alpha}\langle\hat{n}_{\mathbf{i}\gamma\sigma}\rangle + W\delta_{\mathbf{I},\mathbf{i}} - \mu)\delta_{\alpha,\beta}\delta_{\mathbf{i},\mathbf{j}}$ is the single-particle Hamiltonian and $\tilde{t}$ includes the effect of the local change in the hopping parameter between Fe sites neighboring he impurities, $\langle\hat{n}_{\mathbf{i}\alpha\uparrow}\rangle = \sum_n |u^n_{\mathbf{i}\alpha}|^2 f(E_n)$, $\langle\hat{n}_{\mathbf{i}\alpha\downarrow}\rangle = \sum_n |v^n_{\mathbf{i}\alpha}|^2[1-f(E_n)]$, and $\Delta^{\alpha}_{\mathbf{ij}} = (V/2)\sum_n\{u^n_{\mathbf{i}\alpha}v^{n*}_{\mathbf{j}\alpha}[1-f(E_n)] - v^{n*}_{\mathbf{i}\alpha}u^n_{\mathbf{j}\alpha}f(E_n)\}\delta_{\mathbf{i}\pm\hat{x}\pm\hat{y},\mathbf{j}}$. Here V is the pairing strength and $f(E)$ is the Fermi-Dirac distribution function. The local superconducting order parameter and charge density at site **i** are defined as

$$\Delta_{\mathbf{i}} = \frac{1}{4}\sum_{\mathbf{j}\alpha}\Delta^{\alpha}_{\mathbf{ij}}\delta_{\mathbf{i}\pm\hat{x}\pm\hat{y},\mathbf{j}} , \tag{5.7a}$$

$$n_{\mathbf{i}} = \sum_{\alpha\sigma}\langle n_{\mathbf{i}\alpha\sigma}\rangle , \tag{5.7b}$$

respectively. Throughout this work, the numerical calculations are performed on a 28×28 square lattice with the periodic boundary condition. A 48×48 supercell is taken to calculate the density of states. The interaction parameter values are fixed at $(U, J_H, V) = (3.2, 0.6, 1.05)$ [15]; while the electron filling is chosen to be 2.13 in the pristine system, which corresponds to the optimal electron doping regime. For the impurity scattering, we fix the impurity scattering strength $W = -20$ and $\delta t = -0.2$.

This value of W is reasonable given by the Zn core level located ~ 8 eV below the Fermi level and is very close to the strong scattering (unitary) limit. Note we have checked several values of impurity scattering strength W. The results are insensitive to the precise value for $W < -8$. This might also be relevant to the impurity effect from Co and Ni substitution in LaFeAsO [153]. Specifically, for $W = -0.5$ the superconducting transition temperature is hardly affected by impurities up to $n_{imp} = 25.5\%$ [122–124].

5.3 Single impurity effects

Before we proceed with the complex disorder configuration, the single impurity effect on superconducting phase is studied. In the absence of impurities, our two-orbital model naturally captures the relation between SDW and SC phases and recovers the whole phase diagram with doping evolution. Henceforth, we shall restrict our calculations within this set of interaction parameters. With a single impurity in the unitary limit, we find that impurity scattering induces strong charge inhomogeneity and significantly suppresses the superconducting order parameter around the impurity site as illustrated in Fig. 5.1. In particular, we revisit the effects of a single Zn impurity on superconductivity in $Ba(Fe_{1-x-y}Co_yZn_x)_2As_2$ with $y > 0.1$, where there is no SDW. Note that localization of electrons on the impurity site is taken into account through the modified hopping coefficients of surrounding Fe atoms as presented in Eq. (5.5).

To gain deeper physical insights into scattering effects around a single impurity, we consider the 2D spatial cross-correlation functions of the superconducting order parameter and charge density defined by

$$C_X(\mathbf{i}) = \frac{\sum_{\mathbf{j}}[(X(\mathbf{i}+\mathbf{j}) - \langle X\rangle)(X(\mathbf{j}) - \langle X\rangle)]}{\sum_{\mathbf{j}}[X(\mathbf{j}) - \langle X\rangle]^2} \tag{5.8}$$

where $X = n$ and $|\Delta|$, and the mean $\langle X\rangle = (1/N)\sum_{\mathbf{j}} X(\mathbf{j})$ with N the number of lattice sites. The cross-correlation function is normalized to give $-1 \leq C_X \leq 1$. The results for the 2D cross-correlation functions are plotted in Fig. 5.1(c) through 5.1(e), where the fourfold symmetry and rapid screening over a few lattice sites becomes obvious. A quantitative analysis is possible when plotting C_X as a function of distance from the impurity site. In Fig. 5.1(e) we define a typical spatial correlation length ξ_X by measuring the impurity-induced fluctuations of X as the distance where C_X drops from unity to $1/e$. It is straightforward to read off from Fig. 5.1(e) that the additional local charge on Zn is well-screened within a lattice distance, $\xi_n \sim 1$. Indeed, it is over screened, resulting in Friedel-type oscillations, which are clearly visible in the correlation function. Such a short screening length is mainly due to the strong local Coulomb repulsion U, which acts on the charge sector. In contrast, the superconducting correlation function has a more profound oscillating tail with a short coherence length $\xi_\Delta \sim 2$. Based on these quite

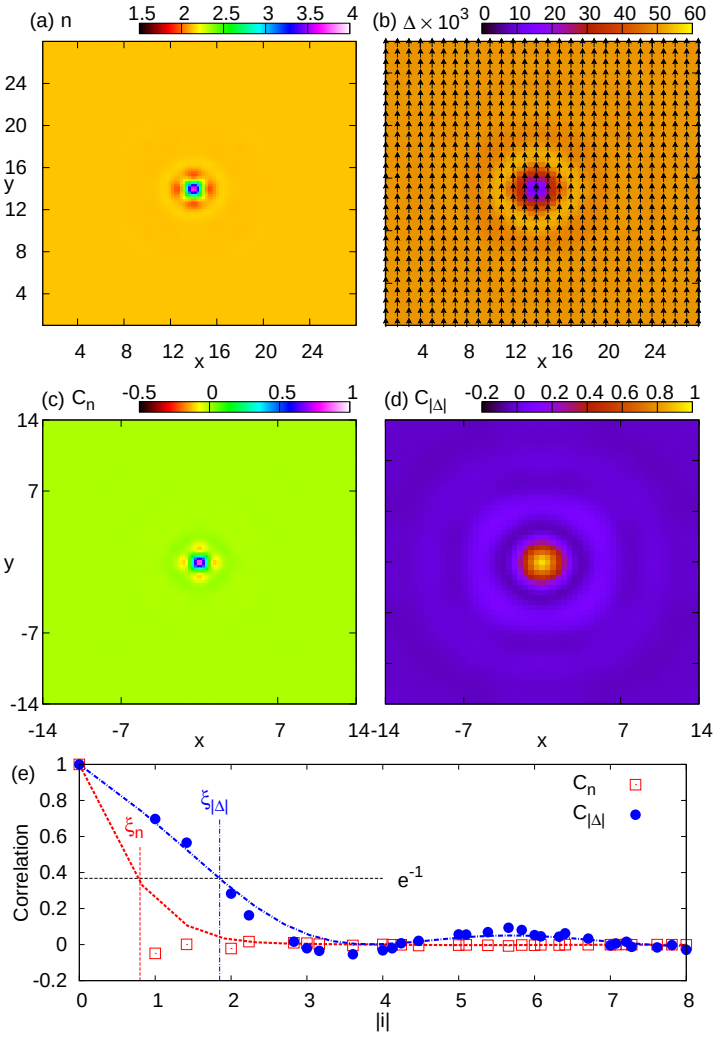

FIGURE 5.1: (Color online) Single impurity effects at zero temperature. The intensity plots of the local charge density (a) and superconducting order parameters (b). The arrows represent the argument of the complex superconducting order. The 2D cross-correlation functions of charge (c) and modulus of order parameter (d). For quantitative analysis the same correlation functions vs. distance $|\mathbf{i}|$ in (e).

short correlation lengths, we expect that the Zn-doped Ba-112 iron-based superconductor will be a good candidate for the Swiss-cheese model [165], where the holes of the Swiss-cheese correspond to the holes punched into the superconducting texture by the Zn impurity, while the effect on the bulk value of the superconducting order parameter is almost negligible after a few lattice sites away from the defect. Hence we anticipate that the $s_{\pm}$-pairing gap is easily destabilized by strong impurity scattering similar to the high-T_c cuprate [165], Sr_2RuO_4 [166], UPt_3 [167], and $PuCoGa_5$ superconductors [168]. Indeed, this result is in agreement with available experimental observations in $Ba(Fe_{1-x-y}Zn_xCo_y)_2As_2$, which has a relatively low Neel temperature $T_N \sim 135$ K and no trace of superconductivity for $y = 0$ and $x = 0.08, 0.25$ [154, 155]. On the other hand, when Co doping induces superconductivity, doping by several percent of Zn

rapidly suppresses it.

5.4 Disorder effects in the superconducting order parameter

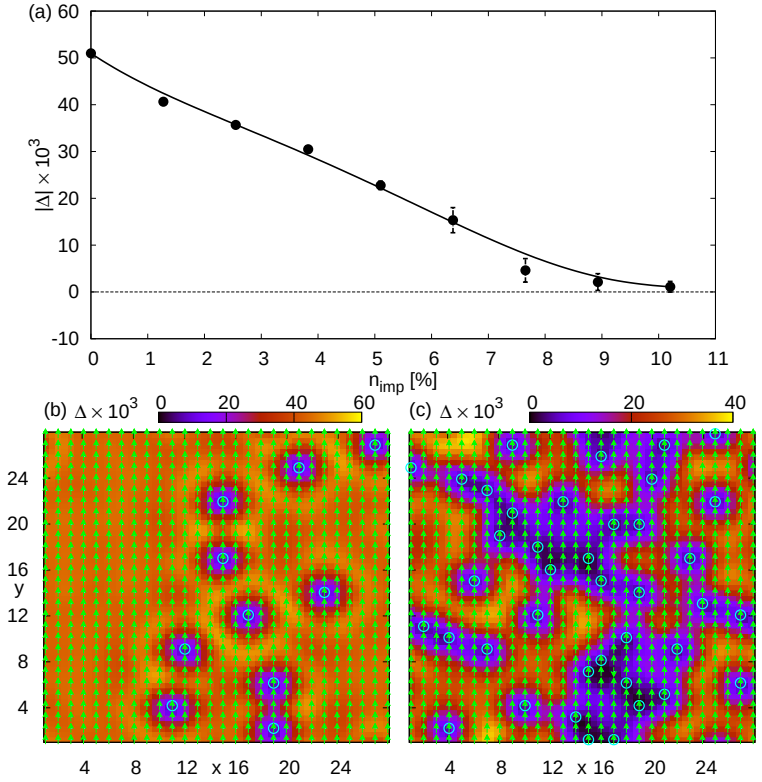

FIGURE 5.2: (Color online) Disorder effects at zero temperature. (a) The averaged superconducting order parameter $\langle\Delta\rangle = |\Delta|e^{i\phi}$ as a funtion of n_{imp}. The data is averaged over 5 disorder configurations. The error bars on the data points represents the statistical deviation. The solid line is fitted to guide the eye. Intensity plot of local superconducting order parameters for a typical impurity configuration with concentration $n_{\text{imp}} = 1.28\%$ (b) and $n_{\text{imp}} = 5.10\%$ (c). The arrows and open green circles represent the argument of complex superconducting order parameter and the impurity position respectively.

We next turn to the question of how superconductivity is affected by increasing the impurity concentration. For this purpose, the evolution of the disorder-configuration-averaged superconducting order parameter $\langle\Delta\rangle$ (at zero temperature) as a function of the impurity concentration n_{imp} is considered.

As for the case of the single impurity study, we focus on the compound

$$\text{Ba}(\text{Fe}_{1-x-y}\text{Zn}_x\text{Co}_y)_2\text{As}_2, \text{ with } y > 0.1 \tag{5.9}$$

when the SDW phase is suppressed. Again we are primarily interested in the local suppression of the superconductivity due to Zn substitution and the combined effects of charge localization and strong impurity scattering. For that purpose we make the following simplifications: (1) doping with Co adds mainly charge to the itinerant electrons that is captured by a shift of the chemical potential, and (2) scattering is in the weak limit compared to Zn. Hence, the local scattering effect of Co impurities is neglected. The results of the suppression of the lattice-averaged order parameter are plotted in Fig. 5.2(a). We find that the averaged modulus of the order parameter $\langle|\Delta|\rangle$ decays nearly linearly with increasing impurity concentration and eventually vanishes at a critical concentration of $n_{\rm imp} \approx 10 - 11\%$. Considering the superconducting transition temperature $T_{\rm c}$ is usually over estimated at the mean-field level (more on this later in Sec. 5.5), our results are in good agreement with recent measurements in $Ba(Fe_{1-x-y}Zn_xCo_y)_2As_2$ [150].

To provide an intuitive picture of disorder effects in highly disordered superconductors with increasing impurity concentration, we present a study of the evolution of the local superconducting order parameter for two particular realizations of disorder configurations. The spatially resolved order parameter $\Delta_{\mathbf{i}}$ is shown in colormaps in Figs. 5.2(b) and (c) for $n_{\rm imp} = 1.28\%$ and 5.10%, respectively. The images reveal that the order parameter is locally suppressed at the impurity sites, and the impurities behave individually when the impurity concentration is small as shown in Fig. 5.2(b). Of great interest is that the interference of the local order parameter at each impurity site develops gradually with increasing impurity concentration $n_{\rm imp}$, as one can clearly observe from Fig. 5.2(c), where islands form. The crude estimation on the threshold length of interference is given by ξ_Δ as illustrated in the previous Fig. 5.1(e). Also a considerable portion of sites has vanishing order parameter amplitude in the highly disordered limit. These correlated sites form islands and break the system into several superconducting puddles as illustrated in Fig. 5.2(c). Consequently, the local order parameter becomes highly inhomogeneous in Fig. 5.2(a). We propose, as in the case of high-temperature cuprate superconductors [144], that the novel electronic inhomogeneity should also be detected by measuring the local density of states using the atomic resolution scanning tunneling microscopy.

5.5 Total density of states and superfluid density

To gain further insight into the disorder effects in the unitary limit of highly disordered superconductors, we calculate several observables such as the total density of states (DOS), the superfluid density, and the magnetic penetration depth λ. The site-averaged

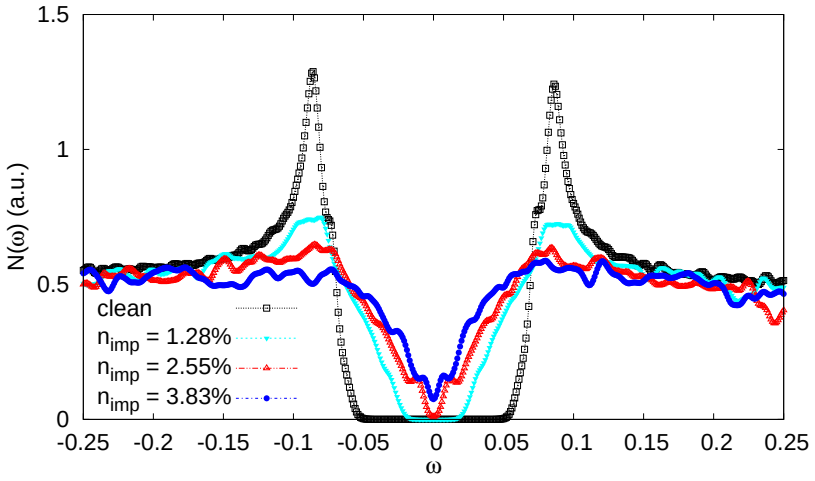

FIGURE 5.3: (Color online) Total density of states for various sets of impurity concentrations $n_{\rm imp} = 1.28, 2.55, 3.83\%$ at very low temperature $T = 0.002 \ll T_c$.

DOS at finite temperature is defined by

$$N(\omega) = -\frac{1}{N}\sum_{\mathbf{i}\alpha n}[|u^n_{\mathbf{i}\alpha}|^2 f'(\omega - E_n) + |v^n_{\mathbf{i}\alpha}|^2 f'(\omega + E_n)], \tag{5.10}$$

where $f'(E)$ is the derivative of the Fermi-Dirac distribution function with respect to the Fermi energy. For better visualization in Fig. 5.3, the DOS is calculated at finite temperature $T = 0.002 \ll T_c$. Note that in the pristine system two BCS coherence peaks are exhibited at the energies $\omega = \pm 0.1$, which corresponds to the single particle excitation gap. With increasing impurity concentration, the coherence peaks are gradually suppressed. Eventually above $n_{\rm imp} = 3.83\%$, the DOS is filled in and gapless superconductivity emerges.

In experiments, the magnitude of the superconducting transition temperature T_c is usually less sensitive to defects since it is related to the spatial average of the order parameter, which is a local correlation function. On the other side, the magnitude of the penetration depth λ measures the stiffness of the superconducting phase coherence in the superconductor, which is a nonlocal response function. Therefore, this quantity can provide deep insight into the nature of the superconducting pairing symmetry through its temperature dependence and residual value because these are extremely sensitive to defects. So far, measurements of the magnetic penetration depth in Fe-SCs have given controversial results. For example, in 122-type iron pnictides, the superfluid density exhibits an exponential temperature behavior in the cleanest hole-doped compounds, $Ba_{1-x}K_xFe_2As_2$[169], while a power-law behavior is seen in $Ba(Fe_{1-x}Co_x)_2As_2$[130, 170–175]. Very recently, one research studied the temperature dependence of the superfluid density of clean 122-type iron pnictides at various electron-doping levels and found that the low-temperature power-law dependence of the deviation $\Delta\lambda(T) = \lambda(T) - \lambda(0)$ varies

with an exponent greater than 3 [176].

In our multiorbital lattice BdG calculations, we follow the standard linear response approach of Refs. [177] and [178] to investigate disorder effects on the superfluid density. In the presence of a weak vector potential $\mathcal{A}_\eta(\mathbf{r},t)$ along the direction η, the hopping term is modified by the Peierls phase factors $e^{i\int \mathcal{A}_\eta(\mathbf{r},t)d\mathbf{r}}$ (We set $e=\hbar=c=1$). Hence, the change in the tight-binding Hamiltonian in the Meissner state is

$$\begin{aligned}\mathcal{H}_0' = &\sum_{\mathbf{i}\delta\alpha\beta\sigma} t^{\alpha\beta}_{\mathbf{i}\mathbf{i}+\delta} d^\dagger_{\mathbf{i}\alpha\sigma} d_{\mathbf{i}+\delta} \\ &\times[-i\mathcal{A}_\eta(\mathbf{i},t)\delta_\eta - \frac{1}{2}(\mathcal{A}_\eta(\mathbf{i},t)\delta_\eta)^2] + \mathcal{O}(\mathcal{A}_\eta^3)\end{aligned} \tag{5.11}$$

where δ_η projects δ onto the direction η in units of the lattice constant. The charge current density operator consists of the usual paramagnetic and diamagnetic parts,

$$\hat{j}_\eta(\mathbf{i},t) = -\frac{\partial \mathcal{H}_0'}{\partial \mathcal{A}_\eta(\mathbf{i},t)} = \hat{j}^P_\eta(\mathbf{i},t) + \hat{j}^D_\eta(\mathbf{i},t), \tag{5.12}$$

with

$$\{\hat{j}^P_\eta(\mathbf{i},t), \hat{j}^D_\eta(\mathbf{i},t)\} = \sum_{\delta\alpha\beta\sigma} t^{\alpha\beta}_{\mathbf{i}\mathbf{i}+\delta} d^\dagger_{\mathbf{i}\delta\sigma} d_{\mathbf{i}+\delta\beta\sigma}\delta_\eta\{i, \mathcal{A}_\eta\delta_\eta\}. \tag{5.13}$$

In the interaction representation, the kernel function K of the charge current satisfies

$$\langle\hat{j}_\eta(\mathbf{i},t)\rangle = -\sum_{\mathbf{i}'}\int dt' K(\mathbf{i},\mathbf{i}',t-t')\mathcal{A}_\eta(\mathbf{i}',t') \tag{5.14}$$

to leading order in the vector potential $\mathcal{A}_\eta$, where, the static kernel at $\omega=0$ is expressed by

$$\begin{aligned}K(\mathbf{i},\mathbf{i}',\omega=0) = &-\sum_{nm}\Gamma^{nm}_{\mathbf{i}}\Gamma^{mn}_{\mathbf{i}'}\frac{f(E_m)-f(E_n)}{E_m-E_n} \\ -\sum_{\delta\alpha\beta n} &t^{\alpha\beta}_{\mathbf{i}\mathbf{i}+\delta}[u^{n*}_{\mathbf{i}\alpha}u^n_{\mathbf{i}+\delta\beta}f(E_n) + v^n_{\mathbf{i}\alpha}v^{n*}_{\mathbf{i}+\delta\beta}f(-E_n)]\delta_\eta^2\delta_{\mathbf{i},\mathbf{i}'}.\end{aligned} \tag{5.15}$$

Here, the auxiliary functions are $\Gamma^{nm}_{\mathbf{i}} = \sum_{\delta\alpha\beta} t^{\alpha\beta}_{\mathbf{i}\mathbf{i}+\delta}(u^{n*}_{\mathbf{i}\alpha}u^m_{\mathbf{i}+\delta\beta} - v^m_{\mathbf{i}\alpha}v^{n*}_{\mathbf{i}+\delta\beta})\delta_\eta$. Fourier transform with respect to the individual coordinates $\mathbf{i}$ and $\mathbf{i}'$ then defines the spatially averaged kernel function $\bar{K}(\mathbf{q},\omega=0) = (1/N)\sum_{\mathbf{i},\mathbf{i}'} e^{-i\mathbf{q}\cdot(\mathbf{i}-\mathbf{i}')}K(\mathbf{i},\mathbf{i}',\omega=0)$, which gives the bulk superfluid density $\bar{\rho}_s = \bar{K}(\mathbf{q}\to 0,\omega=0)$. We also define the local superfluid density as

$$\rho_s(\mathbf{i}) = K(\mathbf{i},\mathbf{i};\omega=0) \tag{5.16}$$

to investigate the local suppression of the superfluid density. As shown in Fig. 5.4(a), we find that the local superfluid density is dramatically suppressed at impurity sites.

As illustrated in Fig. 5.4(b), the bulk superfluid density $\bar{\rho}_s$ decreases drastically to zero, much faster than T_c, as expected with increasing impurity concentration $n_{\rm imp}$ in the Swiss-cheese scenario for a short coherence superconductor. This different rate of suppression is further corroborated by the Uemura plot as shown in Fig. 5.4(c), suggesting the break-down of the AG theory. We note that the loss of phase coherence is related to the vanishingly small superfluid density near the critical concentration of impurities [179], implying the importance of spatial disorder induced fluctuations [180, 181]. As manifested in Fig. 5.2(c), a Bose system consisting of localized Cooper pairs is gradually formed in the highly disordered limit due to the loss of phase coherence between the superconducting puddles. Unfortunately, the physically interesting region, where the superfluid density is vanishing small, is not captured within the BdG framework due to the neglect of phase fluctuations. In the present mean-field theory the phases of the order parameter at different sites are completely aligned with the ground state as shown in Fig. 5.2(b) and (c). For details on the consequences of quantum phase fluctuations on the order parameter in the inhomogeneous BdG state using a quantum XY model see Ref. [182].

Finally, we also calculated the temperature dependence of the deviation $\Delta\lambda(T)$ of the magnetic penetration depth in the presence of disorder, which is related to the bulk superfluid density $\lambda^2 \propto 1/\bar{\rho}_s$. In the clean limit, $\Delta\lambda(T)$ is expected to vary exponentially at low temperatures due to a gapped DOS, as shown in Fig. 5.5. The exponential decay is consistent with a fully gapped pairing state. At the impurity concentration $n_{\rm imp} = 3.83\%$, the temperature dependence of $\Delta\lambda(T)$ shows a T^2 power law. Hence we expect that for intermediate impurity concentrations the temperature behavior will resemble that of a power law with exponent greater than two. Interestingly, the T^2 variation of $\Delta\lambda(T)$ is observed experimentally in $Ba_{1-x}K_xFe_2As_2$ [169, 183], and $Ca_{0.5}Na_{0.5}Fe_2As_2$ single crystals [184], possibly due to the doping-induced disorder. Our calculation showcases that the temperature dependence of the penetration depth in an $s_\pm$-wave pairing superconductor can be very sensitive to the impurity scattering. Depending on the impurity concentration, it may enable us to explain various power-law behaviors in Fe-SCs [130, 170–175].

5.6 Summary

To summarize, by solving the lattice BdG equations self-consistently, we have studied disorder effects on superconducting and transport properties of disordered superconductors with $s_\pm$ pairing symmetry. In the unitary limit, the impurity scattering strength is so large that the potential scattering term cannot be treated as a perturbation in the framework of pair breaking by Abrikosov and Gorkov. The detailed numerical calculations demonstrate that a single nonmagnetic impurity can depress superconductivity

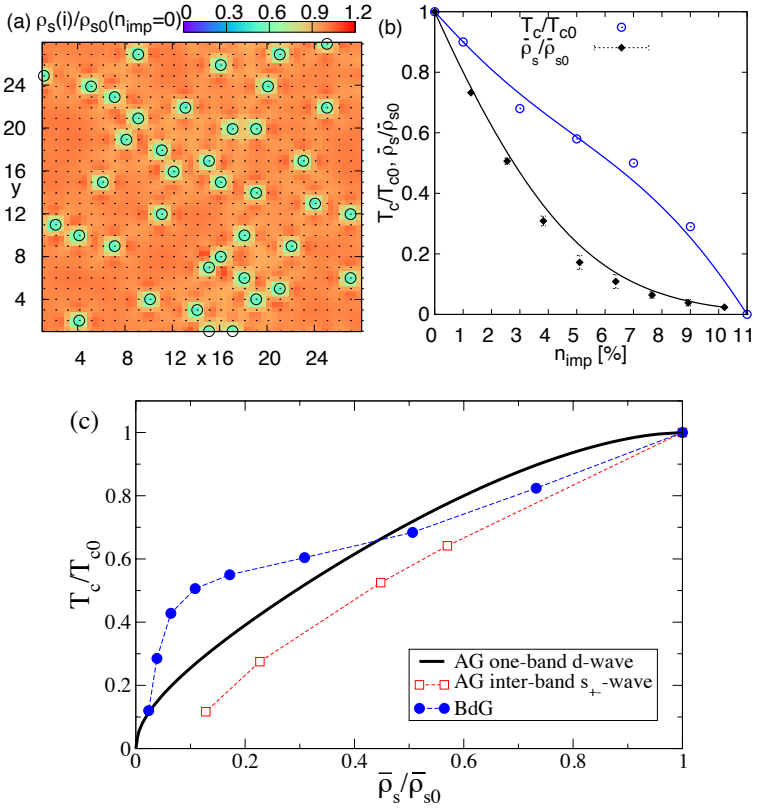

FIGURE 5.4: (Color online) (a) The normalized intensity (unitless) of local superfluid density $\rho_s(\mathbf{i})$ with $n_{\rm imp} = 3.83\%$ at zero temperature. The open black circles indicate the impurity locations. (b) The zero-temperature bulk superfluid density $\bar{\rho}_s$ and superconducting transition temperature T_c as a function of impurity concentration $n_{\rm imp}$. The data is averaged over five randomly distributed impurity configurations. (c) The Uemura plot of the superfluid density in short-coherence superconductors. The variables T_{c0} and $\bar{\rho}_{s0}$ are obtained from a pristine system. For comparison, we also plot results of the one-band AG calculations for d-wave pairing symmetry [159] and the two-band AG calculations for the $s_{\pm}$-wave symmetry [185].

significantly at the local scale. With increasing impurity concentration the impurity scattering potential induces a spatial redistribution of the amplitudes of local Cooper pairs in the form of superconducting puddles, giving rise to significant spatially electronic inhomogeneity. Calculations of the local density of states, the superfluid density, as well as the magnetic penetration depth further reinforce this picture, demonstrating again that the superconducting phase is not stable against strong impurity scattering as expected in the Swiss cheese scenario.

Our results shed new light on the understanding of recent experiments in Co- and Zn-substituted $BaFe_2As_2$ samples [150]. In these samples the superconductivity is completely suppressed when the concentration of Zn impurities $n_{\rm imp}$ is above 8%. The available angle-resolved photoemission spectrocopy experiments indicate that the substitution by Zn atoms not only provides additional electrons into the Fe lattice, but also creates strong local scattering potentials because the Zn-3d orbitals are well-below the

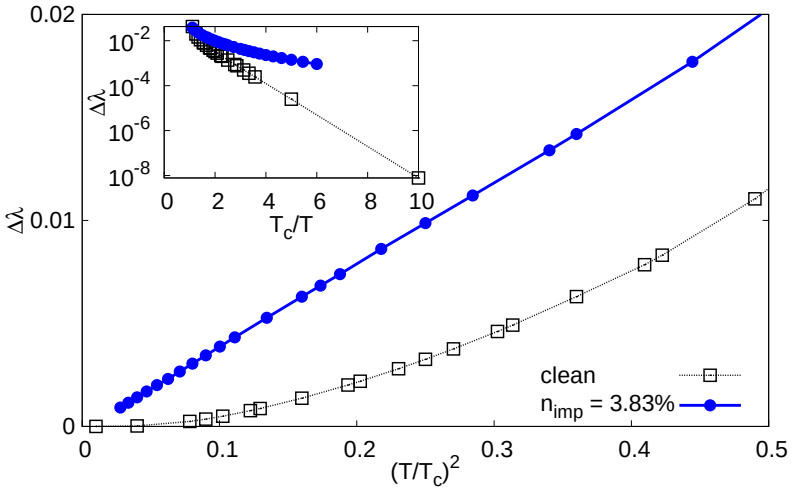

FIGURE 5.5: (Color online) Temperature dependence of the deviation of the magnetic penetration depth $\Delta\lambda$ in the clean limit (open black square) and for a dirty system with impurity concentration $n_{\mathrm{imp}} = 3.83\%$ (solid blue circle). The data is averaged over five randomly selected disorder configurations. Inset: Replotted data to emphasize the exponential low-temperature behavior of the clean system.

Fermi level [154, 155]. All these observations are consistent with our numerical results. Furthermore, our calculations show that superconductivity is hardly affected by weak intraorbital scattering with scattering potential $W = -0.5$ (corresponding to Co and Ni) or by interorbital scattering in the unitary limit. We anticipate that the emergent electronic inhomogeneity in the strong scattering limit, due to local screening effects, will be probed in future scanning tunneling microscope and scanning Meissner force microscope experiments [186].

Chapter 6

Emergent topological orbital phases in tetragonal t_{2g} systems

6.1 Introduction

Previous **chapters** (**2.** to **5.**) were all related with magnetic and superconducting orders, however, devated from these orders, I found that it is possible to have topological orders in the iron-based t_{2g} system based on the new model [15]. In this chapter, I will give more insights with the topological index and symmetry analysis based on the new model in **chapter 3.**.

The class of topological insulators (TIs) is characterized by topological properties in the electronic wave function with the emergence of protected edge or surface states. In fact, the integer quantum Hall insulator is the first known TI, which was characterized by the topological Chern number [187] under the condition of broken time-reversal (TR) symmetry due to external magnetic fields. Haldane showed that such a Chern insulator can be realized on a honeycomb lattice with opposite spontaneous internal magnetic fields between two different sub-lattices, even in the absence of external magnetic fields [188]. By promoting Haldane's model to the class of Hamiltonians with spin degrees of freedom that respect the TR symmetry in the presence of strong spin-orbit coupling, the quantum-spin Hall insulator, characterized by a nontrivial Z_2 topological invariant, was proposed [189, 190]. Later this idea was generalized to Z_2 TIs in three dimensions (3D). Some of the non-trivial topological properties that usually accompany TIs are the odd number of Dirac cones of these edge or surface states in the Brillouin zone. Experimentally, the quantum spin Hall insulator was realized in the quasi-two-dimensional sub-bands of the HgTe/CdTe quantum well structures [191], following the theoretical proposal by Bernevig and collaborators [192] based on strong spin-orbit coupling (SOC) due to the heavy tellurium atom. In addition, the Z_2 TI in 3D was realized shortly thereafter in the doped $Bi_{1-x}Sb_x$ alloy [193] and other bismuth-based and

tellurium-based compounds [194, 195].

The quest for topological phases in multi-orbital systems is ongoing in cold-atom gases and photonic crystals [196, 197]. However, there are very few studies on multi-orbital systems in real materials beyond those with the honeycomb lattice. Recently, the topological Kondo insulator in rare-earth materials due to the hybridization of an itinerant band with a localized band with different inversion parity, attracts much attention [198]. Here we propose a new possibility for realizing non-trivial topological phases through Coulomb interactions in tetragonal systems with the t_{2g} symmetry caused by crystal-field splitting. The modest Coulomb interaction prevails in compounds with transition metal elements, even though the hybridization of two degenerate bands is identical in the parity under spatial inversion symmetries. We show that non-trivial topological phases can be induced by generating spontaneous orbital currents in an effective, low-energy two-orbital (d_{xz} and d_{yz} orbitals) model, which leads to the anomalous-orbital-hall (AOH) effect. The nature of these orbital currents is different from the loop or current flux phases that were employed to describe the pseudo-gap phase in the copper-oxide superconductors [199–203], which have different orbital degrees of freedom and crystal symmetries. Indeed, the AOH effect offers a new realization of the topological Mott insulator [204–207]. In that respect our model may help in the search for novel topological phases in transition-metal oxides and other compounds with active d_{xz} and d_{yz} orbital degrees of freedom. However, there are two possible mean-field ground state configurations of these orbitals, which respect the C_{4v} symmetry of one transition-metal atom per unit cell (For details see the Appendix D.). The first configuration of type I [196, 197, 208], which is frequently discussed in literatures, is the $d_{xz/yz}$ orbital locking of the nearest neighbor (NN) chemical bond direction. The second configuration of type II is the $d_{xz/yz}$ orbital locking of the next-nearest neighbor (NNN) chemical bond direction. Type II configuration proposed in this work is responsible for the generation of spontaneous orbital currents in mean-field ground states, which leads to topologically nontrivial phases.

For transition metals with crystal-field splitting caused by a tetragonal lattice distortion, the d_{xz} and d_{yz} are the only two relevant orbital degrees of freedom of the t_{2g} orbital manifold at low energy. We begin our study with an effective two-orbital model [15, 209, 210] and calculate the inter-orbital Coulomb interaction with mean-field theories. Based on these mean-field solutions, the inter-orbital Coulomb interaction generates spontaneous orbital current flux. This new orbital order gap out the Dirac dispersion in the bulk bands and generates two edge bands with the linear dispersion following one-dimensional version of two Dirac cones when spinless (or spin polarized) fermions are considered. We further extend the model to the Hamiltonian with spin degrees of freedom and discuss two uniquely distinguishable phases: Phase **(I)**: The orbital currents are parallel to the $\uparrow$ / $\downarrow$ spin with doubled Chern number, $\mathcal{C} = \pm 4$. Phase **(II)**:

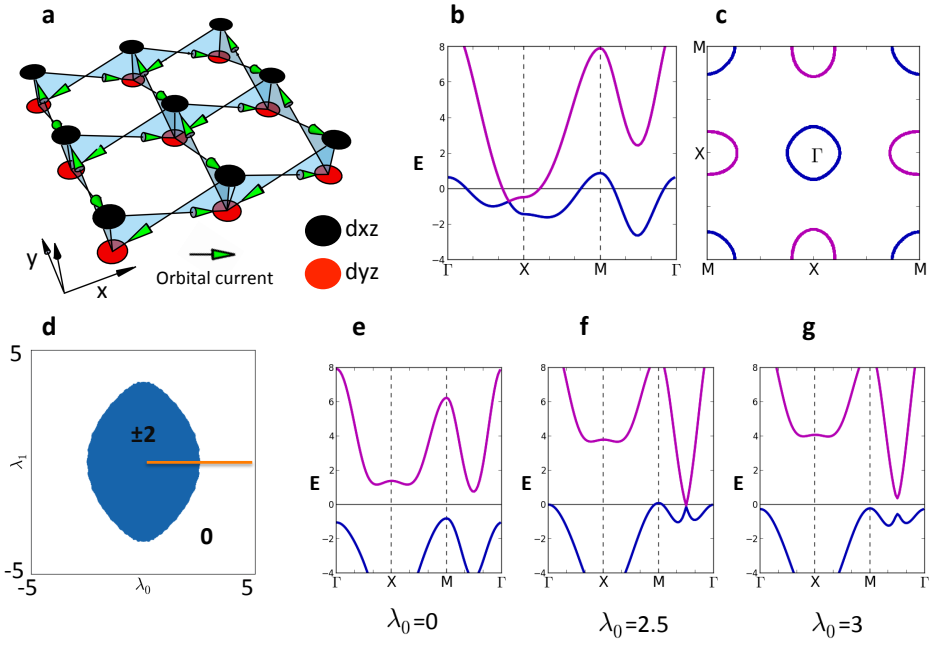

FIGURE 6.1: (color online) (a) The schematics of the orbital current order (λ_{AOH}). The coordinates x and y are in the 1-Fe per unit cell. (b) and (c) The electronic band structure and Fermi surfaces at half-filling without interaction terms. (d) The calculated phase diagram based on the Chern number $\mathcal{C}$ with $\lambda_{AOH} = 1$ and $-5 < \lambda_{0,1} < 5$. (e),(f) and (g) The evolution of the corresponding band structure from TI to metal to trivial band-gap insulator for different values of λ_0 at $\lambda_1 = 0$ along the orange line cut in (d). Note that both the λ_0 and λ_1 term break the C_{4v} symmetry.

The orbital currents are anti-parallel to the $\uparrow$ / $\downarrow$ spin with vanishing Chern number, $\mathcal{C} = 0$. We see that Phase **(I)** and the spinless Hamiltonian are a realization of the Chern insulator, while Phase **(II)** leads to the Z_2 classification of the TI. Without the introduction of additional terms, our mean-field calculation shows the states of Phases **(I)** and **(II)** are equal in energy. Of course this degeneracy can be lifted, once the on-site intra-orbital spin-exchange interaction is considered, then Phase **(II)** can be considered as the better mean-field ground state at low temperature.

6.2 The model Hamiltonian

Let us introduce the model Hamiltonian for spinless fermions to facilitate our discussions. The spinless Hamiltonian $\hat{H}$ together with two additional interaction terms, λ_0 and λ_1,

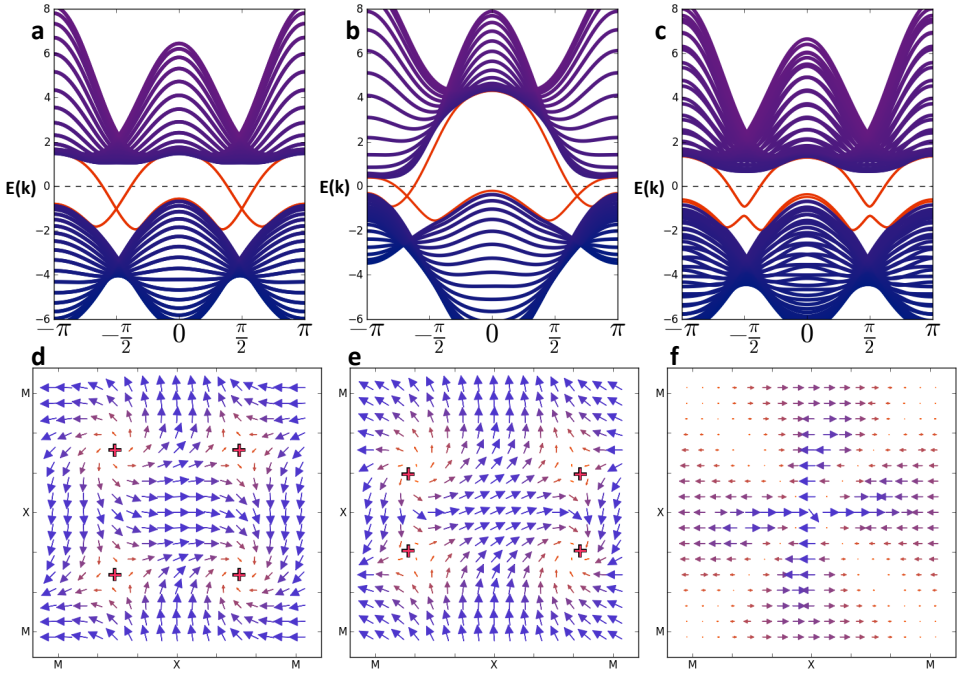

FIGURE 6.2: (color online) (a) - (c) The electronic dispersion of the edge states (red lines) for different interaction parameters, but fixed $\lambda_{AOH} = 1$. (a) $\lambda_0 = \lambda_1 = \lambda_R = 0$; (b) $\lambda_1 = 2$; (c) $\lambda_R = 0.03$. Note that any finite λ_R splits the Dirac cones. (d) - (f) The corresponding vector plot of the complex Pfaffian function $\mathcal{P}(\mathbf{k})$. The bi-color code represents small (orange) to large (blue) modulus $|\mathcal{P}(\mathbf{k})|$. The red crosses mark the positions of the vortex cores, i.e., $\mathcal{P}(\mathbf{k}) = 0$.

is given by

$$\begin{aligned}\hat{H} = &\sum_{IJ,\alpha\beta} t_{IJ}^{\alpha\beta}\, c_{I\alpha}^{\dagger}\, c_{J\beta} + i\,\lambda_{AOH}^{a} \sum_{IJ,\alpha\neq\beta} \epsilon_{IJ}^{\alpha\beta}\; c_{I\alpha}^{\dagger} c_{J\beta} \\ &+\lambda_0 \sum_{I\alpha} (-1)^{\alpha} c_{I\alpha}^{\dagger} c_{J\alpha} + i\,\lambda_1 \sum_{I,\alpha\neq\beta} (-1)^{\alpha}\, c_{I\alpha}^{\dagger} c_{I\beta} \\ &-\sum_{I\alpha} \mu\, c_{I\alpha}^{\dagger} c_{I\alpha},\end{aligned} \tag{6.1}$$

where I, J are site indices, α, β are orbital indices. $\epsilon_{IJ}^{\alpha\beta}$ indicate the direction of each inter-orbital current term shown in Fig. 6.1(a) and is given in Table. I of the Appendix D. The first term with hopping parameter $t_{IJ}^{\alpha\beta}$ is the kinetic term of spinless fermions in the lattice and the last term, μ, is the chemical potential. The AOH effect is described by the complex hopping term between different orbitals for sites I and J with the coupling constant λ_{AOH}^{a} determined by spontaneously generated current through the inter-orbital Coulomb interaction, the index a of λ_{AOH}^{a} is preserved for future study when spin degree of freedom is incoporated. The on-site orbital energy difference λ_0 is responsible for the on-site orbital charge polarization, whereas the on-site complex hopping with the coupling constant λ_1 describes the on-site inter-orbital coherence.

In the case of translational invariant crystal symmetry, we can Fourier transform the spinless Hamiltonian to $\mathbf{k}$-space and write it in 2×2 matrix form, $\hat{H}(\mathbf{k})$, with basis functions $\psi_{\mathbf{k}} = (c_{\mathbf{k}\alpha}, c_{\mathbf{k}\beta})^T$. We derive the expression $\hat{H}(\mathbf{k}) = E_0(\mathbf{k}) + \vec{B}(\mathbf{k}) \cdot \vec{\tau}$, where $\vec{B} = (X, Y, Z)$ and $\vec{\tau} = (\tau_x, \tau_y, \tau_z)$ are the Pauli matrices. The detailed expressions for the matrices X, Y and Z are given in the Appendix D. The 2×2 matrix $\hat{H}(\mathbf{k})$ can be easily diagonalized. The analytic expression for the eigenvalues is $E_\pm(\mathbf{k}) = E_0(\mathbf{k}) \pm B(\mathbf{k})$, where $B = |\vec{B}|$. The corresponding eigenvectors are

$$\begin{aligned} |+, \mathbf{k}\rangle &= (Z + B, X + i\,Y)^T / \sqrt{2B^2 + 2ZB}, \\ |-, \mathbf{k}\rangle &= (-X + i\,Y, Z + B)^T / \sqrt{2B^2 + 2ZB}. \end{aligned} \tag{6.2}$$

We find that Dirac cones exist in the dispersion of the bulk material when all the interaction-induced terms are turned off ($\lambda^a_{AOH} = \lambda_0 = \lambda_1 = 0$). Their locations are determined by $B(\mathbf{k}) = 0$. They are protected by the C_{4v} and TR symmetries of spinless fermions with double degeneracy at each Dirac point.

6.3 Topological Phases

In Figs. 6.1(b) and 6.1(c) we show the dispersion of the electronic band structure of the bulk material at half filling when $\lambda^a_{AOH} = \lambda_0 = \lambda_1 = 0$. The Chern number $\mathcal{C}$ can be calculated directly through the Berry curvature of the Hamiltonian $\hat{H}(\mathbf{k})$, which is defined as $\mathcal{C}\,(\lambda^a_{AOH}; \lambda_0; \lambda_1; n) = \frac{1}{2\pi}\int_{k\in BZ} dk\, \Omega^n(k)$, with integer band index n. The first observation is that $\mathcal{C}\,(\lambda^a_{AOH}; 0; 0; n) = \pm 2$ for any real λ^a_{AOH}. The second observation is that the sign of $\mathcal{C}$ depends on the sign of λ^a_{AOH}, which determines the class of the Chern insulator, $\text{sign}(\mathcal{C}) = \text{sign}(\lambda^a_{AOH} \times (-1)^n)$. Since the topological phase with $\mathcal{C} = \pm 2$ is robust against weak perturbations by symmetry breaking terms, we show its stability region in the λ_0-λ_1 phase diagram in Fig. 6.1(d) for $\lambda^a_{AOH} = 1$. Note that the TI phase is interaction induced and therefore vanishes for $\lambda^a_{AOH} \to 0$. Following the orange line cut in the phase diagram, we see the evolution of the bulk band-gap as it closes and reopens with varying λ_0, see Figs. 6.1(e) to 6.1(g). This leads to a sequence of phase transitions from a topological Chern insulator to a metal (around $\lambda_0 = 2.5$) and on to a trivial band-gap insulator.

For practical purposes in real materials, we need to consider electrons as fermions with spin degrees of freedom. Therefore, we promote the spinless two-band orbital model to the spinful model with spins as $\hat{H}_s = \hat{H}_\uparrow[\epsilon_\uparrow] + \hat{H}_\downarrow[\epsilon_\downarrow]$, where the sign of the orbital current direction is considered $\lambda^a_{AOH} = \epsilon_a |\lambda^a_{AOH}|$, spin index $a \in [\uparrow, \downarrow]$. A detailed analysis of the Hamiltonian $\hat{H}^s$ reveals the following stable topological phases:

- Phase **(I)** $\epsilon_\uparrow = \epsilon_\downarrow$ with Chern number $\mathcal{C} = \pm 4$,
- Phase **(II)** $\epsilon_\uparrow = -\epsilon_\downarrow$ with Chern number $\mathcal{C} = 0$.

For Phase **I**, we find that the Chern number ± 4 is twice of the spinless case due to the twofold degeneracy of spins. Here it has the same orbital current direction as discussed before. For Phase **II**, we find that the Chern number classification scheme is insufficient to capture the topological nontrivial insulator phase. To see whether Phase **II** is a TI, we plot the edge states of the slab geometry in Fig. 6.2(a). The calculated edge states along the (1,0,0) direction show two Dirac cones at $k_x{=}\pm\frac{\pi}{2}$. Furthermore, we show in Fig. 6.2(b) that these edge states are robust against the perturbation $\lambda_1 = 2$, although the position of the Dirac cones is shifted away from $k_x = \pm\frac{\pi}{2}$. One may tend to claim that Phase **II** is a conventional Z_2 quantum spin Hall insulator since the time reversal symmetry is respected by the mean-field Hamiltonian for Phase **II** with zero Chern number. However, it cannot be reconciled with the fact that the number of pairs of degenerate edges states are even instead of odd. We claim that Phase **II** is a topological mirror insulator protected by mirror symmetry as indicated by the even mirror Chern number $\mathcal{C}_M$, which is equivalent to the spin Chern number for Phase **II**, given by $\mathcal{C}_M = (\mathcal{C}_\uparrow - \mathcal{C}_\downarrow)/2 = [2-(-2)]/2 = 2$ as opposed to the Z_2 quantum spin Hall insulator in Kane and Mele lattice model with odd mirror Chern number $\mathcal{C}_M = 1$ (in the absence of spin-orbital couplings). In the following section, we propose a topological invariant for the topological mirror insulator realized in Phase **II**.

It is noticed that we only consider the imaginary part of the intra-orbital current order given by λ^a_{AOH} term induced by off-site Coulomb interaction. In general, we should include the real part. Since the real and spatial uniform term only causes the renormalization of hopping terms, it does not affect the band topologies of the phases(see **Appendix D.**). In addition, based on our current models, Phase **(I)** and Phase **(II)** are degenerate to our numerical accuracy if we only consider the off-site Coulomb interaction. However, if one include an additional on-site intra-orbital spin-exchange term, J, the degeneracy between Phase **(I)** and Phase **(II)** is lifted and Phase **(II)** has lower energy (see **Appendix D.**).

6.4 Mirror topological invariant

Based on symmetry of the mean-field Hamiltonian for Phase **II**, time reversal symmetry is still respected. However, the number of Kramers' pair at the edges are even instead of odd. This indicates that Phase **II** is not adiabatically connected to the Z_2 quantum spin Hall Insulator protected by time reversal symmetry.

We notice that the spinful Hamiltonian $\hat{H}_s$ for Phase **II** satisfy the mirror symmetry $\mathbf{M}\hat{H}_s(k_x,k_y)\mathbf{M}^{-1} = \hat{H}_s(-k_x,k_y) = \hat{H}_s(k_x,-k_y)$ in which the mirror operator is given by $\mathbf{M} = \mathbf{PT} = (\tau_x\mathbf{K})\otimes(-i\sigma_y\mathbf{K})$ in the basis we use in the manuscript (see **Appendix D.** for detailed symmetry analysis). The operator $\mathbf{K}$ performs the complex conjugate operation identical to the TR operation for spinless fermions. The operator $\mathbf{P}$ swap

two orbitals and the operator, $-i\sigma_y$, is responsible for the spin flipping with the TR-operation, $\mathbf{T}$. Because of the mirror symmetry $\mathbf{M}$ in the mean-field Hamiltonian $\hat{H}_s$, we define two different space of the Bloch wavefunctions $|u_n(\mathbf{k})\rangle$ on the BZ, which differ by their properties under mirror symmetry: an even subspace for which the space spanned by $|u_n(\mathbf{k})\rangle$ is equivalent to $M|u_n(\mathbf{k})\rangle$ up to a phase vector, and an odd space, for which they are orthogonal.

A mirror Pfaffian invariant analogous to the Z_2 quantum spin Hall phase in Kane-Mele model [189, 190] can be used to capture the band topology in Z_2 quantum spin Hall insulator. In our case, the mirror Pfaffian invariant is constructed to capture the band topology of the topological mirror insulator we discuss as

$$\mathcal{P}(\mathbf{k}) = Pf\big[\langle u_m(\mathbf{k})|\mathbf{M}|u_n(\mathbf{k})\rangle\big], \tag{6.3}$$

where $|u_m(\mathbf{k})\rangle, |u_n(\mathbf{k})\rangle$ are two occupied orthogonal eigenstates of the Hamiltonian $\hat{H}_s(\mathbf{k})$. For the $\mathbf{k}$ points at the "even" space along the k_x and k_y axes, the commutation relation $\mathbf{M}\hat{H}_s(\mathbf{k})\mathbf{M}^{-1} = \hat{H}_s(\mathbf{k})$ holds. Therefore, the two eigenstates $|u_m(\mathbf{k})\rangle = \mathbf{M}|u_n(\mathbf{k})\rangle$ and $|u_m(\mathbf{k})\rangle$ are degenerate. As a results, the absolute value of the Pfaffian $\mathcal{P}(\mathbf{k}) = Pf\big[\langle u_m(\mathbf{k})|\mathbf{M}|u_n(\mathbf{k})\rangle\big]$ at the k_x axis and k_y axis is given by $|\mathcal{P}(\mathbf{k})| = 1$. For the $\mathbf{k}$ points at the "odd" space satisfying the anti-commutation relation $\mathbf{M}\hat{H}_s(\mathbf{k})\mathbf{M}^{-1} = -\hat{H}_s(\mathbf{k})$, $\mathbf{M}|u_i(\mathbf{k})\rangle$ turns into unoccupied eigenstate and is orthogonal to the eigenstate $|u_j(\mathbf{k})\rangle$ with vanishing Pfaffian $\mathcal{P}(\mathbf{k}) = 0$.

In Fig. 6.2(d), we show the Pfaffian in the Brillouin Zone (BZ) for the topological mirror insulator. There are four vortices well separated by the even space at k_x and k_y axis. Let us examine the effects on the Paffian $\mathcal{P}(\mathbf{k})$ when an infinitesimal mirror symmetry breaking interaction is adiabatically turned on. We introduce the on-site Rashba spin-orbit interaction $i\lambda_R \sum_{I\alpha\sigma}(-1)^{\alpha}(-1)^{\sigma}c^{\dagger}_{I\alpha\sigma}c_{I\alpha\bar{\sigma}}$. The corresponding Hamiltonian $\hat{h}_R(\mathbf{k}) = \lambda_R\,\tau_z \otimes \sigma_y$ in momentum space breaks the mirror symmetry ($[\hat{H}_s + \hat{h}_R(\mathbf{k}),\ M] \neq 0$). This will destroy the mirror topological phase even though the interaction $\hat{h}_R(\mathbf{k})$ is infinitesimal. As we expect, the four vortices disappear with the infinitesimal Rashba spin-orbit interaction as shown in Fig. 6.2(f). As far as the edge states are concerned, an infinitesimal λ_R will destroy the edge states and the gapless edge states are gapped in Fig. 6.2(c).

A different scenario occurs when a finite interaction is turned on without breaking the mirror symmetry. We consider the inter-orbital coherence interaction λ_1. In momentum space, the interaction is given by the expression $-i\lambda_1\tau_y$ which breaks the time reversal symmetry $\mathbf{T} = -i\sigma_y K$ but preserve the mirror symmetry $\mathbf{M}$. In this case, the Paffian is plotted in Fig. 6.2(e). Here the locations of the pair of vortices in the upper BZ half-plane are modified and move toward the pair in the lower half-plane compared to Fig. 6.2(d) as the strength of λ_1 increases. This trend continues until vortices disappear

at a critical strength $\lambda_{1c} \approx 2.5$, which corresponds to the region of the phase boundary in Fig. 6.1(d) for spinless fermions, before touching the even space of the Paffian, which cannot accommodate vortices. This observation is consistent with the corresponding degenerate states in edge states as displayed in Fig. 6.2(b). The locations of the degeneracies are the direct projection of the vortex positions in the BZ of Fig. 6.2(e) on the edges.

As described above, the Pfaffian $\mathcal{P}(\mathbf{k})$ is a good indicator to tell whether a system has a non-trivial band topology due to the mirror symmetry $\mathbf{M}$. We can define the mirror topological index by counting the number of vortex cores,

$$I = \frac{1}{2\pi i} \oint_{\partial \mathbf{S}_4} d\mathbf{k} \cdot \nabla_{\mathbf{k}} \log[\,\mathcal{P}(\mathbf{k})\,] \mod 2, \tag{6.4}$$

where $\partial \mathbf{S}_4$ is the boundary of one quarter of the BZ. From the symmetry analysis of phase **II** in the Appendix D., we know that the even subspace is sitting on $\mathbb{C}$. Note that $\mathbb{C}$ is not a single point, but rather paths which divide the BZ into four independent sections. Since the $\mathbf{M}$ operator connects (k_x, k_y) to $(\pm k_x, \mp k_y)$ for phase **II** with Hamiltonian $\hat{H}_s^{II}$ and the Hamiltonian has intrinsic symmetry, $\hat{H}_s^{II}(\mathbf{k}) = \hat{H}_s^{II}(-\mathbf{k})$, the minimal irreducible section becomes the quarter of the BZ. Hence, the odd/even number of vortices inside a quarter of the BZ determines the nontrivial/trivial topology of the bands.

6.5 Conclusions

In conclusion, we have demonstrated a new path to realize non-trivial topological phases by Coulomb interaction in compounds where t_{2g} orbitals are the low energy manifold. Specifically, we focus on the compounds with the ground state orbital orientation respecting C_{4v} symmetry with 45-degree intra-orbital orientation. Based on mean-field theories, we identify two topological insulating phases induced by Coulomb repulsive interaction. One phase is adiabatically connected to conventional quantum Hall insulator with even Chern number. In addition, we identify an emergent topological mirror insulator with mirror symmetry which is different from the Z_2 topological insulators proposed earlier [195, 211–214]. We propose a mirror topological invariant to capture the band topology of the phase by counting the vortex number of mirror Pfaffian in a quarter of BZ.

Finally, we suggest possible candidates for the emergent TCI phases in materials with crystal field split t_{2g} orbitals that are described by a simple two-orbital effective Hamiltonian, which should be considered as an effective theory for the paramagnetic phase even at finite temperature with normalized parameters.

When the system is a Chern insulator, the anomalous orbital Hall effect with finite magnetic moments will occur due to orbital currents, yet without spin order. Based on

this work, we suggest to look for TCIs in the iron-pnictide based nonmagnetic insulators with crystallographic 122 structure [82], where the Fermi surface is close to half-filling. Due to the edges states, the material candidate should show electric conductivity even at low temperature even though the bulk is insulating.

We suggest to focus on pnictides showing paramagnetic and bad metallic conductivity. Based on the experimental evidence, the Ni-based compound, $BaNi_2As_2$ with very low superconducting temperature ($T_c \approx 0.6$K), is likely such a candidate. It does not show spin-density wave state when the d electron filling is almost fully filled within our two-orbital model. By hole doping with K on the Ba site of $BaNi_2As_2$, the electron filling can be reduced to close to half-filled. With compressional stress applied normal to the NiAs layer, the lattice constant in the NiAs layer can be enlarged due to strain responses (see Supplementary Material in Section I). In this regime, a paramagnetic insulating state should be looked into. The $BaFe_2As_2$ at a temperature above Neel temperature is also a possible area to look for the TCI phase. Other members of the 122 family may also be suitable for detecting the TCI phase but systematic studies are needed to sort this out.

Similar to other TIs, when the topological edge states stacked along the layer growth direction to form the surface states, the surface states can be verified through scanning tunneling and angle-resolved photoemission spectroscopies. In addition, systematic measurements of the Hall conductivity can distinguish the proposed TCI (phase **II**) from the Chern insulator (phase **I**), which has the anomalous orbital Hall effect. Moreover, the intrinsic inter-orbital current order should lead to magneto-optical Kerr or Faraday rotation observable in experiments.

Appendix A

Treatment of the vacancy impurity problem

We treat the vacancy disorder as an impurity scattering problem, since one might anticipate that a vacancy behaves like a strong impurity scatterer for a Bloch wave function. Therefore, we put an on-site impurity energy ϵ_i on each vacancy site $i = i_v$ to mimic vacancy disorder:

$$\begin{aligned} H &= H_{hop} + H_{imp} \\ &= \sum_{i,j} (-t_{ij} - \mu\ \delta_{ij})\ c_i^\dagger c_j + \sum_{i=i_v} V_0\ c_i^\dagger c_i, \end{aligned} \tag{A.1}$$

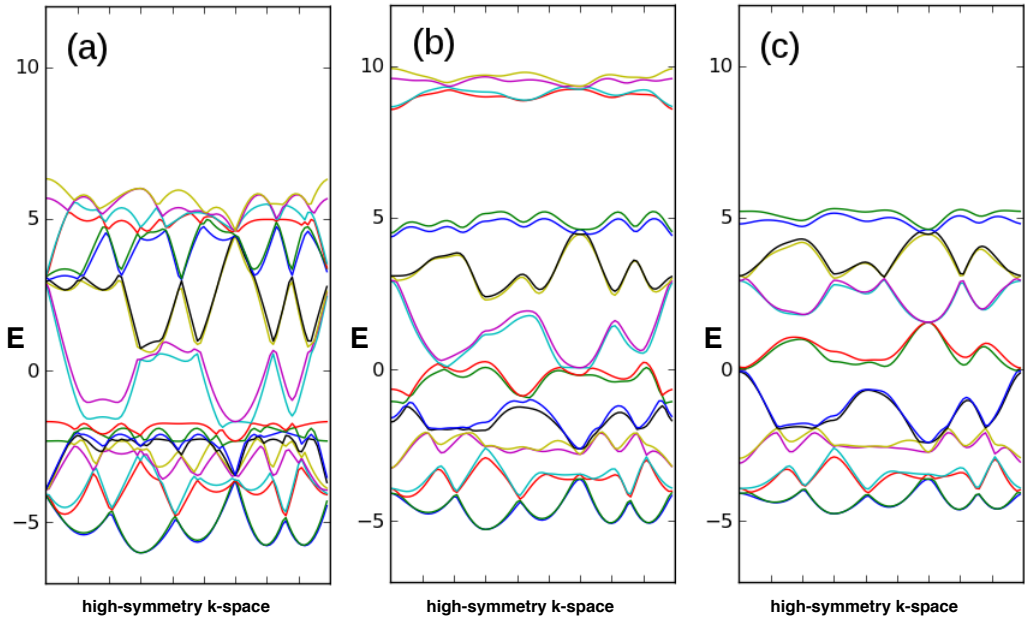

FIGURE A.1: (Color online) The band structure plot in high symmetry axis ($\Gamma \to X \to M \to \Gamma$) for $V_0 = 0$ (a), $V_0 = 2.5$ (b), $V_0 = 100$ (c).

We introduce a new index to describe the $A_{1(2)}; B_{1(2)}$ sub-atoms for unit cell cut "-b-" in Fig. 1.1, $\psi_i^\dagger = (c_{A1}^\dagger, c_{A2}^\dagger, c_{B1}^\dagger, c_{B2}^\dagger)_i$, and linearize the fermionic operator, $c_{A\alpha(B\alpha),i} = (1/\sqrt{N}) \sum_{\mathbf{k}} c_{A\alpha(B\alpha),\mathbf{k}} \times \exp(i\mathbf{k} \cdot R_i)$, to get the 4×4 hopping matrix in $\mathbf{k}$-space, $H_{hop} = \sum_{\mathbf{k}} \psi_{\mathbf{k}}^\dagger M_{\mathbf{k}} \psi_{\mathbf{k}}$,

$$M_{\mathbf{k}} = \begin{pmatrix} \varepsilon_{A,\mathbf{k}} - \mu & \varepsilon_{xy,\mathbf{k}} & \varepsilon_{T,\mathbf{k}} & 0 \\ \varepsilon_{xy,\mathbf{k}} & \varepsilon_{A,\mathbf{k}} - \mu & 0 & \varepsilon_{T,\mathbf{k}} \\ \varepsilon_{T,\mathbf{k}} & 0 & \varepsilon_{B,\mathbf{k}} - \mu & \varepsilon_{xy,\mathbf{k}} \\ 0 & \varepsilon_{T,\mathbf{k}} & \varepsilon_{xy,\mathbf{k}} & \varepsilon_{B,\mathbf{k}} - \mu \end{pmatrix} \tag{A.2}$$

We perform the same linear transformation for the impurity term H_{imp} in the Hamiltonian. There are four independent vacancy ordering vectors as shown in the unit cell cut "-b-" in Fig. 1.1 for $Q_1 = 2\pi(4/5, 2/5), Q_n = nQ_1, n = 1 \cdots 4$. The similar vacancy ordering vectors were obtained in Ref. [69], in the notation of one Fe per unit cell.

By construction H_{imp} enlarges the basis in the $\mathbf{k}$-space,

$$\psi_{\mathbf{k}} \to \psi'_{\mathbf{k}} = (\psi_{\mathbf{k}}, \psi_{\mathbf{k}+\mathbf{Q_1}}, \psi_{\mathbf{k}+\mathbf{Q_2}}, \psi_{\mathbf{k}+\mathbf{Q_3}}, \psi_{\mathbf{k}+\mathbf{Q_4}}). \tag{A.3}$$

In this formulation the diagonal scattering matrix $V = I_{4\times4} \times V_0$ sits in the off-diagonal positions to describe multiple scattering between all vacancy ordered states with different Q_n, Finally, the enlarged Hamiltonian becomes $H = \sum_{\mathbf{k}} \psi_{\mathbf{k}}^{\prime\dagger} W_{\mathbf{k}} \psi'_{\mathbf{k}}$ with

$$W_k = \begin{pmatrix} M_{\mathbf{k}} & V & V & V & V \\ V & M_{\mathbf{k}+\mathbf{Q_1}} & V & V & V \\ V & V & M_{\mathbf{k}+\mathbf{Q_2}} & V & V \\ V & V & V & M_{\mathbf{k}+\mathbf{Q_3}} & V \\ V & V & V & V & M_{\mathbf{k}+\mathbf{Q_4}} \end{pmatrix} \tag{A.4}$$

Note that the impurity potential V_0 not only leads to a reconstruction of the shape of the band structure, it also creates a gap of $2V_0$ between high-energy bands and the low-energy bands. Therefore, we need to shift it back to the origional place, $W_k \to W'_k = W_k + I_{20\times20} \times V_0$.

Figure A.1 shows the calculated band structure for various values of the impurity scattering strength V_0. When $V_0 = 0$, the band structure exhibits an entanglement of 20 bands, which down-folded simplifies to the band structure shown for the four bands in the $\sqrt{2} \times \sqrt{2}$ unit cell of Fig. 1.1(a). The more complicated plot in Fig. A.1(a) it is due to the repeated plotting of different Q_n's in $\mathbf{k}$-space of $M_{\mathbf{k}}$. However, for finite values of V_0 (=2.5) a gap separates the upper four upper bands and 16 lower bands, shown in Fig. A.1(b). Finally, when V_0 approaches the unitarity limit. $V_0 = 100$, as shown

in Fig. A.1(c), the upper four bands are being pushed far above as four independent flat bands, while the lower 16 bands form a simpler shape as the new periodicity with vacancy stripe order sets in. The result for Fig. A.1(c) is stable for all of the values of V_0 that is greater than 100, which means the vacancy order is in the limit of $V_0 \to \infty$.

Appendix B

Details of the D_{2d} symmetry and comparisons to Zhang's model

B.1 The D_{2d} invariant symmetry

We now give the reason for our choice of the D_{2d} symmetry of the point group describing the crystal structure of $BaFe_2As_2$, which is used for the construction of the kinetic Hamiltonian in Eq. (1). To begin with, we draw the three-dimensional (3D) structure of the basic Fe-As building blocks of $BaFe_2As_2$ in Fig. B.1. The D_{2d} symmetry is generated by the group elements C_4 and σ_h as shown in Fig. B.1(b,c). Close inspection reveals the point group symmetry D_{2d}, because combined fourfold rotation (C_4) and mirror reflection (σ_h) leave the crystal structure invariant.

However, the D_{2d} symmetry is obvious only for the 3D crystal structure, while the inclusion of the reflection operation σ_h is not obvious for the two-dimensional (2D) model as shown by Fig. 1(a) in the main text. The question is how one can construct a D_{2d} hopping Hamiltonian on a 2D lattice. The solution is as follows: The As atoms mediate the 2NN hopping (t_3) through their p orbitals between the d orbitals of the Fe sites. As a consequence the upper (lower) As atoms lead to effective hopping terms between the d_{xz} (d_{yz}) orbitals, respectively. Finally, the σ_h operation of the upper/lower As atoms can be mapped onto the exchange of the order of the d_{xz} and d_{yz} orbitals, see Fig. B.1(b). This corresponds to exchanging the upper and lower panels of Fig. 1(b) in the main text.

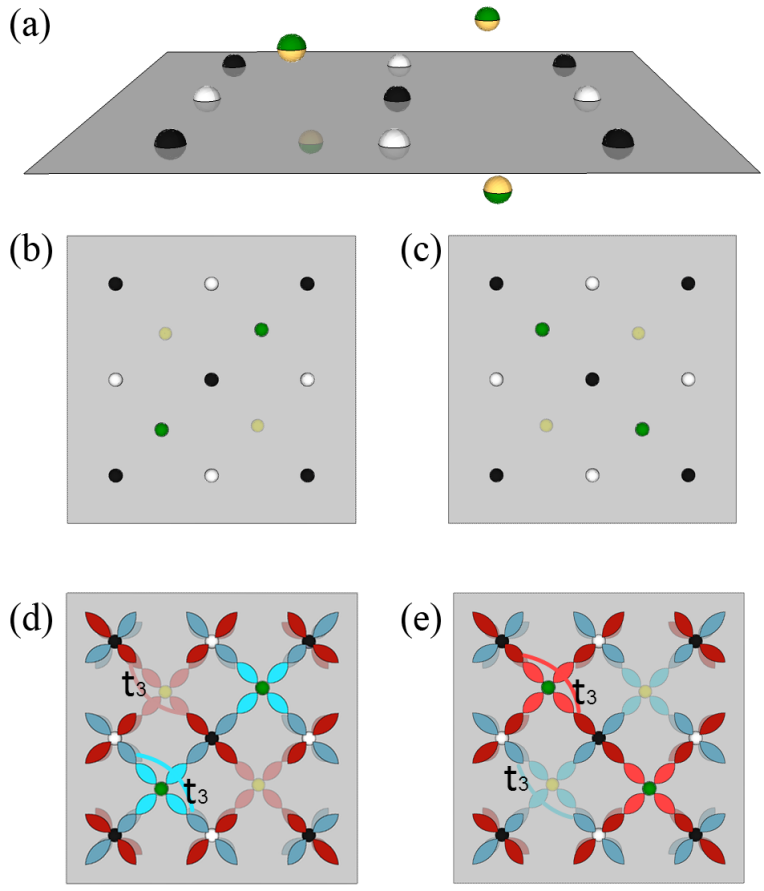

FIGURE B.1: (color online) (a) Schematic picture of D_{2d} point group symmetry of the three-dimensional (3D) structure of the Fe-As building blocks. The colormap is: Fe atoms on the A (black) and B (white) sublattice; the As atoms above (green/yellow) and below (yellow/green). (b) Top view of panel (a); (c) application of symmetry operation C_4 or σ_h on panel (b); (d) orbital ordering and t_3 hopping terms overlayed onto panel (b); (e) the resulting σ_h operation of panel (d).

B.2 Comparisions of H_1 and H_2 under the same parameter set

It is intersting to investigate that how those two models behave under the same parameter set as used in H_2, t_{1-6}=(-1,0.08,1.35,-0.12,0.09,0.25). In Fig. B.3, we show the comparisons of H_1 and H_2 with the evolution of Fermisurface from extreme e-doped one to extreme h-doped one. We can clearly indicated that with condition **II** introduced for H_2 the two conduction bands degenerated alone X-M direction. Additionaly, the electron pocket of H_2 around M points is always sandwiched in between the one of H_1. The area of the Fermi surface of the two models doesn't have much difference in e-doped side, Fig. B.3 (a-c). However, much difference shows up for the h-doped side as shown in Fig. B.3 (d-h). Around M points, the the electron pocket of H_2 shrunk a lot as increase the h-doping and finally shrunk into a tiny Dirac point in Fig. B.3 (g).

Finally, it changed to a hole pocket for H_2. To compare, this electron pocket shrinking for H_2 is not seen in H_1 and H_1 always preserve finite size Fermi surface.

We further calculated the phase diagram for both H_1 and H_2 under the same hopping term and interaction parameters, (U,J_h,V)=(3.2,0.6,1.05). Again, both of H_1 and H_2 shows good abilities in e-doped side. But H_1 behaved differently in the extreme h-doped side. Base on previous Fermi surface analysis, we blame this problem for H_1 as its Fermi surface around M points does not shrunk and remain finite size area. Here a comment for the extra condition **II** added on H_2. The 90° rotation between degenerated d_xz and d_yz orbitals as a twisting and it gives more degeneracies for H_2 alone X-M directions. The resulting effect is the electron pocket around M points shrunk its size and gives the correct Fermi surface evolution.

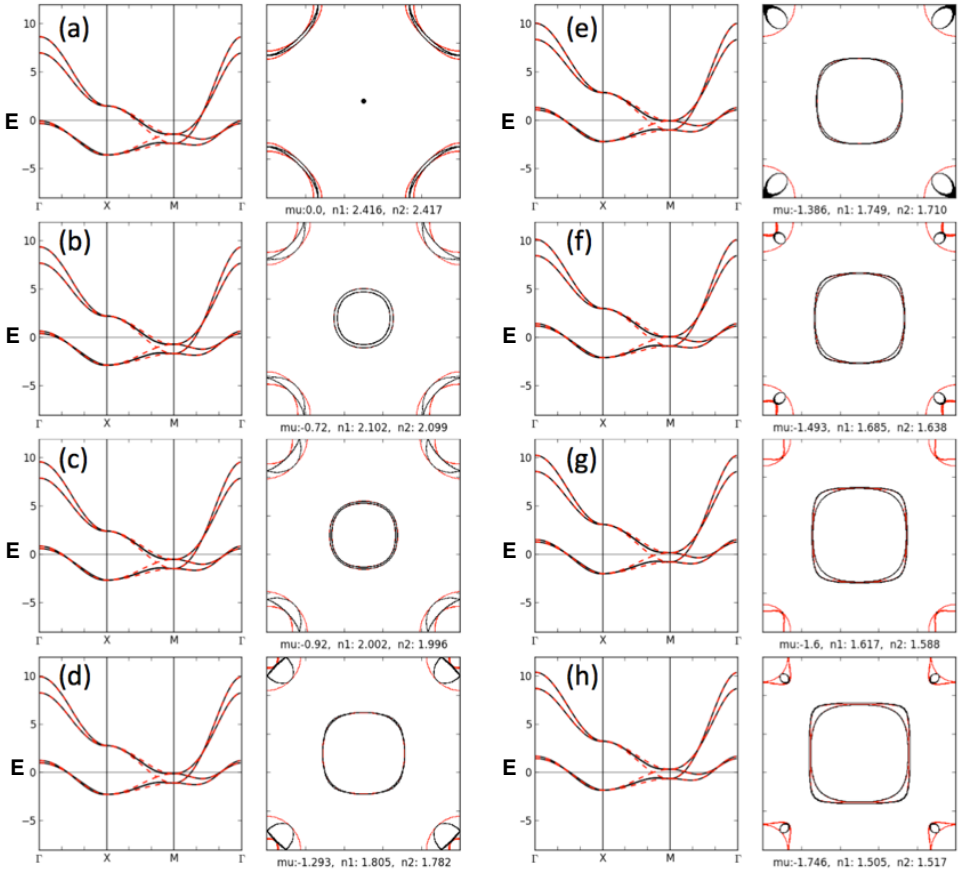

FIGURE B.2: (color online) The compared Fermi surface for model H_1(red) and H_2(black) using the same set of parameters. For each subset, the left panel is the band structure with the Fermi level indicated in the horizontal line, the right panel is the correspond Fermi surface. The alphabetical order indicate the Fermi level from high to low as μ_{a-h} = (0.0,-0.72,-0.92,-1.29,-1.38,-1.49,-1.6,-1.74). The correspond electron occupation is setting right below the Fermi surface panel for n_1 to H_1 and n_2 to H_2.

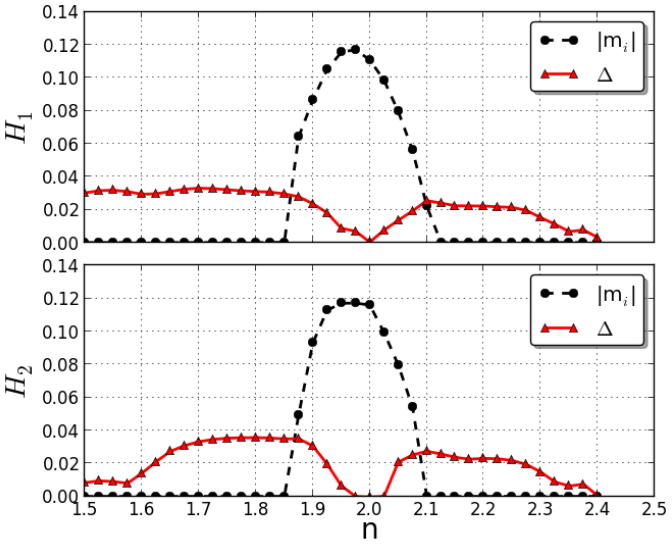

FIGURE B.3: (color online) The calculation of phase diagram for both H_1 and H_2 under the same hopping and interaction parameters. The upper / lower panel is for H_1 / H_2, the black(circle) / red(triangle) line shows the order parameters of AFM / $s_{\pm}$-pairing.

Appendix C

Unfolding transformation of the tight-binding model

Here we derive the unitary transformations for the rotation of orbitals between both Fe sublattices to attain the exact mapping of the 2-by-2 orbital model onto the model of two decoupled two-orbital Hamiltonians.

C.1 Description of the orbital twist argument

As proposed in Ref. [15], the tight-binding Hamiltonian of Eq. (5.1) in the 2-Fe unit cell Brillouin zone (BZ) is given by $\mathcal{H}_0 = \sum_{\mathbf{k}} \psi^\dagger(\mathbf{k})\, \mathbb{W}_{\mathbf{k}}\, \psi(\mathbf{k})$ with

$$\mathbb{W}_{\mathbf{k}} = \begin{pmatrix} \xi^H - \mu & \xi_{12} & \xi_t & \xi_c \\ \xi_{12} & \xi^V - \mu & \xi_c & \xi_t \\ \xi_t & \xi_c & \xi^V - \mu & \xi_{12} \\ \xi_c & \xi_t & \xi_{12} & \xi^H - \mu \end{pmatrix}. \tag{C.1}$$

Here the four-component field operator is defined as ψ=$(d_{A1}$,d_{A2},d_{B1},$d_{B2})^T$ with A, B labeling the sublattice and 1(2) labeling the orbital $d_{yz}(d_{xz})$. The dispersions are given by $\xi^H = 2t_2 \cos k_x + 2t_3 \cos k_y + 4t_6 \cos k_x \cos k_y$, $\xi^V = 2t_3 \cos k_x + 2t_2 \cos k_y + 4t_6 \cos k_x \cos k_y$, $\xi_{12} = 2t_4(\cos k_x + \cos k_y)$, $\xi_t = 4t_1 \cos \frac{k_x}{2} \cos \frac{k_y}{2}$, $\xi_c = 4t_5 \cos \frac{k_x}{2} \cos \frac{k_y}{2}$ with $t_{1-6} = (-1, 0.08, 1.35, -0.12, 0.09, 0.25)$. In Eq. (C.1), the C_4 symmetry of intra-orbital hopping processes between sublattices A and B is broken. As we will show below, there is a degree of freedom to write the Hamiltonian by rotating the local coordinate on the sublattice A or B. The above C_4 symmerty is recovered by a 90° rotation of d_{xz} and d_{yz} orbitals on the sublattice B as illustrated in Fig. C.1(a). Specifically, we define

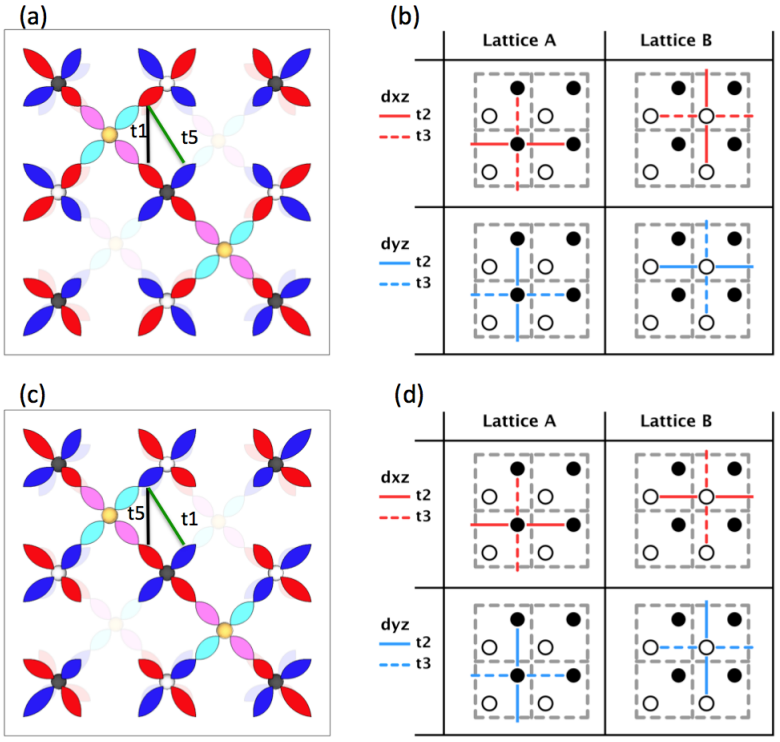

FIGURE C.1: (Color online) Two choices of the basis (a), (b)[(c), (d)] with[without] a 90° rotation of the local coordinate system on sublattice B. Panels (a), (c) show the d_{xz} and d_{yz} orbital symmetry and the overlap through As-$p_{x/y}$ orbitals: the NNN intra-(inter-) hopping terms t_1 (t_5) are indicated by the black (green) solid lines. Panels (b), (d) illustrate the NNN intraorbital hopping terms for $t_2(t_3)$ in solid (dashed) lines. Note that the coordinates of (a) and (c) have a 45° rotation from (b) and (d).

a new basis under the unitary transformation $\phi = (d'_{A1}, d'_{A2}, d'_{B1}, d'_{B2})^T = U\psi$ with

$$U = \begin{pmatrix} 1 & 0 & 0 & 0 \\ 0 & 1 & 0 & 0 \\ 0 & 0 & 0 & 1 \\ 0 & 0 & 1 & 0 \end{pmatrix}. \tag{C.2}$$

Namely, the unitary transformation U flips the orbitals d_{xz} and d_{yz} on the sublattice B. The corresponding Hamiltonian has the form $\mathcal{H}_0 = \sum_{\mathbf{k}} \phi^\dagger(\mathbf{k}) \mathbb{W}'_{\mathbf{k}} \phi(\mathbf{k})$ with

$$\mathbb{W}'_{\mathbf{k}} = U\mathbb{W}_{\mathbf{k}}U^\dagger = \begin{pmatrix} \xi^H - \mu & \xi_{12} & \xi_c & \xi_t \\ \xi_{12} & \xi^V - \mu & \xi_t & \xi_c \\ \xi_c & \xi_t & \xi^H - \mu & \xi_{12} \\ \xi_t & \xi_c & \xi_{12} & \xi^V - \mu \end{pmatrix}. \tag{C.3}$$

C.2 Mapping onto the 1-Fe per unit cell Hamiltonian

Note that $\mathbb{W}'_{\mathbf{k}}$ in Eq. (C.3) has the same 2×2 block matrix for sublattices A and B. By the symmetry analysis, the entire Hamiltonian can be written in the basis $\phi = (d_1, d_2)^T$ of the 1-Fe unit cell . The resulting Hamiltonian $\mathcal{H}^0 = \sum_{\mathbf{k}} \phi^\dagger_{\mathbf{k}} \mathbb{M}_{\mathbf{k}} \phi_{\mathbf{k}}$ takes the following form

$$\mathbb{M}_{\mathbf{k}} = \begin{pmatrix} \xi_1 - \mu & \xi_{12} \\ \xi_{21} & \xi_2 - \mu \end{pmatrix}, \tag{C.4}$$

where $\xi_1 = E_x + E_t$, $\xi_2 = E_y + E_t$ and $\xi_{12} = \xi_{21} = E_c$. Each component is defined as

$$\begin{aligned} E_t &= 2t_1[\cos k_x + \cos k_y] + 2t_6[\cos 2k_x + \cos 2k_y], \\ E_x &= 2(t_2 + t_3)\cos k_x \cos k_y + 2(t_2 - t_3)\sin k_x \sin k_y, \\ E_y &= 2(t_2 + t_3)\cos k_x \cos k_y - 2(t_2 - t_3)\sin k_x \sin k_y, \\ E_c &= 2t_5[\cos k_x + \cos k_y] + 4t_4 \cos k_x \cos k_y, \end{aligned} \tag{C.5}$$

with a new set of hopping parameters $t_{1-6} = (0.09, 0.08, 1.35, -0.12, -1, 0.25)$. Figure C.2(a) and (b) shows the band structure and Fermi surface with half electron filling in the BZ corresponding to 1-Fe per unit cell and the Dirac dispersions can be observed around X and Y points. The comparison between the 1-Fe band structure and 2-Fe band structure is shown in Fig. C.2(c). The 1-Fe band structure can be nicely folded onto the 2-Fe band structure. The folded Fermi surfaces are also presented in Fig. C.2(d). The corresponding band dispersions in the reduced BZ are given by the block-structured matrix

$$\mathbb{W}''_{\mathbf{k}} = \begin{pmatrix} \mathbb{M}_{\mathbf{k}} & 0 \\ 0 & \mathbb{M}_{\mathbf{k}+\mathbf{Q}} \end{pmatrix}, \tag{C.6}$$

with the folding vector $\mathbf{Q} = (\pi, \pi)$.

We next prove that the $\mathbb{W}''_{\mathbf{k}}$ is just a gauge transform from $\mathbb{W}'_{\mathbf{k}}$. The explicit form of band dispersions in 2-Fe unit cell is given by

$$\begin{aligned} \{\xi^H, \xi^V\} =& \{t_2, t_3\}\,[e^{i\mathbf{k}\cdot\hat{x}} + e^{-i\mathbf{k}\cdot\hat{x}}] + \{t_3, t_2\}\,[e^{i\mathbf{k}\cdot\hat{y}} + e^{-i\mathbf{k}\cdot\hat{y}}] \\ &+ t_6\,[e^{i\mathbf{k}\cdot(\hat{x}+\hat{y})} + e^{-i\mathbf{k}\cdot(\hat{x}+\hat{y})} + e^{i\mathbf{k}\cdot(\hat{x}-\hat{y})} + e^{-i\mathbf{k}\cdot(\hat{x}-\hat{y})}], \\ \{\xi_t, \xi_c\} =& \{t_1, t_5\}\,[e^{i\mathbf{k}\cdot(\hat{x}+\hat{y})/2} + e^{-i\mathbf{k}\cdot(\hat{x}+\hat{y})/2} \\ &+ e^{i\mathbf{k}\cdot(\hat{x}-\hat{y})/2} + e^{-i\mathbf{k}\cdot(\hat{x}-\hat{y})/2}], \\ \xi_{12} =& t_4\,[e^{i\mathbf{k}\cdot\hat{x}} + e^{-i\mathbf{k}\cdot\hat{x}} + e^{i\mathbf{k}\cdot\hat{y}} + e^{-i\mathbf{k}\cdot\hat{y}}]. \end{aligned} \tag{C.7}$$

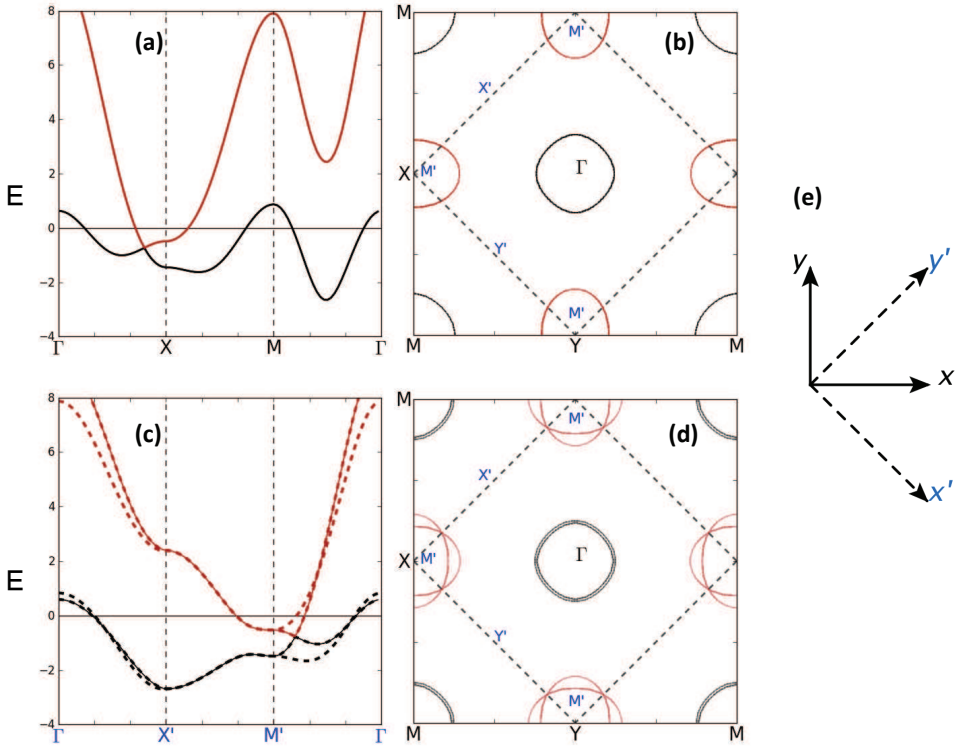

FIGURE C.2: (Color online) Calculated band structure (a) and Fermi surface (b) in unfolded (1-Fe per unit cell) BZ. Here the Fermi energy is shifted to zero for 1/2 filling. (c) The folded band structure of the 1-Fe (green solid line) to 2-Fe per unit cell band structure (dashed line), which is identical to that calculated directly from the Hamiltonian before the gauge transformation. (d) The Fermi surfaces of the 2-Fe band structure. (e) The transformation between the coordinates in the 1-Fe per unit cell (solid lines) and 2-Fe per unit cell (dashed lines) systems.

By the help of the re-definition of $(\hat{x},\hat{y}) \to (\hat{x}+\hat{y},\hat{x}-\hat{y})$, The band dispersions written in 1-Fe unit cell basis have the from

$$\begin{aligned}
\{\xi^H,\xi^V\} =& \{t_2,t_3\}\,[e^{i\mathbf{k}\cdot(\hat{x}+\hat{y})}+e^{-i\mathbf{k}\cdot(\hat{x}+\hat{y})}] \\
&+\{t_3,t_2\}\,[e^{i\mathbf{k}\cdot(\hat{x}-\hat{y})}+e^{-i\mathbf{k}\cdot(\hat{x}-\hat{y})}], \\
&+t_6\,[e^{i\mathbf{k}\cdot(2\hat{x})}+e^{-i\mathbf{k}\cdot(2\hat{x})}+e^{i\mathbf{k}\cdot(2\hat{y})}+e^{-i\mathbf{k}\cdot(2\hat{y})}], \\
\{\xi_t,\xi_c\} =& \{t_1,t_5\}\,[e^{i\mathbf{k}\cdot\hat{x}}+e^{-i\mathbf{k}\cdot\hat{x}}+e^{i\mathbf{k}\cdot\hat{y}}+e^{-i\mathbf{k}\cdot\hat{y}}], \\
\xi_{12} =& t_4\,[e^{i\mathbf{k}\cdot(\hat{x}+\hat{y})}+e^{-i\mathbf{k}\cdot(\hat{x}+\hat{y})}+e^{i\mathbf{k}\cdot(\hat{x}-\hat{y})}+e^{-i\mathbf{k}\cdot(\hat{x}-\hat{y})}],
\end{aligned} \tag{C.8}$$

Then we shall consider $\mathbb{W}'_{\mathbf{k}}$ with the new elements of Eq. (C.8) and $\mathbf{k}$ running over the BZ corresponding to 1-Fe per unit cell. Here, we rewrite $\mathbb{W}'_{\mathbf{k}}$ in the block matrix form

$$\mathbb{W}'_{\mathbf{k}} = \begin{pmatrix} \mathbb{A} & \mathbb{B} \\ \mathbb{B} & \mathbb{A} \end{pmatrix} \tag{C.9}$$

with

$$\mathbb{A} = \begin{pmatrix} \xi^H & \xi_{12} \\ \xi_{12} & \xi^V \end{pmatrix} \tag{C.10}$$

and

$$\mathbb{B} = \begin{pmatrix} \xi_c & \xi_t \\ \xi_t & \xi_c \end{pmatrix}. \tag{C.11}$$

For the convenience of discussion, we have set the chemical potential μ to be zero. Here we introduce a gauge transform $\eta(\mathbf{k}) = (d_{1\mathbf{k}}, d_{2\mathbf{k}}, d_{1\mathbf{k}+\mathbf{Q}}, d_{2\mathbf{k}+\mathbf{Q}})^T = K\psi(\mathbf{k})$ with

$$K = \frac{1}{\sqrt{2}} \begin{pmatrix} \mathbb{1} & -\mathbb{1} \\ -\mathbb{1} & -\mathbb{1} \end{pmatrix}, \tag{C.12}$$

where $\mathbb{1}$ is a 2×2 identity. The gauge transform K satisfies $K^\dagger K = \mathbb{1}_{4\times4}$. A little algebra leads to

$$\begin{aligned} \mathcal{H}_0 &= \sum_{\mathbf{k}} \psi^\dagger(\mathbf{k}) K^\dagger K \mathbb{W}'_{\mathbf{k}} K^\dagger K \psi(\mathbf{k}) \\ &= \sum_{\mathbf{k}} \eta^\dagger(\mathbf{k}) K \mathbb{W}'_{\mathbf{k}} K^\dagger \eta(\mathbf{k}) \end{aligned} \tag{C.13}$$

with

$$K^\dagger \mathbb{W}'_{\mathbf{k}} K = \begin{pmatrix} \mathbb{A}+\mathbb{B} & 0 \\ 0 & \mathbb{A}-\mathbb{B} \end{pmatrix}. \tag{C.14}$$

Here $\mathbb{A}$ and $\mathbb{B}$ matrices follow $\mathbb{A}(\mathbf{k}) = \mathbb{A}(\mathbf{k}+\mathbf{Q})$ and $\mathbb{B}(\mathbf{k}) = -\mathbb{B}(\mathbf{k}+\mathbf{Q})$, respectively. By carefully collecting terms in Eq. (C.14), we confirm that

$$K^\dagger \mathbb{W}'_{\mathbf{k}} K = \begin{pmatrix} \mathbb{M}_{\mathbf{k}} & 0 \\ 0 & \mathbb{M}_{\mathbf{k}+\mathbf{Q}} \end{pmatrix} = \mathbb{W}''_{\mathbf{k}}. \tag{C.15}$$

By combining these results for the unitary transformations U and K, we can map the 2-by-2 onto the 1-by-2 Hamiltonian: $\mathbb{W}''_{\mathbf{k}} = K^\dagger \mathbb{W}'_{\mathbf{k}} K = K^\dagger U \mathbb{W}_{\mathbf{k}} U^\dagger K$.

Appendix D

Supplementary material for Chapter 6.

D.1 Mean-field formalism and calculation

In this section we derive the meanfield form of the coulomb interaction. The Hamiltonian we interest is in the form, $H^s = H^0 + H^U + H^V$ (the superscript, s, stands for spinful). Here, we write down the form of in real-space,

$$\begin{aligned} H^0 &= \sum_{ij,\alpha\beta,\sigma} (t_{ij}^{\alpha\beta} - \mu\,\delta_{ij}\delta_{\alpha\beta}) c_{i\alpha,\sigma}^{\dagger} c_{j\beta,\sigma}, \\ H^U &= \sum_{i,\alpha,\sigma} U\; n_{i\alpha,\sigma}\, n_{i\alpha,\sigma'}, \\ H^V &= \sum_{i\neq j,\alpha\neq\beta,\sigma} V_{ij,\alpha\beta}\; n_{i\alpha,\sigma}\, n_{j\beta,\sigma}. \end{aligned} \tag{D.1}$$

Where H^0 is the hopping terms in present of 1-Fe / unitcell [15, 209], the non-zero terms are depict as follows,

$$\begin{aligned} t_1 &= t_{\pm\hat{x}}^{\alpha\alpha} = t_{\pm\hat{y}}^{\alpha\alpha} = 0.09, \\ t_2 &= t_{\pm(\hat{x}-\hat{y})}^{11} = t_{\pm(\hat{x}+\hat{y})}^{22} = 0.08, \\ t_3 &= t_{\pm(\hat{x}+\hat{y})}^{11} = t_{\pm(\hat{x}-\hat{y})}^{22} = 1.35, \\ t_4 &= t_{\pm(\hat{x}\pm\hat{y})}^{\alpha\bar{\alpha}} = -0.12, \\ t_5 &= t_{\pm\hat{x}}^{\alpha\bar{\alpha}} = t_{\pm\hat{y}}^{\alpha\bar{\alpha}} = -1, \\ t_6 &= t_{\pm 2\hat{x}}^{\alpha\alpha} = t_{\pm 2\hat{y}}^{\alpha\alpha} = 0.25. \end{aligned} \tag{D.2}$$

H^U is the on-site intra orbital Hubbard interaction and H^V is the inter-orbital ($\alpha \neq \beta$) Coulomb interaction between site i and j. Note that, we've also considered the intra orbital Coulomb interaction ($\alpha = \beta$) and we found no interesting phases can be found

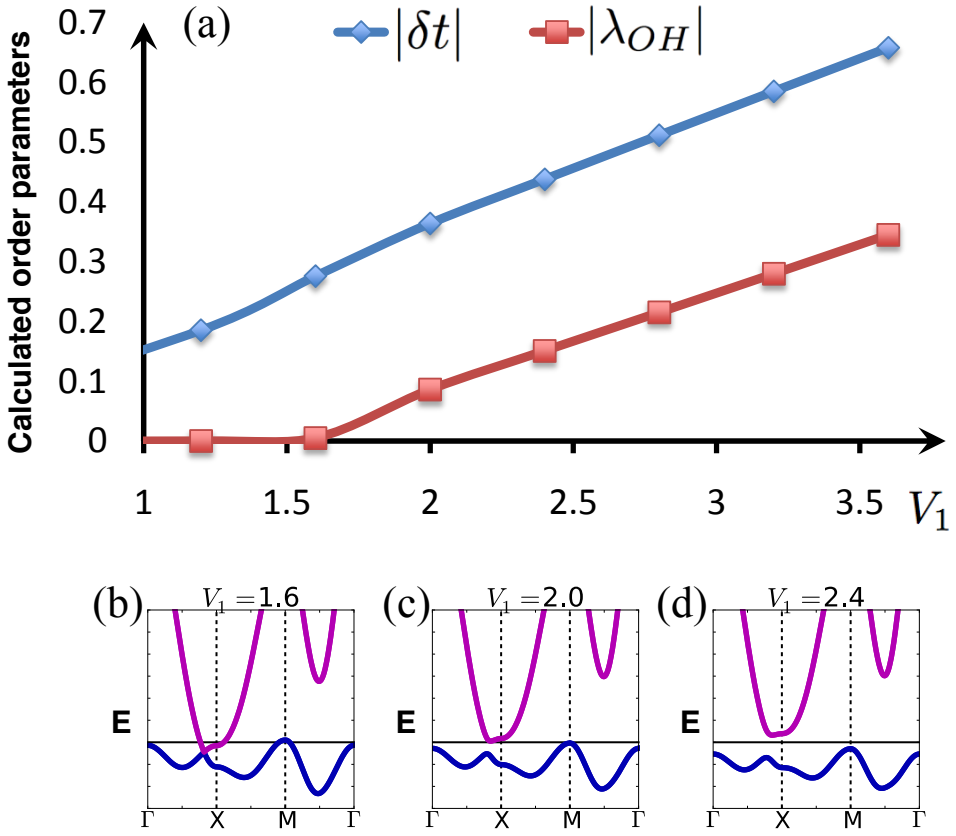

FIGURE D.1: (color online) (a) The mean-field calculated order parameters of H^{OH} term, where $\delta t/\lambda_{OH}$ belong to the real/image part of it. (b),(c) and (d) is the k-space band structure of 1-Fe/unitcell BZ under different strength of V_1.

in our calculation. We treat H^U and H^V by mean-field expansion. For H^U we have,

$$H^U = U \sum_{i\alpha,\sigma\neq\sigma'} \langle n_{i\alpha\sigma}\rangle \, n_{i\alpha\sigma'}. \tag{D.3}$$

H^V has two ways for the mean-field decoupling, $H^V = H^{CDW} + H^{OH}$, where,

$$\begin{aligned} H^{CDW} &= \sum_{i\neq j,\alpha\neq\beta,\sigma} V_{ij} \, \langle n_{i\alpha\sigma}\rangle \, n_{j\beta\sigma} \\ H^{OH} &= -\sum_{i\neq j,\alpha\neq\beta,\sigma} V_{ij} \langle c^\dagger_{i\alpha,\sigma} \, c_{j\beta,\sigma}\rangle c^\dagger_{j\beta,\sigma} \, c_{i\alpha,\sigma} \end{aligned} \tag{D.4}$$

Here we only calculate the nearest neighbor ($V_{\langle ij\rangle}$=V_1). In a bulk (periodic 2D) calculation, the CDW term is not a preffered state and only H^{OH} has stable solution with finite value of V_1. The Hubbard term, with U=3.2, does not contribute to a finite magnetism to this system.

TABLE D.1: The matrix elements of $\epsilon_{ij}^{\alpha\beta}$. It also preserve the translational symmetry of 1-Fe / unitcell and the C_{4v} point group symmetry.

	$i \pm \hat{x}, d_{xz}$	$i \pm \hat{x}, d_{yz}$	$i \pm \hat{y}, d_{xz}$	$i \pm \hat{y}, d_{yz}$
i, d_{xz}	0	1	0	-1
i, d_{yz}	-1	0	1	0

Now, we define the meanfield calculated orbital current flux order from H^{OH},

$$\chi_{\alpha\beta,\sigma}^{ij} \equiv V_1 \langle c_{i\alpha,\sigma}^{\dagger} c_{j\beta,\sigma} \rangle \tag{D.5}$$

The meanfield calculated χ is a complex number with real and imaginary part,

$$\begin{aligned} \delta t &= \mathrm{Re}\,\chi, \\ \lambda_{OH}^{\sigma} &= \epsilon_\sigma \,|\mathrm{Im}\,\chi_\sigma|, \quad \epsilon_\sigma \in \pm 1 \end{aligned} \tag{D.6}$$

The first term, δt, is always negative and homogeneous in real space. It will contribute to H^0 to its nearest neighbor inter-orbital hopping term t_5 [209]. The second term, λ_{OH}^{σ}, is the generator for the orbital-hall effect. Therefore we can use it to express the orbital-current flux order, $i\,\mathrm{Im}\,\chi_{\alpha\beta,\sigma}^{ij} = i\,\lambda_{OH}^{a}\,\epsilon_{ij}^{\alpha\beta}$ and H^{OH} can be easily rewrite,

$$H^{OH} = i\,\lambda_{OH}^{\sigma} \sum_{ij,\alpha\neq\beta,\sigma} \epsilon_{ij}^{\alpha\beta}\; c_{i\alpha,\sigma}^{\dagger} c_{j\beta,\sigma}, \tag{D.7}$$

where $\epsilon_{ij}^{\alpha\beta}$ is expressed in Table. D.1 and the real part of H^{OH} has been absorbed into the hopping terms. Fig. D.1(b) shows that the Fermi surface is shifted downward in Γ/M points with the contribution of δt only. Once the image part λ_{OH} is involved, the bulk Dirac cond will be destroied immediately as shown in Fig. D.1(c) and the shows the gap. The gap is becomeing larger with larger value of λ_{OH} as shown in Fig. D.1(d).

D.2 Ground state with exchange interaction

Without introduce more terms, we have two degenerated phases, $\epsilon_\uparrow = \pm\epsilon_\downarrow$, of H^{OH} as described in the main-text. Now we discuss one possiblility which can lift the degeneracy. The on-site Hubbard interaction is usually contain a Hund's coupling J [19]. However, without loosing generality, this term is more complicated with more terms to be involved which was discussed by K. Sano and co-authors [215]. Here we introduce only one more term from K. Sano's paper,

$$H^{J} = -J \sum_{i\alpha} (c_{i,\alpha,\uparrow}^{\dagger} c_{i,\alpha,\downarrow}\, c_{i,\bar{\alpha},\downarrow}^{\dagger} c_{i,\bar{\alpha},\uparrow} + h.c), \tag{D.8}$$

We mean-field decouple H^J terms,

$$H^J = \lambda_J \sum_{i\alpha} (c^\dagger_{i,\alpha,\uparrow} c_{i,\alpha,\downarrow} + c^\dagger_{i,\bar{\alpha},\downarrow} c_{i,\bar{\alpha},\uparrow} + h.c), \tag{D.9}$$

Where the mean-field order parameter, λ_J, is defined, $\lambda_J = -J \langle c^\dagger_{i,\alpha,\sigma} c_{i,\alpha,\bar{\sigma}} \rangle$. Finally, if we plugin Eq. D.9 into H by manuly giving small and real values of λ_J and we found that **Phase (II)** ($\epsilon_\uparrow = -\epsilon_\downarrow$) is the preffered ground state (no matter how small λ_J is).

D.3 The Hamiltonian in momentum representation

In this section we Fourier transform H into **k**-space with those mean-field calculated order λ_{OH} and the manuly added terms λ_0 and λ_1 in 1-Fe / unit cell frame work. We firstly focus on the spinless Hamiltonian, $H[\delta t; \lambda_{OH,0,1}; \epsilon_a] = \frac{1}{N} \sum_k \psi^\dagger_k \hat{H}(\delta t; \lambda_{OH,0,1}; \epsilon_a) \psi_k$, where $\psi_k = (c_{k,1}, c_{k,2})^T$ and c_1/c_2 stands for anihilate electron on d_{xz}/d_{yz} orbital and $\hat{H} = E_0 + \vec{R} \cdot \vec{\tau}$. Here $\vec{R} = (X, Y, Z)$ and $\vec{\tau}$ is the Pauli matrix,

$$\begin{aligned}
E_0 =& 2\,t_1\,[\cos(k_x) + \cos(k_y)\,] + 2\,t_6\,[\cos(2k_x) + \cos(2k_y)\,] \\
&+ 2\,t_s\,[\cos(k_x)\,\cos(k_y)\,] - \mu, \\
X =& 4\,t_4\,[\cos(k_x)\,\cos(k_y)\,] + 2\,(t_5 + \delta t)\,[\cos(k_x) + \cos(k_y)\,] \\
Y =& 2\,\epsilon_a \lambda_{OH} [\cos(k_x) - \cos(k_y)] + \lambda_1, \\
Z =& 2\,t_d\,[\sin(k_x)\,\sin(k_y)\,] + \lambda_0.
\end{aligned} \tag{D.10}$$

More specifically,

$$\hat{H} = \begin{pmatrix} E_0 + Z, & X - iY \\ X + iY, & E_0 - Z \end{pmatrix}. \tag{D.11}$$

Eq. D.11 has been used in the main-text for the calculation of Chern number.

Here we write down the spinful Hamiltonian with the Rashba spin-orbital coupling term in a 4×4 matrix,

$$\hat{H}_s(\lambda_{OH,0,1,R}) = \begin{pmatrix} \hat{H}(\epsilon_\uparrow = 1), & i\lambda_R \sigma_z \\ -i\lambda_R \sigma_z, & \hat{H}(\epsilon_\downarrow = -1) \end{pmatrix}. \tag{D.12}$$

Eq. D.12 has been used in the main-text for the calculation of Z_2 properties.

D.4 Two types of C_{4v} structure

As shown in Fig. D.2, the C_{4v} symmetry could have two different types and the second type can generate bulk Dirac cones in between Γ-X directions as in our model. We focus on the k-dependent intra-orbital hopping energies for the C_{4v} symmetry, $H^{xz,yz} =$

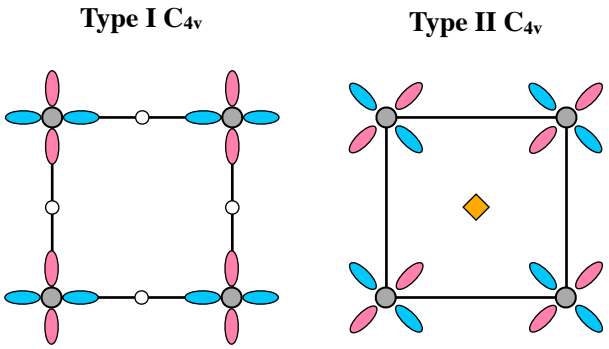

FIGURE D.2: (color online) Two types of C_{4v} structure: I. Left panel, the orbital orientation along the nearest neighbor (NN) bonding direction. II. Right panel, the orbital orientation along the next nearest neighbor (NNN) bonding direction. The blue / red colors represent for d_{xz} / d_{yz} orbitals.

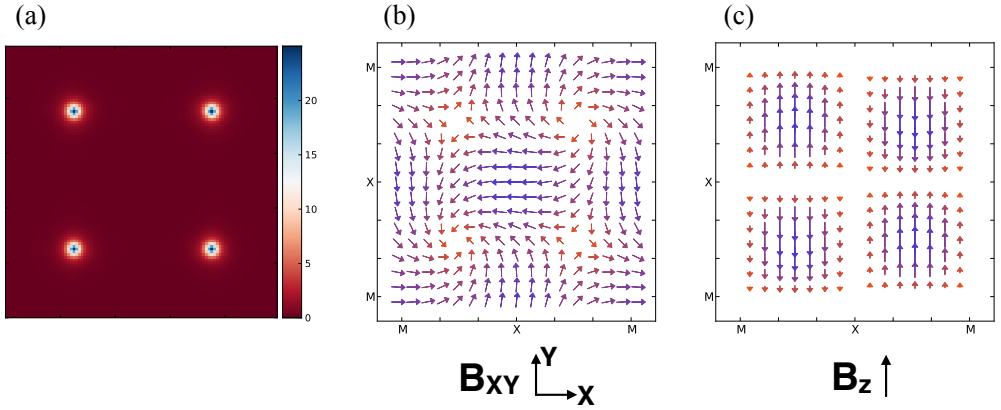

FIGURE D.3: (color online) (a) Calculated Berry curvature of the simplified Hamiltonian, $\tilde{H}(\mathbf{k})$. (b) / (c) are the B-field XY / Z component of, $\tilde{H}(\mathbf{k})$.

$\sum_k [\epsilon_{xz}(k)\, c^\dagger_{xz,k} c_{xz,k} + \epsilon_{xz}(k)\, c^\dagger_{yz,k} c_{yz,k} + \cdots]$ with

$$\begin{aligned} \epsilon_{xz} &= -2\,t\,\cos(\mathbf{k}\cdot\vec{a}_1), \\ \epsilon_{yz} &= -2\,t\,\cos(\mathbf{k}\cdot\vec{a}_2), \end{aligned} \tag{D.13}$$

where $\vec{a}_{1,2}$ are orthogonal to each other and they indicated the bonding direction of the effective hopping term, t. If we choose $\vec{a}_1 = (1,0)$ and $\vec{a}_2 = (0,1)$ then this correspond to the type I C_{4v} structure [208]. While if we choose $\vec{a}_1 = (1,1)$ and $\vec{a}_2 = (-1,1)$ then it becomes,

$$\hat{H}^{xz,yz} = -2\,t\big(I\cos(k_x)\cos(k_y) + \tau_z \sin(k_x)\sin(k_y)\big), \tag{D.14}$$

which gives the form of τ_z term in our spinless Hamiltonian.

D.5 Topological defects as the generator of Berry flux

The anomalous Hall effect of ± 2 Chern number is a combined effect of X, Y and Z. The Chern number can be easily calculated through the area integration of Berry curvature,

$$\Omega(k)^{\pm} = i\frac{\langle\pm|\frac{\partial\hat{H}(k)}{\partial k_x}|\mp\rangle\langle\mp|\frac{\partial\hat{H}(k)}{\partial k_y}|\pm\rangle - (k_x \leftrightarrow k_y)}{(E_{\pm} - E_{\mp})^2}. \tag{D.15}$$

In viewing the symmetry of $\vec{R}$, we know that the Dirac-cones can be re-defined by taking any two component of it. Let us now consider the simplified Hamiltonian from Eq. D.10,

$$\begin{aligned}
\tilde{E}_0 =& 0 \\
\tilde{X} =& t^x\big(4\,t^4\,[\cos(k_x)\,\cos(k_y)\,] + 2\,t^5\,[\cos(k_x) + \cos(k_y)\,]\big) \\
\tilde{Y} =& t^y\big(2\,\lambda_{OH}[\cos(k_x) - \cos(k_y)]\big), \\
\tilde{Z} =& t^z\big(2\,(t_2 - t_3)[\sin(k_x)\,\sin(k_y)\,]\big).
\end{aligned} \tag{D.16}$$

In Eq. D.16, $\tilde{E}_0$ can be regarded as a constant shift and has no contribution to the topology. In the main-text, the four Dirac-cones was generate with $t^{x,y,z} = (1, 0, 1)$ and $\tilde{Y}$ is regarded as perturbation to open the gap. Here if we choose $t^{x,y,z} = (1, 1, 0)$, the Dirac-cones are setting on $(\pm\frac{\pi}{2}, \pm\frac{\pi}{2})$ and $(\pm\frac{\pi}{2}, \mp\frac{\pi}{2})$. Now, we turn on t^z in a small value, the Dirac-degeneracy will be opened and the calculated Chern number is ± 2 for each band. The correspond Berry-curvature is showing in Fig. D.3 (a), four high intensity spots can be found on the Dirac-cones. If we regard these four Dirac-cones as topological defects of a B-field Hamiltonian acting on the pseudo-spin degree of freedom, $\mathbf{B}\cdot\vec{\tau}$, where $\mathbf{B} = (\tilde{X}, \tilde{Y}, \tilde{Z})$, we can map out the B_{xy} (in-plane) and B_z (out-plane) in Fig. D.3 (b) and (c). Therefore, it is easy to know that each B-field winding around the Dirac-cone gives π and hence we have Chern number $= \pm 4\pi/2\pi = \pm 2$.

D.6 The Berry connection and counting of Chern number

Here, we derive the analytic form of the Berry connection of the Berry phase (Chern number), $\gamma^- = 2\pi\,\mathcal{C}^- = \int_{\mathbb{C}} d\vec{k}\cdot\mathcal{A}_-(k)$, where,

$$\begin{aligned}
\mathcal{A}_-(k) =& i\langle -, k|\,\bigtriangledown_k\,|-, k\rangle \\
=& (\frac{X\partial_x Y - Y\partial_x X}{2R^2 + 2ZR}, \frac{X\partial_y Y - Y\partial_y X}{2R^2 + 2ZR}).
\end{aligned} \tag{D.17}$$

Here, $\partial_{x/y}$ is the short hand of ∂_{k_x/k_y}.

The calculated vector field of $\mathcal{A}_-(k)$ is shown in Fig. D.4(a). We can find several high symmetry points are zeros and two of them are the singularities. As shown in Fig. D.4 the torous BZ has no boundary, the line integral around the edges has no

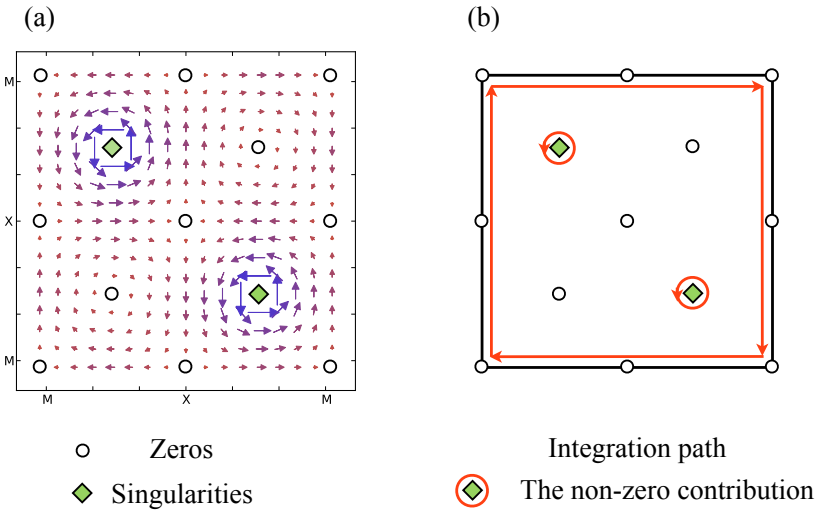

FIGURE D.4: (color online) (a) The vector field of $\mathcal{A}_{-}(k)$. (b) The contour integration of (a).

contribution. The only contribution came from the contour integration which bypass the singularities of $\mathcal{A}_{-}(k)$ and each singularity contribute value of 2π which results the ± 2 of Chern number. The evaluation of the line integral of singularities can be easily obtained from the gauge smoothing process of $\mathcal{A}_{-}(k)$.

D.7 Symmetry analysis of the time and mirror invariance

In this section, we discuss the symmetry classification of phases **I** and **II** of the spinful Hamiltonian with spin degrees of freedom. A detailed account of the symmetry operators used in the main text is given. The spinful Hamiltonian in **k**-space of fermions is defined by $H^s = \phi^{\dagger}_{\mathbf{k}} \hat{H}_s(\mathbf{k}) \phi_{\mathbf{k}}$, where $\phi_{\mathbf{k}} = (c_{\mathbf{k},1\uparrow}, c_{\mathbf{k},2\uparrow}, c_{\mathbf{k},1\downarrow}, c_{\mathbf{k},2\downarrow})^T$. We re-write $\hat{H}_s$ as a direct tensor product of Pauli matrices in the combined orbital pseudo-spin and spin spaces, $\hat{H}_s^{I,II} = X\,\tau_x \otimes I + Z\,\tau_z \otimes I + \hat{H}_{AOH}^{I,II}$, where the orbital flux term, $\hat{H}_{AOH}^{I,II}$, of phases **I** and **II** is either $\hat{H}_{AOH}^{I} = Y\tau_y \otimes I$ or $\hat{H}_{AOH}^{II} = Y\tau_y \otimes \sigma_z$. Here I is the 2×2 unity matrix in spin space.

D.7.1 Intrinsic inversion symmetry and TR symmetry violation of spinless $\hat{H}$

We start our symmetry analysis by noting that the quasi-2D Hamiltonian of spinless fermions, $\hat{H}$, in a tetragonal system has intrinsic inversion symmetry $\hat{H}(\mathbf{k}) = \hat{H}(-\mathbf{k})$. This corresponds to a 180^o rotation in the k_x-k_y plane. Moreover, for the spinless Hamiltonian the time-reversal (TR) operator is given by the charge conjugation operator,

$\mathbf{T} = \mathbf{K}$, and satisfies the relation

$$\begin{aligned}\mathbf{T}\,\hat{H}[\lambda_{AOH}](\mathbf{k})\,\mathbf{T}^{-1} =& \hat{H}[-\lambda_{AOH}](-\mathbf{k}) \\ =& \hat{H}[-\lambda_{AOH}](\mathbf{k}),\end{aligned} \tag{D.18}$$

which tells us that the TR symmetry is violated, because it reverses the orbital current direction from $\lambda_{AOH} \to -\lambda_{AOH}$.

D.7.2 Parity or mirror invariance of spinless $\hat{H}$

In addition to the inversion symmetry, the spinless quasi-2D Hamiltonian is invariant under mirror reflections. The two mirror axes x and y obey the parity operation

$$\mathbf{P}\,\hat{H}(k_x, k_y)\,\mathbf{P}^{-1} = \hat{H}(\pm k_x, \mp k_y), \tag{D.19}$$

respectively, with $\mathbf{P} = \tau_x\mathbf{K}$. This statement is universally true for our model Hamiltonians and applies also to phases **I** and **II** of the spinful Hamiltonian. Note that in 2D the parity operation is a mirror reflection, which flips the sign of only one coordinate, otherwise it would be a rotation.

D.7.3 Parity and mirror invariance of phase II of spinful $\hat{H}_s$

The spinful Hamiltonian for fermions with spin degrees of freedom satisfies similar symmetry operations as before. However, now we need to pay attention to the fact that the mirror and TR operators flip the spin of the fermion and must be defined in the enlarged $SU(2)\otimes SU(2)$ space as $\mathbf{M} = \tau_x \otimes (-i\sigma_y)$ and $\mathbf{T} = \hat{1} \otimes (-i\sigma_y\mathbf{K})$, where $\hat{1}$ is the unity matrix in orbital space. Then, the generalized mirror symmetry $\mathbf{M}$ is equivalent to the parity symmetry $\mathbf{P}$ of the spinless fermion. To summarize the key results of our symmetry analysis, our spinful model Hamiltonian of phase **II** is invariant under each of the TR- and mirror (parity) operations:

$$\mathbf{T}\,\hat{H}_s^{II}(\mathbf{k})\,\mathbf{T}^{-1} = \hat{H}_s^{II}(-\mathbf{k}) = \hat{H}_s^{II}(\mathbf{k}), \tag{D.20}$$

$$\mathbf{M}\,\hat{H}_s^{II}(k_x, k_y)\,\mathbf{M}^{-1} = \hat{H}_s^{II}(\pm k_x, \mp k_y). \tag{D.21}$$

D.7.4 Even and odd parity subspaces of phase II of spinful $\hat{H}_s$

For the spinful Hamiltonian, the Chern number is only meaningful for phase **I**. This can be seen from its non-zero Chern number $\mathcal{C}[\hat{H}_s^I] = -\mathcal{C}[\mathbf{M}\,\hat{H}_s^I\,\mathbf{M}^{-1}] = -\mathcal{C}[\mathbf{T}\,\hat{H}_s^I\,\mathbf{T}^{-1}] = \pm 4$. Consequently, $\hat{H}_s^I$ has two distinguishable degenerated states of $\mathcal{C} = \pm 4$, which can be mapped onto each other.

On the other side, phase **II** also has two distinguishable degenerated states, however, these two states cannot be distinguished by the Chern number, because $\mathcal{C}[\hat{H}_s^{II}] = 0$.

Thus, we need to further examine its symmetry properties to see whether it is topological or not. A very direct and useful check is to see whether the system has a Z_2-like invariant index. This symmetry has been widely used in the search for 2D and 3D topological insulators, because there exist general methods to calculate the Z_2 topological invariant, especially when the Hamiltonian exhibits inversion symmetry. In phase **II**, the operator $\mathbf{M}$ commutes with the orbital-flux term $\hat{H}^{II}_{AOH}$ and $\hat{H}^{II}_{s}$. The even parity subspace is described along the contour, $\mathbb{C} \in \{(\Gamma - M); (M - X)\}$, and gives the commutation relation, $\mathbf{M}\,\hat{H}^{II}_{s}(\mathbb{C})\,\mathbf{M}^{-1} = \hat{H}^{II}_{s}(\mathbb{C})$. Whereas the odd parity subspace is located at the high-symmetry points for the parameters we choose, $\Lambda_n \in \{(\pm\frac{\pi}{2}, \pm\frac{\pi}{2}); (\pm\frac{\pi}{2}, \mp\frac{\pi}{2})\}$, and gives the anti-commutation relation, $\mathbf{M}\,\hat{H}^{II}_{s}(\Lambda_n)\,\mathbf{M}^{-1} = -\hat{H}^{II}_{s}(\Lambda_n)$. This $\pm$-parity symmetry motivated us to construct the Z_2-like topological invariant in the main text in order to test for the topological ground state with vanishing Chern number.

Bibliography

[1] Y. Kamihara, H. Hiramatsu, M. Hirano, R. Kawamura, H. Yanagi, T. Kamiya, and H. Hosono. *J. Am. Chem. Soc.*, 128:10012, 2006.

[2] G.F. Chen, Z. Li, D. Wu, G. Li, W.Z. Hu, J. Dong, P. Zheng, J.L. Luo, and N.L. Wang. *Phys. Rev. Lett.*, 100:247002, 2008.

[3] Johnpierre Paglione and Richard L. Greene. *Nat. Phys.*, 6:645, 2010.

[4] Y. Kamihara, T. Watanabe, M. Hirano, and H. Hosono. *J. Am. Chem. Soc.*, 130: 3296, 2008.

[5] Z.-A. Ren, W. Lu, J. Yang, W. Yi, X.-L. Shen, Z.-C. Li, G.-C. Che, X.-L. Dong, L.-L. Sun, F. Zhou, and Z.-X.C. Zhao. *Chin. Phys. Lett.*, 25:2215, 2008.

[6] T. Shimojima, K. Ishizaka, Y. Ishida, N. Katayama, K. Ohgushi, T. Kiss, M. Okawa, T. Togashi, X.-Y. Wang, C.-T. Chen, S. Watanabe, R. Kadota, T. Oguchi, A. Chainani, and S. Shin. *Phys. Rev. Lett.*, 104:057002, 2010.

[7] Chi-Cheng Lee, Wei-Guo Yin, and Wei Ku. *Phys. Rev. Lett.*, 103:267001, 2009.

[8] V. Cvetkovic and Z. Tesanovic. *Europhys. Lett.*, 85:37002, 2009.

[9] Kazuhiko Kuroki, Seiichiro Onari, Ryotaro Arita, Hidetomo Usui, Yukio Tanaka, Hiroshi Kontani, and Hideo Aoki. *Phys. Rev. Lett.*, 101:087004, 2008.

[10] Patrick A. Lee and Xiao-Gang Wen. *Phys. Rev. B*, 78:144517, 2008.

[11] M. Daghofer, A. Nicholson, A. Moreo, and E. Dagotto. *Phys. Rev. B*, 81:014511, 2010.

[12] S. Raghu, X. L. Qi, C. X. Liu, D. J. Scalapino, and S. C. Zhang. *Phys. Rev. B*, 77:220503, 2008.

[13] Degang Zhang. *Phys. Rev. Lett.*, 103:186402, 2009.

[14] J. Hu and N. Hao. *Phys. Rev. X*, 2:021009, 2012.

[15] Yuan-Yen Tai, Jian-Xin Zhu, Matthias J. Graf, and C. S. Ting. *Europhys. Lett.*, 103:67001, 2013.

[16] A. B. Vorontsov, M. G. Vavilov, and A. V. Chubukov. *Phys. Rev. B*, 79:060508, 2009.

[17] S. Maiti, R. M. Fernandes, and A. V. Chubukov. *Phys. Rev. B*, 85:144527, 2012.

[18] D. Parker, M. G. Vavilov, A. V. Chubukov, and I. I. Mazin. *Phys. Rev. B*, 80: 100508, 2009.

[19] Tao Zhou, D. Zhang, and C. S. Ting. *Phys. Rev. B*, 81:052506, 2010.

[20] Yuan-Yen Tai, Jian-Xin Zhu, Matthias J. Graf, and C. S. Ting. *Phys. Rev. B*, 86: 134512, 2012.

[21] J. Guo, S. Jin, G. Wang, S. Wang, K. Zhu, T. Zhou, M. He, and X. Chen. *Phys. Rev. B*, 82:180520, 2010.

[22] A. Krzton-Maziopa, Z. Shermadini, E. Pomjakushina, V. Pomjakushin, M. Bendele, A. Amato, R. Khasanov, H. Luetkens, and K. Conder. *J. Phys.: Condens. Matter*, 23:052203, 2011.

[23] M. Fang, H. Wang, C. Dong, Z. Li, C. Feng, J. Chen, and H. Q. Yuan. *Europhys. Lett.*, 94:27009, 2011.

[24] H. Wang, C. Dong, Z. Li, S. Zhu, Q. Mao, C. Fang, H. Q. Yuan, and M. Fang. *Europhys. Lett.*, 93:47004, 2011.

[25] D. M. Wang, J. B. He, T.-L. Xia, and G. F. Chen. *Phys. Rev. B*, 83:132502, 2011.

[26] L. Haggstrom and A. Seidel. *J. Magn. Magn. Mater.*, 98:37, 1991.

[27] Z Wang, Y. J. Song, H. L. Shi, Z. Wang, Z. Chen, H. F. Tian, G. F. Chen, J. G. Guo, H. X. Yang, and J. Q. Li. *Phys. Rev. B*, 83:140505(R), 2011.

[28] X.-W. Yan, M. Gao, Z.-Y. Lu, and T. Xiang. *Phys. Rev. Lett.*, 106:087005, 2011.

[29] C. Cao and J. Dai. *Phys. Rev. B*, 83:193104, 2011.

[30] R. Yu, J.-X. Zhu, and Q. Si. *Phys. Rev. Lett.*, 106:186401, 2011.

[31] Y. Zhou, D. Xu, W. Chen, and F. Zhang. *Europhys. Lett.*, 95:17003, 2011.

[32] W. Bao, Q. Huang, G. F. Chen, M. A. Green, D. M. Wang, J. B. He, X. Q. Wang, and Y. Qiu. *Chin. Phys. Lett.*, 28:086104, 2011.

[33] C. Cao and J. Dai. *Phys. Rev. Lett.*, 107:056401, 2011.

[34] F. Ye, S. Chi, Wei Bao, X. F. Wang, J. J. Ying, X. H. Chen, H. D. Wang, C. H. Dong, and Minghu Fang. *Phys. Rev. Lett.*, 107:137003, 2011.

[35] V. Yu. Pomjakushin, D. V. Sheptyakov, E. V. Pomjakushina, A. Krzton-Maziopa, K. Conder, D. Chernyshov, V. Svitlyk, and Z. Shermadini. *Phys. Rev. B*, 83: 144410, 2011.

[36] L. Zhang and D. J. Singh. *Phys. Rev. B*, 79:094528, 2009.

[37] X.-W. Yan, M. Gao, Z.-Y. Lu, and T. Xiang. *Phys. Rev. B*, 84:054502, 2011.

[38] C. Cao and J. Dai. *Chin. Phys. Lett.*, 28:057402, 2011.

[39] I. R. Shein and A. L. Ivanovskii. *Phys. Lett. A*, 375:1028, 2011.

[40] I. A. Nekrasov and M. V. Sadovskii. *JETP Lett.*, 93:166, 2011.

[41] Y. Zhang, L. X. Yang, M. Xu, Z. R. Ye, F. Chen, C. He, H. C. Xu, J. Jiang, B. P. Xie, J. J. Ying, X. F. Wang, X. H. Chen, J. P. Hu, M. Matsunami, S. Kimura, and D. L. Feng. *Nature Mater.*, 10:273, 2011.

[42] X.-P. Wang, T. Qian, P. Richard, P. Zhang, J. Dong, H.-D. Wang, C.-H. Dong, M.-H. Fang, and H. Ding. *Europhys. Lett.*, 93:57001, 2011.

[43] Daixiang Mou, Shanyu Liu, Xiaowen Jia, Junfeng He, Yingying Peng, Lin Zhao, Li Yu, Guodong Liu, Shaolong He, Xiaoli Dong, Jun Zhang, Hangdong Wang, Chiheng Dong, Minghu Fang, Xiaoyang Wang, Qinjun Peng, Zhimin Wang, Shenjin Zhang, Feng Yang, Zuyan Xu, Chuangtian Chen, and X. J. Zhou. *Phys. Rev. Lett.*, 106:107001, 2011.

[44] T. Qian, X.-P. Wang, W.-C. Jin, P. Zhang, P. Richard, G. Xu, X. Dai, Z. Fang, J.-G. Guo, X.-L. Chen, and H. Ding. *Phys. Rev. Lett.*, 106:187001, 2011.

[45] M. Xu, Q. Q. Ge, R. Peng, Z. R. Ye, Juan Jiang, F. Chen, X. P. Shen, B. P. Xie, Y. Zhang, A. F. Wang, X. F. Wang, X. H. Chen, and D. L. Feng. *Phys. Rev. B*, 85:220504, 2012.

[46] Degang Zhang. *Phys. Rev. Lett.*, 104:089702, 2010.

[47] K. Terashima, Y. Sekiba, J. H. Bowen, K. Nakayama, T. Kawahara, T. Sato, P. Richard, Y.-M. Xu, L. J. Li, and G. H. Cao. *Proc. Acad. Nat. Sci. USA*, 106: 7330, 2009.

[48] Y Sekiba, T Sato, K Nakayama, K Terashima, P Richard, J H Bowen, H Ding, Y-M Xu, L J Li, G H Cao, Z-A Xu, and T Takahashi. *New J. Phys.*, 11:025020, 2009.

[49] Clarina de la Cruz, Q. Huang, J. W. Lynn, Jiying Li, W. Ratcliff II, J. L. Zarestky, H. A. Mook, G. F. Chen, J. L. Luo, N. L. Wang, and Pengcheng Dai. *Nature (London)*, 453:899, 2008.

[50] T.-M. Chuang, M. P. Allan, Jinho Lee, Yang Xie, Ni Ni, S. L. Bud'ko, G. S. Boebinger, P. C. Canfield, and J. C. Davis. *Science*, 327:181, 2010.

[51] D. K. Pratt, W. Tian, A. Kreyssig, J. L. Zarestky, S. Nandi, N. Ni, S. L. Bud'ko, P. C. Canfield, A. I. Goldman, and R. J. McQueeney. *Phys. Rev. Lett.*, 103:087001, 2009.

[52] Yi Gao, Tao Zhou, C. S. Ting, and Wu-Pei Su. *Phys. Rev. B*, 82:104520, 2010.

[53] Yi Gao, Huai-Xiang Huang, Chun Chen, C. S. Ting, and Wu-Pei Su. *Phys. Rev. Lett.*, 106:027004, 2011.

[54] . In principle, the multiorbital t-J model can be derived from the multiorbital Hubbard model in the large-U limit, similar to the single-orbital model for high-T_c cuprates [see for example F. C. Zhang, C. Gros, T. M. Rice, and H. Shiba, Supercond. Sci. Technol. **1**, 36 (1988)]. So far, such general and cumbersome derivation has not been done in the literature. Instead, our constructed t-J model, on the one hand, describes the magnetism 245 ($\sqrt{5}$-$\sqrt{5}$) structure in itinerant picture, and on the other hand gives the proper description of the shape of Fermi surface compared to the ARPES data in various doping region.

[55] Q. Si and E. Abrahams. *Phys. Rev. Lett.*, 101:076401, 2008.

[56] Qimiao Si, Elihu Abrahams, Jianhui Dai, and Jian-Xin Zhu. *New J. Phys.*, 11: 045001, 2009.

[57] Jianhui Dai, Qimiao Si, Jian-Xin Zhu, and Elihu Abrahams. *PNAS*, 106:4118, 2009.

[58] Kangjun Seo, B. Andrei Bernevig, and Jiangping Hu. *Phys. Rev. Lett.*, 101:206404, 2008.

[59] Pallab Goswami, Predrag Nikolic, and Qimiao Si. *Europhys. Lett.*, 91:37006, 2010.

[60] Rong Yu, Pallab Goswami, Qimiao Si, Predrag Nikolic, and Jian-Xin Zhu. *arxiv:1103.3259*, 2011.

[61] R. H. Yuan, T. Dong, Y. J. Song, P. Zheng, G.F. Chen, J. P. Hu, J. Q. Li, and N. L. Wang. *Scientific Reports*, 2:221, 2012.

[62] F. Chen, M. Xu, Q. Q. Ge, Y. Zhang, Z. R. Ye, L. X. Yang, Juan Jiang, B. P. Xie, R. C. Che, M. Zhang, A. F. Wang, X. H. Chen, D. W. Shen, J. P. Hu, and D. L. Feng. *Phys. Rev. X*, 1:021020, 2011.

[63] Meng Wang, Miaoyin Wang, G. N. Li, Q. Huang, C. H. Li, G. T. Tan, C. L. Zhang, Huibo Cao, Wei Tian, Yang Zhao, Y. C. Chen, X. Y. Lu, Bin Sheng, H. Q. Luo, S. L. Li, M. H. Fang, J. L. Zarestky, W. Ratcliff, M. D. Lumsden, J. W. Lynn, and Pengcheng Dai. *Phys. Rev. B*, 84:094504, 2011.

[64] Wei Li, Shuai Dong, Chen Fang, and Jiangping Hu. *Phys. Rev. B*, 85:100407, 2012.

[65] Jian-Xin Zhu, Rong Yu, A. V. Balatsky, and Qimiao Si. *Phys. Rev. Lett.*, 107: 167002, 2011.

[66] Tom Berlijn, P. J. Hirschfeld, and Wei Ku. *arxiv:1204.2849*, 2012.

[67] S. Ducatman, N. B. Perkins, and A. Chubukov. *arxiv:1207.2201*, 2012.

[68] J.-X. Zhu W. Li, J. Li and C. S. Ting. *Europhys. Lett.*, 99:57006, 2012.

[69] T. Das and A. V. Balatsky. *Phys. Rev. B*, 84:115117, 2011.

[70] N. Hao, Y. Wang, and J. Hu. *arXiv:1207.6798*.

[71] G. Xu, W. Ming, Y. Yao, X. Dai, S.-C. Zhang, and Z. Fang. *Europhys. Lett.*, 82: 67002, 2008.

[72] C. Lester, J.-H. Chu, J. G. Analytis, S. C. Capelli, A. S. Er-ickson, C. L. Condron, M. F. Toney, I. R. Fisher, and S. M. Hayden. *Phys. Rev. B*, 79:144523, 2009.

[73] X. F. Wang, T. Wu, G. Wu, R. H. Liu, H. Chen, Y. L. Xie, and X. H. Chen. *New J. Phys.*, 11:045003, 2009.

[74] Y. Laplace, J. Bobroff, F. Rullier-Albenque, D. Colson, and A. Forget. *Phys. Rev. B*, 80:140501, 2009.

[75] T. Sato, K. Nakayama, Y. Sekiba, P. Richard, Y.-M. Xu, S. Souma, T. Takahashi, G. F. Chen, J. L. Luo, N. L. Wang, and H. Ding. *Phys. Rev. Lett.*, 103:047002, 2009.

[76] M. Rotter, M. Pangerl, M. Tegel, and D. Johrendt. *Angew. Chem. Int. Ed.*, 47: 7947, 2008.

[77] H. Chen, Y. Ren, Y. Qiu, W. Bao, R. H. Liu, G. Wu, T. Wu, Y. L. Xie, X. F. Wang, Q. Huang, , and X. H. Chen. *Europhys. Lett.*, 85:17006, 2009.

[78] I. I. Mazin, D. J. Singh, M. D. Johannes, , and M. H. Du. *Phys. Rev. Lett.*, 101: 057003, 2008.

[79] D. J. Singh and M.-H. Du. *Phys. Rev. Lett.*, 100:237003, 2008.

[80] P. Richard, K. Nakayama, T. Sato, M. Neupane, Y.-M. Xu, J. H. Bowen, G. F. Chen, J. L. Luo, N. L. Wang, X. Dai, Z. Fang, H. Ding, and T. Takahashi. *Phys. Rev. Lett.*, 104:137001, 2010.

[81] T. Zhou, H. Huang, Y. Gao, J.-X. Zhu, , and C. S. Ting. *Phys. Rev. B*, 83:214502, 2011.

[82] C. Zheng and R. Hoffmann. *J. Solid State Chem.*, 72:58, 1988.

[83] J. Kunes, R. Arita, P. Wissgott, A. Toschi, H. Ikeda, , and K. Held. *Comput. Phys. Commun.*, 181:1888, 2010.

[84] . The Hamiltonian H_2^t is invariant by exchange of orbitals in one sublattice if and only if one exchanges t_1 and t_5. Therefore, the elements in W_k can be re-written: $\xi_{A1} = \xi_{B1} = \xi^H$, $\xi_{A2} = \xi_{B2} = \xi^V$ and $\xi_t = 4\,t_5 \cos(k_x/2)\,cos(k_y/2)$, $\xi_c = 4\,t_1 \cos(k_x/2)\,cos(k_y/2)$ and ξ_{12} kept unchanged. In the main text we chose a notation to simplify the comparison to Zhang's model.

[85] . The hopping terms t_2 and t_3 control the Fermi surface anisotropy; t_4 controls the band splitting at both M and Γ points of the BZ; t_5 controls the band splitting at the Γ point; t_6 modifies the band curvature along the Γ-M direction. For a set of given values of $|t_1|$, $|t_4|$ and $|t_5|$, the band dispersion is unchanged when the following condition is obeyed: $t_1 \times t_4 \times t_5 > 0$.

[86] . All calculations were performed on a 40×40 lattice of Fe sites. The supercell technique with periodic boundary conditions was applied to reduce the size of the real-space Hamiltonian in k-space.

[87] A. M. Oleś, G. Khaliullin, P. Horsch, and L. F. Feiner. *Phys. Rev. B*, 72:214431, 2005.

[88] S. Avci, O. Chmaissem, D. Y. Chung, S. Rosenkranz, E. A. Goremychkin, J. P. Castellan, I. S. Todorov, J. A. Schlueter, H. Claus, A. Daoud-Aladine, D. D. Khalyavin, M. G. Kanatzidis, , and R. Osborn. *Phys. Rev. B*, 85:184507, 2012.

[89] M. L. Teague, G. K. Drayna, G. P. Lockhart, P. Cheng, B. Shen, H.-H. Wen, , and N.-C. Yeh. *Phys. Rev. Lett.*, 106:087004, 2011.

[90] X. Zhang, Y. S. Oh, Y. Liu, L. Yan, S. R. Saha, N. P. Butch, K. Kirshenbaum, K. H. Kim, J. Paglione, R. L. Greene, , and I. Takeuchi. *Phys. Rev. B*, 82:020515, 2010.

[91] Y. Yin, M. Zech, T. Williams, , and J. Hoffman. *Physica C*, 469:535, 2009.

[92] F. Massee, Y. Huang, R. Huisman, S. de Jong, J. B. Goedkoop, , and M. S. Golden. *Phys. Rev. B*, 79:22051, 2009.

[93] P. J. Hirschfeld, M. M. Korshunov, , and I. I. Mazin. *Rep. Prog. Phys.*, 74:124508, 2011.

[94] T. Maier, S. Graser, D. Scalapino, , and P. Hirschfeld. *Phys. Rev. B*, 79:224510, 2009.

[95] J.-P. Reid, M. A. Tanatar, A. Juneau-Fecteau, R. T. Gordon, S. R. de Cotret, N. Doiron-Leyraud, T. Saito, H. Fukazawa, Y. Kohori, K. Kihou, C. H. Lee, A. Iyo, H. Eisaki, R. Prozorov, , and L. Taillefer. *Phys. Rev. Lett.*, 109:087001, 2012.

[96] R. Thomale, C. Platt, W. Hanke, J. Hu, , and B. A. Bernevig. *Phys. Rev. Lett.*, 107:117001, 2011.

[97] S. Maiti, M. M. Korshunov, T. A. Maier, P. J. Hirschfeld, , and A. V. Chubulov. *Phys. Rev. Lett.*, 107:147002, 2011.

[98] H. Fukazawa, Y. Yamada, K. Kondo, T. Saito, Y. Kohori, K. Kuga, Y. Matsumoto, S. Nakatsuji, H. Kito, P. M. Shirage, K. Kihou, N. Takeshita, C.-H. Lee, A. Iyo, , and H. Eisaki. *J. Phys. Soc. Jpn.*, 78:083712, 2009.

[99] J. K. Dong, S. Y. Zhou, T. Y. Guan, H. Zhang, Y. F. Dai, X. Qiu, X. F. Wang, Y. He, X. H. Chen, , and S. Y. Li. *Phys. Rev. Lett.*, 104:087005, 2010.

[100] K. Hashimoto, A. Serafin, S. Tonegawa, R. Katsumata, R. Okazaki, T. Saito, H. Fukazawa, Y. Kohori, K. Kihou, C. H. Lee, A. Iyo, H. Eisaki, H. Ikeda, Y. Matsuda, A. Carrington, , and T. Shibauchi. *Phys. Rev. B*, 82:014526, 2010.

[101] K. Okazaki, Y. Ota, Y. Kotani, W. Malaeb, Y. Ishida, T. Shi-mojima, T. Kiss, S. Watanabe, C.-T. Chen, K. Kihou, C. H. Lee, A. Iyo, H. Eisaki, T. Saito, H. Fukazawa, Y. Kohori, K. Hashimoto, T. Shibauchi, Y. Matsuda, H. Ikeda, H. Miya-hara, R. Arita, A. Chainani, , and S. Shin. *Science*, 337:1314, 2012.

[102] M. H. Julien, H. Mayaffre, M. Horvatić, C. Berthier, X. D. Zhang, W. Wu, G. F. Chen, N. L. Wang, and J. L. Luo. *Europhys. Lett.*, 87:37001, 2009.

[103] R. M. Fernandes and J. Schmalian. *Phys. Rev. B*, 82:014521, 2010.

[104] Z. J. Yao, J. X. Li, , and Z. D. Wang. *New J. Phys.*, 11:025009, 2009.

[105] F. Wang, H. Zhai, Y. Ran, A. Vishwanath, , and D. H. Lee. *Phys. Rev. Lett.*, 102: 047005, 2009.

[106] A. D. Christinason et al. *Nature*, 456:930, 2008.

[107] C. T. Chen, C. C. Tsuei, M. B. Ketchen, Z. A. Ren, and Z. X. Zhao. *Nature Phys.*, 6:260, 2010.

[108] T. Hanaguri, S. Niitaka, K. Kuroki, , and H. Takagi. *Science*, 328:474, 2010.

[109] S. Graser, T. A. Maier, P. J. Hirschfeld, and D. J. Scalapino. *New J. Phys.*, 11: 025016, 2009.

[110] Y. Ran, F. Wang, H. Zhai, A. Vishwanath, , and D. H. Lee. *Phys. Rev. B*, 79: 014505, 2009.

[111] S. de Jong and et al. *Europhys. Lett.*, 89:27007, 2010.

[112] D. Hsieh, Y. Xia, L. Wray, D. Qian, K. Gomes, A. Yazdani, G. F. Chen, J. L. Luo, N. L. Wang, , and M. Z. Hasan. *arXiv:0812.2289*.

[113] K. K. Huynh, Y. Tanabe, and K. Tanigaki. *Phys. Rev. Lett.*, 106:217004, 2011.

[114] M. Yi and et al. *Proc. Natl. Acad. Sci.*, 108:6878, 2011.

[115] H. Ding et al. *J. Phys.: Condens. Matter*, 23:135701, 2011.

[116] L. Wray and et al. *Phys. Rev. B*, 78:184508, 2008.

[117] H. Ding and et al. *Europhys. Lett.*, 83:47001, 2008.

[118] L. Zhao and et al. *Chin. Phys. Lett.*, 25:4402, 2008.

[119] X. P. Wang and et al. *Phys. Rev. B*, 85:214518, 2012.

[120] V. Vildosola, L. Pourovskii, R. Arita, S. Biermann, , and A. Georges. *Phys. Rev. B*, 78:064518, 2008.

[121] H. J. Zhang, G. Xu, X. Dai, , and Z. Fang. *Chin. Phys. Lett.*, 26:017401, 2009.

[122] M. Rotter, M. Tegel, , and D. Johrendt. *Phys. Rev. Lett.*, 101:107006, 2008.

[123] A. Leither-Jasper, W. Schnelle, C. Geibel, , and H. Rosner. *Phys. Rev. Lett.*, 101: 207004, 2008.

[124] N. Ni, S. L. Bud'ko, A. Kreyssig, S. Nandi, G. E. Rustan, A. I. Goldman, S. Gupta, J.D. Corbett, A. Kracher, , and P. C. Canfield. *Phys. Rev. B*, 78:014507, 2008.

[125] H. Q. Luo, Z. S. Wang, H. Yang, P. Cheng, X. Y. Zhu, , and H. H. Wen. *Supercond. Sci. Technol.*, 21:125014, 2008.

[126] G. F. Chen, Z. Li, J. Dong, G. Li, W. Z. Hu, X. D. Zhang, X. H. Song, P. Zheng, N. L. Wang, , and J. L. Luo. *Phys. Rev. B*, 78:224512, 2008.

[127] A. S. Sefat, R. Y. Jin, M. A. McGuire, B. C. Sales, D. J. Singh, , and D. Mandrus. *Phys. Rev. Lett.*, 101:117004, 2008.

[128] L. J. Li, Y. K. Luo, Q. B. Wang, H. Chen, Z. Ren, Q. Tao, Y. K. Li, X. Lin, M. He, Z. W. Zhu, G. H. Cao, , and Z. A. Xu. *New J. Phys.*, 11:025008, 2009.

[129] S. R. Saha, N. P. Butch, K. Kirshenbaum, , and J. Paglione. *Phys. Rev. B*, 79: 224519, 2009.

[130] R. T. Gordon, H. Kim, N. Salovich, R. W. Giannetta, R. M. Fernandes, V. G. Kogan, T. Prozorov, S. L. Budko, P. C. Canfield, M. A. Tanatar, , and R. Prozorov. *Phys. Rev. B*, 82:054507, 2010.

[131] M. G. Vavilov, A. V. Chubukov, , and A. B. Vorontsov. *Supercond. Sci. Technol.*, 23:054011, 2009.

[132] Q. Si. *Nat. Phys.*, 5:639, 2009.

[133] J. Hu and H. Ding. *Sci. Rep.*, 2:381, 2012.

[134] S. B. Zhang, Y. F. Guo, J. J. Li, X. X. Wang, K. Yamaura, , and E. Takayama-Muromachi. *Physica C*, 471:600, 2011.

[135] Y. Qi, Z. Gao, L. Wang, X. Zhang, D. Wang, C. Yao, C. Wang, C. Wang, , and Y. Ma. *Europhys. Lett.*, 96:47005, 2011.

[136] Y. Nishijubo, S. Kakiya, M. Danura, K. Kudo, , and M. Nohara. *J. Phys. Soc. Jpn.*, 79:095002, 2010.

[137] F. Han, X. Zhu, P. Ceng, G. Mu, Y. Jia, L. Fang, Y. Wang, H. Luo, B. Zeng, B. Shen, L. Shan, C. Ren, , and H.-H. Wen. *Phys. Rev. B*, 80:024506, 2009.

[138] Seiichiro Onari and Hiroshi Kontani. *Phys. Rev. Lett.*, 103:177001, 2009.

[139] G. R. Boyd, P. J. Hirschfeld, , and T. P. Devereaux. *Phys. Rev. B*, 82:134506, 2010.

[140] D. V. Efremov, M. M. Korshunov, O. V. Dolgov, A. A. Golubov, , and P. J. Hirschfeld. *Phys. Rev. B*, 84:180512(R), 2011.

[141] R. M. Fernandes, M. G. Vavilov, , and A. V. Chubukov. *Phys. Rev. B*, 85: 140512(R), 2012.

[142] Y. Wang, A. Kreisel, , and P. J. Hirschfeld. *Phys. Rev. B*, 87:094504, 2013.

[143] Tom Berlijn, Chia-Hui Lin, William Garber, , and Wei Ku. *Phys. Rev. Lett.*, 108: 207003, 2012.

[144] A. V. Balatsky, I. Vekhter, , and J.-X. Zhu. *Rev. Mod. Phys.*, 78:373, 2006.

[145] Yuke Li, Xiao Lin, Qian Tao, Cao Wang, Tong Zhou, Linjun Li, Qingbo Wang, Mi He, Guanghan Cao, and Zhu'an Xu. *New J. Phys.*, 11:053008, 2009.

[146] Yuke Li, Jun Tong, Qian Tao, Chunmu Feng, Guanghan Cao, Weiqiang Chen, Fu chun Zhang, and Zhu an Xu. *New J. Phys.*, 12:083008, 2010.

[147] Zi-Jian Yao, Wei-Qiang Chen, Yu ke Li, Guang han Cao, Hong-Min Jiang, Qian-En Wang, Zhu an Xu, , and Fu-Chun Zhang. *Phys. Rev. B*, 86:184515, 2012.

[148] Peng Cheng, Bing Shen, Jiangping Hu, , and Hai-Hu Wen. *Phys. Rev. B*, 81: 174529, 2010.

[149] Jun Li, Yanfeng Guo, Shoubao Zhang, Shan Yu, Yoshihiro Tsujimoto, Hiroshi Kontani, Kazunari Yamaura, , and Eiji Takayama-Muromachi. *Phys. Rev. B*, 84: 020513(R), 2011.

[150] Jun Li, Yanfeng Guo, Shoubao Zhang, Yoshihiro Tsujimoto, Xia Wang, C.I. Sathish, Shan Yu, Kazunari Yamaura, and Eiji Takayama-Muromachi. *Solid State Commun.*, 152:671, 2012.

[151] J. Li, Y. F. Guo, S. B. Zhang, J. Yuan, Y. Tsujimoto, X. Wang, C. I. Sathish, Y. Sun, S. Yu, W. Yi, K. Yamaura, E. Takayama-Muromachiu, Y. Shirako, M. Akaogi, , and H. Kontani. *Phys. Rev. B*, 85:214509, 2012.

[152] H. Wadati, I. Elfimov, , and G. A. Sawatzky. *Phys. Rev. Lett.*, 105:157004, 2010.

[153] Kazuma Nakamura, Ryotaro Arita, , and Hiroaki Ikeda. *Phys. Rev. B*, 83:144512, 2011.

[154] S. Ideta, T. Yoshida, M. Nakajima, W. Malaeb, T. Shimojima, K. Ishizaka, A. Fujimori, H. Kimigashira, K. Ono, K. Kihou, Y. Tomioka, C. H. Lee, A. Iyo, H. Eisaki, T. Ito, , and S. Uchida. *Phys. Rev. B*, 87:201110(R), 2013.

[155] S. Ideta, T. Yoshida, M. Nakajima, W. Malaeb, T. Shimojima, K. Ishizaka, A. Fujimori, H. Kimigashira, K. Ono, K. Kihou, Y. Tomioka, C. H. Lee, A. Iyo, H. Eisaki, T. Ito, and S. Uchida. *arXiv:1304.5860v1.*

[156] M. Kano, Y. Kohama, D. Graf, F. Balakirev, A. S. Sefat, M. A. Mcguire, B. C. Sales, D. Mandrus, , and S. W. Tozer. *J. Phys. Soc. Jpn.*, 78:084719, 2009.

[157] A. A. Abrikosov and L. P. Gor'kov. *Sov. Phys. JETP*, 12:1243, 1961.

[158] M. Franz, C. Kallin, A. J. Berlinksky, , and M. I. Salkola. *Phys. Rev. B*, 56:7882, 1997.

[159] T. Das, J.-X. Zhu, , and M. J. Graf. *Phys. Rev. B*, 84:134510, 2011.

[160] K. Ohishi, R.H . Heffner, G. D. Morris, E. D. Bauer, M. J. Graf, J.-X. Zhu, L. A. Morales, J. L. Sarrao, M. J. Fluss, D. E. MacLaughlin, L. Shu, W. Higemoto, , and T. U. Ito. *Phys. Rev. B*, 76:064504, 2007.

[161] R. Beaird, I. Vekhter, , and J.-X. Zhu. *Phys. Rev. B*, 86:140507, 2012.

[162] C. Cao, P. J. Hirschfeld, , and H.-P. Cheng. *Phys. Rev. B*, 77:220506(R), 2008.

[163] Y. Bang. *Europhys. Lett.*, 86:47001, 2009.

[164] I. I. Mazin. *Nature*, 464:183, 2010.

[165] B. Nachumi, A. Keren, K. Kojima, M. Larkin, G. M. Luke, J. Merrin, O. Tchernyshoev, Y. J. Uemura, N. Ichikawa, M. Goto, , and S. Uchida. *Phys. Rev. Lett.*, 77:5421, 1996.

[166] A. P. Mackenzie, R. K. W. Haselwimmer, A. W. Tyler, G. G. Lonzarich, Y. Mori, S. Nishizaki, , and Y. Maeno. *Phys. Rev. Lett.*, 80:161, 1998.

[167] J. B. Kycia, J. I. Hong, M. J. Graf, J. A. Sauls, D. N. Seidman, , and W. P. Halperin. *Phys. Rev. B*, 58:R603, 1998.

[168] F. Jutier, G. A. Ummarino, J.-C. Griveau, F. Wastin, E. Colineau, J. Rebizant, N. Magnani, , and R. Caciuffo. *Phys. Rev. B*, 77:024521, 2008.

[169] K. Hashimoto, T. Shibauchi, S. Kasahara, K. Ikada, S. Tonegawa, T. Kato, R. Okazaki, C. J. van der Beek, M. Konczykowski, H. Takeya, K. Hirata, T. Terashima, , and Y. Matsuda. *Phys. Rev. Lett.*, 102:207001, 2009.

[170] R. T. Gordon, N. Ni, C. Martin, M. A. Tanatar, M. D. Vannette, H. Kim, G. D. Samolyuk, J. Schmalian, S. Nandi, A. Kreyssig, A. I. Goldman, J. Q. Yan, S. L. Bud'ko, P. C. Canfield, , and R. Prozorov. *Phys. Rev. Lett.*, 102:127004, 2009.

[171] R. T. Gordon, C. Martin, H. Kim, N. Ni, M. A. Tanatar, J. Schmalian, I. I. Mazin, S. L. BudÕko, P. C. Canfield, , and R. Prozorov. *Phys. Rev. B*, 79:100506(R), 2009.

[172] H. Kim, R. T. Gordon, M. A. Tanatar, J. Hua, U. Welp, W. K. Kwok, N. Ni, S. L. Bud'ko, P. C. Canfield, A. B. Vorontsov, , and R. Prozorov. *Phys. Rev. B*, 82: 060518, 2010.

[173] J. Yong, S. Lee, J. Jiang, C. Bark, J. Weiss, E. Hellstrom, D. Larbalestier, C. Eom, , and T. Lemberger. *Phys. Rev. B*, 83:104510, 2011.

[174] A. A. Barannik, N. T. Cherpak, N. Ni, M. A. Tanatar, S.A. Vitusevich, V. N. Skresanov, P. C. Canfield, R. Prozorov, V.V. Glamazdin, , and K. I. Torokhtii. *Low Temp. Phys.*, 37:725, 2011.

[175] T. J. Williams, A. A. Aczel, E. Baggio-Saitovitch, S. L. Bud'ko, P. C. Canfield, J. P. Carlo, T. Goko, J. Munevar, N. Ni, Y. J. Uemura, W. Yu, , and G. M. Luke. *Phys. Rev. B*, 80:094501, 2009.

[176] Huaixiang Huang, Yi Gao, Jian-Xin Zhu, , and C. S. Ting. *Phys. Rev. Lett.*, 109: 187007, 2012.

[177] D. J. Scalapino, S. R. White, , and S. C. Zhang. *Phys. Rev. Lett.*, 68:2830, 1992.

[178] D. J. Scalapino, S. R. White, , and S. C. Zhang. *Phys. Rev. B*, 47:7995, 1993.

[179] Karim Bouadim, Yen Lee Loh, Mohit Randeria, and Nandini Trivedi. *Nat. Phys.*, 7:884, 2011.

[180] Amit Ghosal, Mohit Randeria, , and Nandini Trivedi. *Phys. Rev. B*, 65:014501, 2001.

[181] L. Benfatto, A. Toschi, , and S. Caprara. *Phys. Rev. B*, 69:184510, 2004.

[182] T. V. Ramakrishnan. *Phys. Scr.*, T27:24, 1989.

[183] C. Martin, R. T. Gordon, M. A. Tanatar, H. Kim, N. Ni, S. L. Bud'ko, P. C. Canfield, H. Luo, H. H. Wen, Z. Wang, A. B. Vorontsov, V. G. Kogan, , and R. Prozorov. *Phys. Rev. B*, 80:020501(R), 2009.

[184] Jeehoon Kim, N. Haberkorn, M. J. Graf, I. Usov, F. Ronning, L. Civale, E. Nazaretski, G. F. Chen, W. Yu, J. D. Thompson, , and R. Movshovich. *Phys. Rev. B*, 86:144509, 2012.

[185] A. B. Vorontsov, M. G. Vavilov, , and A. V. Chubukov. *Phys. Rev. B*, 79:140507, 2009.

[186] J. H. Xu, J. H. Miller, Jr., , and C. S. Ting. *Phys. Rev. B*, 51:424, 1995.

[187] D. J. Thouless, M. Kohmoto, M. P. Nightingale, , and M. den Nijs. *Phys. Rev. Lett.*, 49:405, 1982.

[188] F. D. M. Haldane. *Phys. Rev. Lett.*, 61:2015, 1988.

[189] C. Kane and E. Mele. *Phys. Rev. Lett.*, 95:226801, 2005.

[190] C. Kane and E. Mele. *Phys. Rev. Lett.*, 95:146802, 2005.

[191] M. Knig, S. Weidmann, C. Brune, A. Roth, H. Buhmann, L. Molenkamp, X.-L. Qi, , and S. C. Zhang. *Science*, 318:766, 2007.

[192] B. A. Bernevig, T. L. Hughes, , and S. C. Zhang. *Science*, 314:1757, 2006.

[193] D. Hsieh, D. Qian, L. Wray, Y. Xia, Y. S. Hor, R. J. Cava, , and M. Z. Hasan. *Nature*, 452:970, 2008.

[194] M. Z. Hasan, , and C. L. Kane. *Rev. Mod. Phys.*, 82:3045, 2010.

[195] Y. Ando. *Journal of the Phys. Soc. of Japan.*, 82:102001, 2013.

[196] K. Sun, W. Vincent Liu, A. Hemmerich, and S. Das Sarma. *Nature Physics*, 8: 67–70, 2012.

[197] Y. D. Chong, Xiao-Gang Wen, , and M. Solijacic. *Phys. Rev. B*, 77:235125, 2008.

[198] M. Dzero, K. Sun, V. Galitski, , and P. Coleman. *Phys. Rev. Lett.*, 104:106408, 2010.

[199] . For the single-orbital models of the cuprates, the DDW state [200, 201] breaks the 1-atom per unit cell translational symmetry. In contrast, in our study of the 2-orbital model of pnictides, the 1-Fe per unit cell is translationally invariant with respect to the inter-orbital current flux order due to λ_{AOH}.

[200] S. Chakravarty, R. B. Laughlin, D. K. Morr, and C. Nayak. *Phys. Rev. B*, 63: 094503, 2000.

[201] J.-X. Zhu, W. Kim, C.S. Ting, and J.P. Carbotte. *Phys. Rev. Lett.*, 87:197001, 2001.

[202] J.-X. Zhu. *Phys. Rev. B*, 66:104523, 2002.

[203] M. E. Simon and C. M. Varma. *Phys. Rev. Lett.*, 89:247003, 2002.

[204] S. Raghu, X.-L. Qi, C. Honerkamp, and S.-C. Zhang. *Phys. Rev. Lett.*, 100:156401, 2008.

[205] K. Sugawara, T. Takahashi, Y. Kamihara, M. Hirano, and H. Hosono. *Journal of the Phys. Soc. of Japan.*, 77:063708, 2008.

[206] Bud'ko, P. C. Canfield, , and R. Prozorov. *Phys. Rev. B*, 82:134528, 2010.

[207] J.-Q. Meng, G.-D. Liu, X.-L. Dong, G. Wu, R.-H. Liu, X.-H. Chen, Z.-A. Ren, W. Yi, G.-C. Che, G.-F. Chen, N.-L. Wang, G.-L. Wang, Y. Zhou, Y. Zhu, X.-Y. Wang, Z.-X. Zhao, Z.-Y. Xu, C.-T. Chen, and X.-J. Zhou. *Chinese Phys. Lett.*, 25:3761, 2008.

[208] Guru Khalsa, Byounghak Lee, , and A. H. MacDonald. *Phys. Rev. B*, 88:041302, 2008.

[209] H. Chen, Y.-Y. Tai, C. S. Ting, M. J. Graf, Jianhui Dai, , and J.-X. Zhu. *Phys. Rev. B*, 88:184509, 2013.

[210] . The original model of [15] assumed the 2-Fe per unit cell Hamiltonian. However, Ref. [209] showed that a unitary transformation maps the 2-Fe onto 1-Fe per unit cell Hamiltonian in the absence of the spin-density wave.

[211] X.-L. Qi, T. L. Hughes, , and S.-C. Zhang. *Phys. Rev. B*, 78:195424, 2008.

[212] X.-L. Qi and S.-C. Zhang. *Rev. Mod. Phys.*, 83:1057, 2011.

[213] L. Fu and C. L. Kane. *Phys. Rev. B*, 76:045302, 2007.

[214] M. Z. Hasan and C. L. Kane. *Rev. Mod. Phys.*, 82:3045, 2010.

[215] Kazuhiro Sano and Yoshiaki Ono. *J. Phys. Soc. Jpn.*, 72:1847, 2003.